Electron Spin Echo Spectroscopy on Transition Metal Compounds

E.J. Reijerse

Electron Spin Echo Spectroscopy on Transition Metal Compounds

PROMOTOR: PROF. DR. E. de BOER
CO-REFERENT: DR. C.P. KEIJZERS

Electron Spin Echo Spectroscopy on Transition Metal Compounds

PROEFSCHRIFT

ter verkrijging van de graad van
doctor in de wiskunde en natuurwetenschappen
aan de Katholieke Universiteit te Nijmegen,
op gezag van de Rector Magnificus,
Prof.Dr. J.H.G.I. Giesbers,
volgens het besluit van het College van Decanen
in het openbaar te verdedigen
op donderdag 6 november 1986
des namiddags te 1.30 uur precies

door

Eduard Johannes Reijerse

geboren te Toronto

druk: Sneldruk, Enschede
1986

Graag wil ik iedereen bedanken die heeft bijgedragen aan het tot stand komen van dit proefschrift.

In het bijzonder wil ik hierbij Adrie Klaassen noemen, vanwie ik veel geleerd heb op het gebied van de Electron Spin Resonantie techniek, en die mij gedurende de gehele periode van mijn promotiewerk met raad en daad heeft bijgestaan. Ook Jan van Os wil ik bedanken voor zijn essentiele bijdrage aan de ontwikkeling en opbouw van de Electron Spin Echo spectrometer.

Marcel Paulissen, Richard Mensink en Renee Kanters dank ik voor het vele werk dat zij gedurende hun hoofd- of bijvakstage verricht hebben. Vooral Nic van Aerle wil ik bedanken voor zijn bijdrage aan dit proefschrift. Een groot gedeelte van de experimenten beschreven in de hoofstukken VIII en IX zijn door hem uitgevoerd.

Ook Addy Thiers wil ik apart noemen om hem te bedanken voor onze vruchtbare samenwerking in het "IDAPS"-project en zijn persoonlijke bijdrage aan de technische software ontwikkeling ten behoeve van de Electron Spin Echo spectrometer opstelling.

Helaas staat het promotie reglement niet toe Prof. E. de Boer en Dr. C.P. Keijzers persoonlijk te bedanken voor hun intensieve begeleiding en ondersteuning tijdens het promotieonderzoek. Wel is het toegestaan de gehele Afdeling Molecuulspectroscopie te bedanken voor hun collegialiteit en de prettige werksfeer die ik heb ondervonden gedurende mijn dienstverband.

Verder wil ik alle dienstverlenende afdelingen van de Faculteit der Wiskunde en Natuurwetenschappen bedanken voor de vakkundige assistentie bij het tot stand komen van dit proefschrift, te weten, de beide instrumentmakerijen (o.l.v. Henk Verschoor en Paul Walraven), de afdeling Illustratie (o.l.v. Wim Verdijk) en de afdeling Fotografie (o.l.v. Huub Spruyt).

Tot slot wil ik Annie Martens bedanken voor de snelle en vakkundige verwerking van het fotozetwerk van dit proefschrift.

Aan mijn ouders

CONTENTS

CHAPTER I

Introduction

I.1 Pulsed EPR

Time resolved EPR has undergone a significant development during the last decade. A great variety of time resolved techniques is currently used in the study of the structure and dynamics of paramagnetic centres in all kinds of materials. A technique with increasing popularity is pulsed EPR which will be the subject of this thesis.

Although EPR shares its theoretical basis with NMR, it did not experience the same spectacular development into Fourier transform techniques. This is caused by the large energies involved in electron spin interactions which give rise to spectral widths in the order of 10-50% of the carrier frequency as opposed to the ppm scale which applies to NMR. A second reason is the fact that electron-spin relaxation times are orders of magnitude shorter than the nuclear spin relaxation times which are usually encountered in NMR. These properties put extreme demands on the experimental and technical conditions. The first pulsed EPR studies were confined to esoteric compounds with long relaxation times and narrow linewidths (1,2). The last few years, however, microwave equipment became available that extends the applicability of pulsed EPR techniques to biological systems, polymers, catalists, short lived radicals, transition metal complexes and photo-excited triplets (3-8).

As opposed to pulsed NMR where Free Induction Decays (FID's) can be detected, in pulsed EPR usually echo techniques are employed since - because of the large spectral widths and linewidths - the FID appears usually on a timescale which is too short for detection. FID experiments in EPR are, therefore, limited to compounds like free radicals and one-dimensional conductors (9). Because of the lower limit in pulse length, in most applications only *one* EPR resonance line at a time can be investigated. From here on we will use the name Electron Spin Echo spectroscopy (ESE) in order to indicate this distinction from pulsed NMR.

Echo experiments are widely used in NMR and in laser spectroscopy for the determination of relaxation times and because specific pulse experiments can invert dominant interactions and can reduce or even eliminate their effect on the signal (10-11). In ESE two- and three-pulse techniques are employed almost exclusively. With these techniques, the relaxation times T_1 and T_2 can be determined and small hyperfine interactions of the electron spin with surrounding nuclei can be measured (12-13). This last technique is called Electron Spin Echo Envelope Modulation (ESEEM) and it is the main subject of this thesis. The ESEEM technique can be regarded as an alternative for the CW-ENDOR technique which is still the most popular technique for measuring small hyper-

fine interactions (14). In the ENDOR method the intensity of a (partly) saturated EPR line is continuously monitored, while sweeping with a strong RF-field through the NMR transitions of the nuclei which are coupled to the paramagnetic centre. When a nuclear spin transition is induced, the EPR line will be desaturated to some extend and this results in an increase of the EPR intensity. Despite the great merits of this technique, problems arise in some cases:

a) Since it is a steady state technique short lived paramagnetic centres cannot be investigated.

b) Due to the subtle balance of relaxation times that is needed for detection of the CW-ENDOR effect, the technique can sometimes only be applied in a narrow temperature window. For the same reason the ENDOR intensities are influenced by the relaxation times and they are not suitable for the analysis of the number of nuclei that is responsible for the ENDOR effect.

c) For low frequencies (< 1 MHz) the ENDOR effect is very small. Moreover, technical problems arise such as microphonics of the RF-coil and the generation of higher harmonics in the RF-circuits.

The first two problems can be circumvented by using the pulsed form of ENDOR: the ESE-ENDOR technique which is described in section I.4. Especially the last problem can be tackled with the ESEEM technique which has some attractive features. These are discussed in the next two sections.

The theory involved in describing pulsed experiments is well established and uses the density matrix formalism. This treatment, however, is not very illustrative for non-specialists. Therefore, in the following sections (semi) classical descriptions are presented of the spin-echo phenomenon, the nuclear modulation effect and the ESE-ENDOR effect. For a thorough quantum mechanical treatment the reader is referred to the literature (15) and to Chapter IV where some computational aspects of the theory are considered.

I.2 Spin Echoes

The description of a spin echo experiment is based on the concept of an inhomogeneously broadened resonance line. Figure 1a shows how an inhomogeneous line can be considered to consist of a series of "homogeneous spinpackets" each with its own Larmor precession frequency, ω_i, around the centre frequency ω_0. The latter corresponds to the DC magnetic field B_0. In a frame that rotates around the direction of B_0, defined as the z-axis, with the frequency ω_0 the precession frequency is $\omega_i' = \gamma B_i - \omega_0$, where B_i is the effective

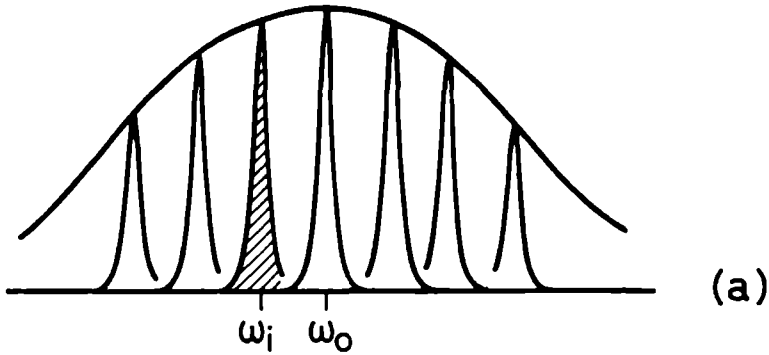

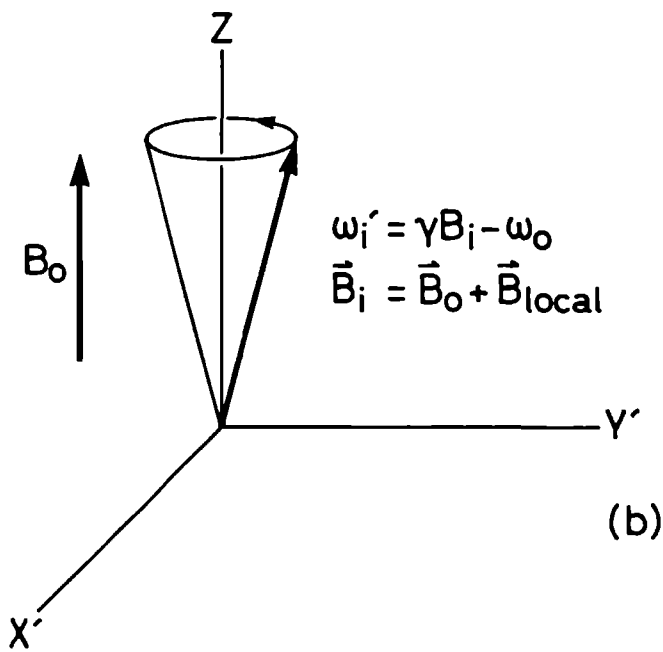

Figure 1 The E P R line of a paramagnetic centre in solid state is inhomogeneously broadened The total linewidth can vary from 1 to 50 Gauss The individual spin packets have linewidths in the order of 1 mG (a) Each spin packet can be considered independently from the others having its own Larmor precession frequency (b)

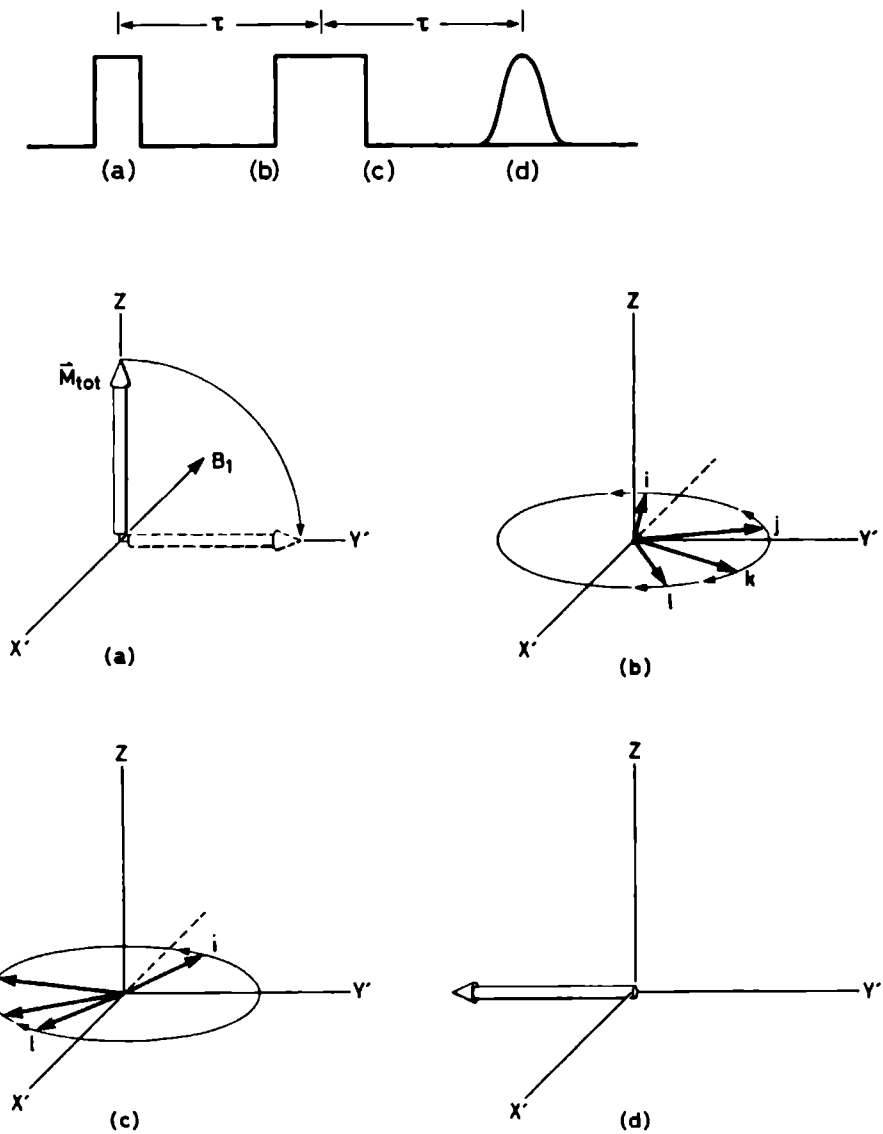

Figure 2. Magnetisation of spin packets i,j,k, and l during a two pulse experiment. a) during the 90° pulse; b) during the waiting time τ; c) after the 180° pulse; d) at the time of the echo (time τ after the 180° pulse).

magnetic field at the site of spin packet "i". All individual spin-magnetic moments belonging to spin packet "i" precess with the same frequency but with different phases. Therefore, in a steady state, the resultant magnetic moment of every spinpacket is aligned along B_0 (figure 1b).

Subsequently we consider the effect of microwave radiation with frequency ω_0 and polarized in the x-y-plane. The oscillating B_1-field can be decomposed into two counterrotating components of which one is rotating in the same direction as the Larmor precession of the spins (the other one is neglected). Hence, in the rotating frame B_1 is a steady field, defined along -x', as is indicated in figure 2a. If the microwave radiation is intense enough the resultant magnetic field in the rotating frame is oriented along B_1 for every spin-packet. The magnetisations M_i start to precess around this new effective field after switching on B_1. When the microwave radiation is present just long enough to flip the magnetisations M_i into the x-y-plane, the pulse is defined as a 90° pulse. Since the different spin packets have different offset frequencies ω_i', they start to dephase immediately after the pulse (fig. 2b). This process is called the Free Induction Decay (FID) and in typical ESE-applications the dephasing will be complete within 50 ns (corresponding to a linewidth of 7 Gauss) which is too short to detect with the present equipment.

From this FID an echo can be generated by means of a second microwave pulse after a waiting time τ which rotates the spins over 180° (fig.2c). This π-pulse is equivalent to a reflection of the dephased pattern in the x'-z-plane. Also the time-behaviour is inverted in this way and the spinpackets refocus after the same waiting time ,τ, into an echo which is called the "two-pulse" or

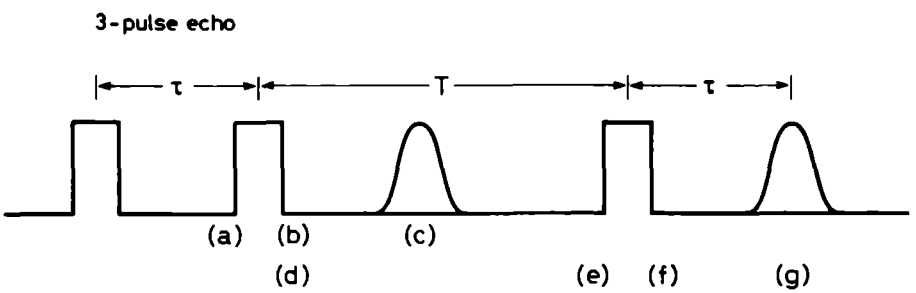

Figure 3. Magnetisation of spin packets i,j,k,l and m during a three-pulse sequence. (a) after the first 90° pulse (along -x') and the waiting time τ; (b) after the second 90° pulse, (c) the x'-components give rise to a Hahn-echo (or "eight-ball echo") at time τ after the second 90° pulse, (d) the projection of the magnetisation components on the x'z-plane after the second 90° pulse; (e) after a longer waiting time T only the z-components will be left, (f) the third 90° pulse brings these components back into the x'y'-plane (g) after time τ they give rise to the stimulated echo It can easily be shown that the x'y'-magnetisation components at this time are lying on a circle defined by $M_x^2 + (M_y + 1/2)^2 = 1/4$.

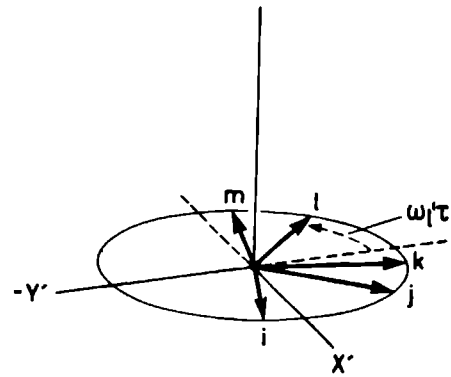

(a)

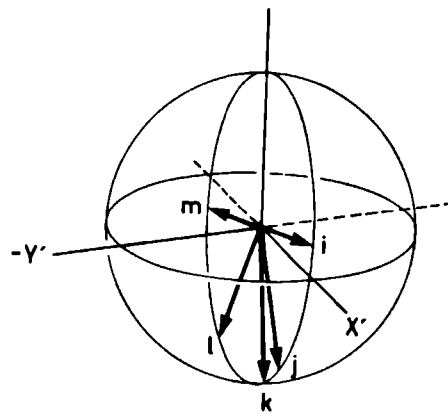

(b)

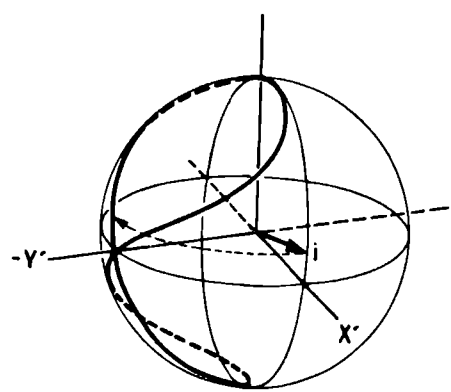

(c)

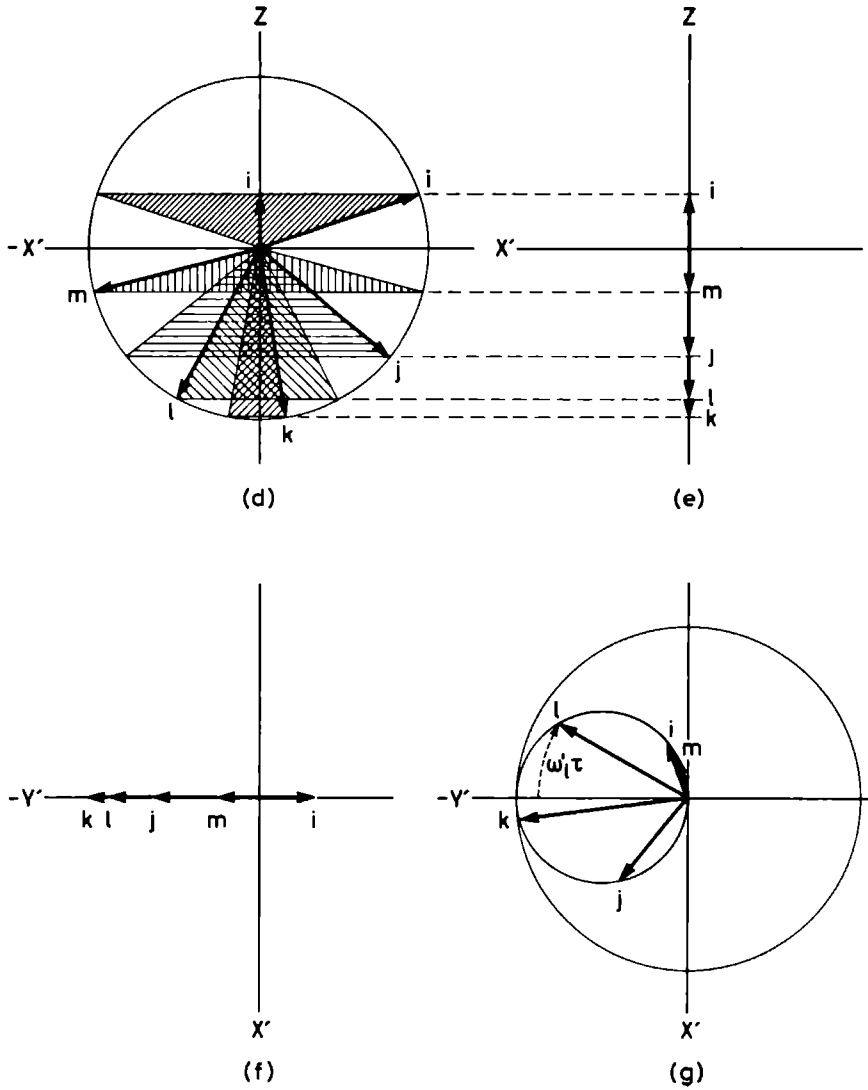
Z
i
i
-X′
m
j
l
k
(d)
Z
i
X′
m
j
l
k
(e)
-Y′
k l j m i
X′
(f)
l
i
m
$\omega_1'\tau$
-Y′
k
j
X′
(g)

"primary" echo (fig. 2d). Monitoring the two-pulse echo intensity as a function of τ offers a method of measuring the "phase-memory time" or homogeneous T_2 of the spin system. Note that the existence of inhomogeneities in the spin system is essential for the echo-phenomenon! The length of the pulses, however, is not essential since for any length there are components of the dephasing pattern which contribute to the echo. The maximum echo intensity is obtained with the 90° - 180° sequence of pulses, of course.

Another important pulse sequence is the three-pulse experiment which is scetched in figure 3. In this sequence the π-pulse is so to say split into two $\pi/2$ pulses. After the first of these $\pi/2$ pulses, the +y' components of the dephased magnetisation pattern (fig. 3a) are stored along the -z-axis where they remain during the waiting time T, and the x-components generate a socalled "Hahn echo" (16) after time τ (figure 3b,c). The third microwave pulse brings the M_z components back into the xy-plane where they continue their time evolution and give rise to a "stimulated" echo at time τ after the third pulse (fig. 3d-g). As is indicated in figure 3c and 3g, the Hahn echo and the stimulated echo have somewhat "diffused" magnetisation patterns. Furthermore, both have half the intensity of the "two-pulse" echo. The characteristic time of the stimulated echo decay as a function of the waiting time, T, is much longer than the phase memory time, T_M, since the "phase information" is stored along the z-axis where it is less sensitive to phase destructive spin-spin interactions. In general, this relaxation time has a value inbetween T_1 and T_M.

The primary echo and the stimulated echo experiment are the main tools of the ESE-spectroscopist. In both experiments the nuclear modulation effect can be observed.

I.3 The nuclear modulation effect

When a paramagnetic centre is coupled to surrounding nuclear spins via anisotropic interactions which do not differ more than one order of magnitude from the nuclear Zeeman energy, the nuclear spin transition frequencies (NMR-transitions) can be observed as modulations on the Electron Spin Echo decay generated in both, two- and three-pulse experiments. We will discuss the origin of this effect using a semi-classical description.

Consider a spin system with one electron S = 1/2 and one nucleus I = 1/2 coupled with an anisotropic hyperfine interaction. The energy level diagram consists of four levels (Figure 4). If the hyperfine interaction was isotropic, only the regular EPR transitions 1-3 and 2-4 would be allowed. However, because of the anisotropic interaction the nuclear spin states are mixed and, therefore, also the nuclear spin flip transitions 1-4 and 2-3 are allowed to some extent. In case of short microwave pulses, all transitions are excited equally and coherently. Each transition represents a spin packet with its own Larmor

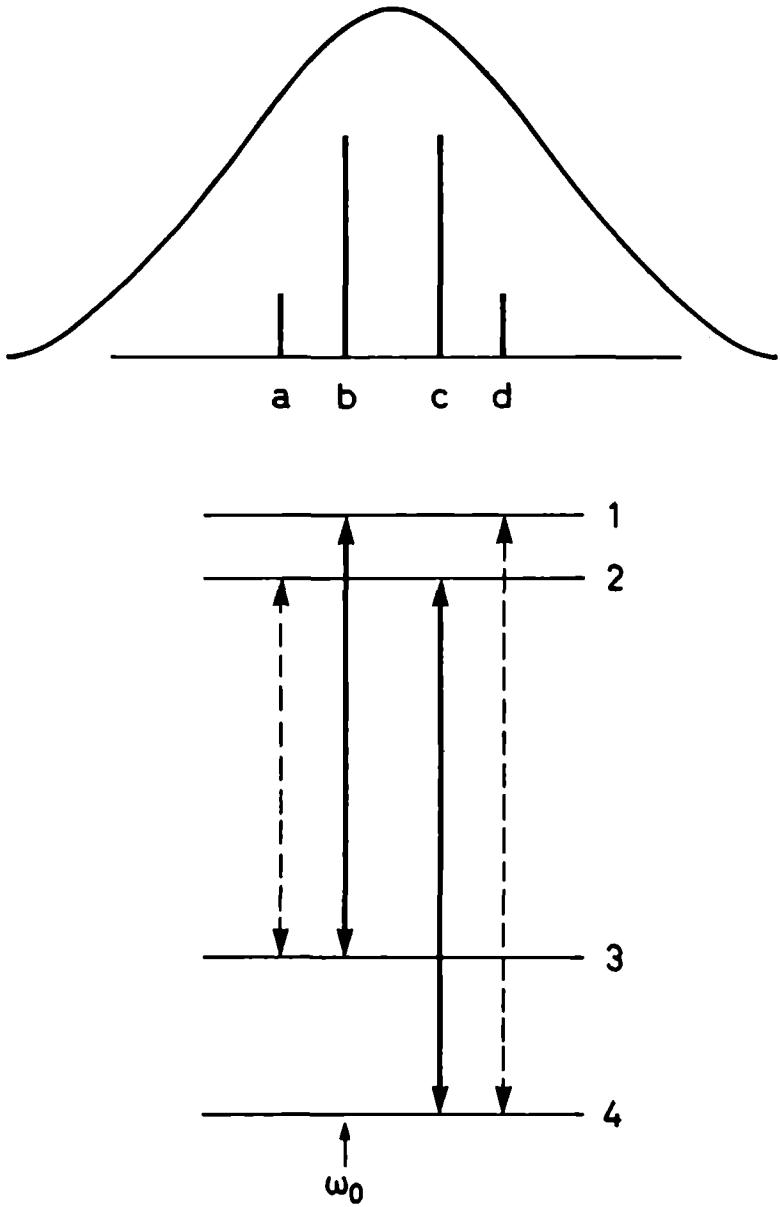

Figure 4. Energy-level diagram and the corresponding spin packets a,b,c, and d for an electron S=1/2 and a nucleus I=1/2.

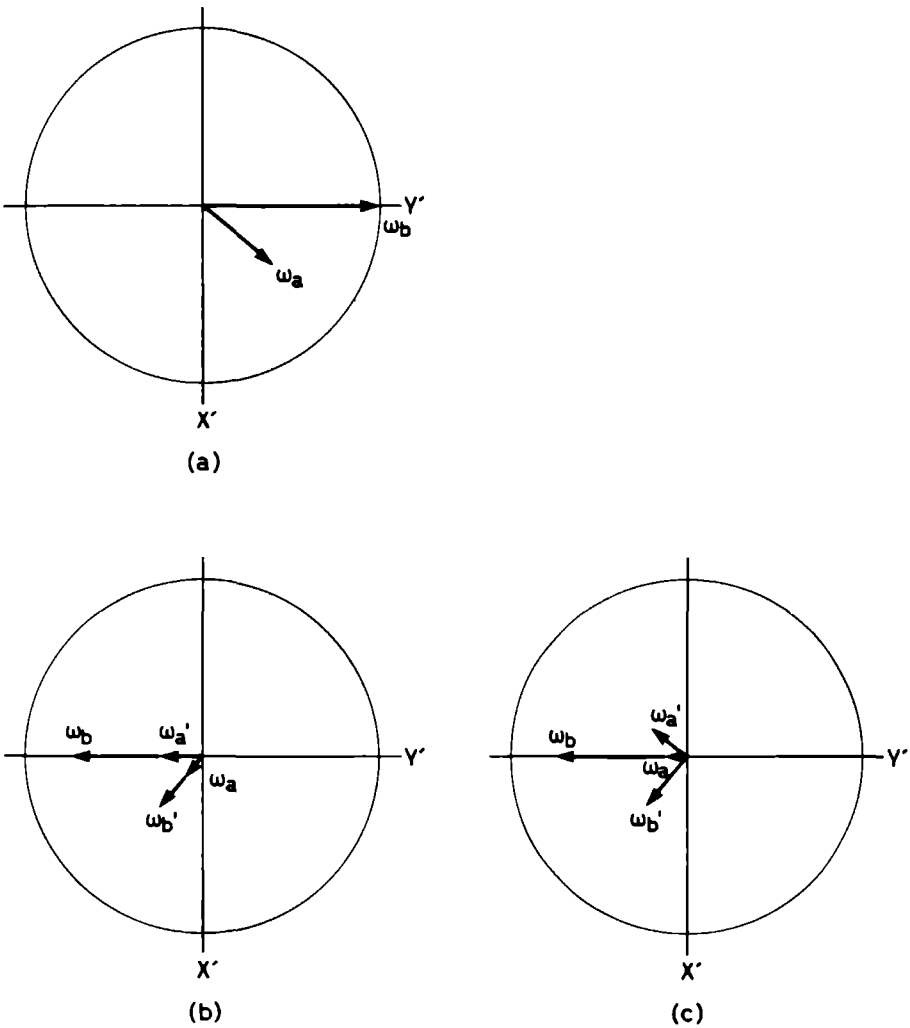

Figure 5 Time behaviour for the magnetisation of "forbidden" spin packet a and "allowed" spin packet b during a two-pulse echo sequence (a) time τ after the 90° pulse, (b) after the 180° pulse, (c) at the time of the echo

frequency. The fact that the microwaves can induce transitions starting at the same level but ending at different ones is called "branching of transitions" and it is this effect that is responsible for the nuclear modulation phenomenon. This branching of transitions can be translated into the classical picture by imagining that during each pulse a spin packet is split into several components which have one level in common with the original "allowed" one. To illustrate the effect we follow spin packets "a" and "b" (figure 4) during a two pulse sequence. We assume that spin packet "b" is at resonance (ω_0) and is, therefore, fixed in the rotating frame (figure 5a). After the $\pi/2$ pulse both "a" and "b" are in the x'y' plane and "a" starts to dephase as is indicated in figure 5a. After the π pulse "b" is inverted along the -y' axis. Because of the branching of transitions also a component with frequency ω_a (and intensity λ) has been formed which we shall indicate with "a'". The original "a"-component will refocus in the usual way to contribute to the echo at time τ after the last pulse. However, the a' component will have its maximum contribution to the echo only if during the refocussing process in time τ it precesses an integral number of times i.e. $(\omega_b - \omega_a)\tau = n \cdot 2\pi$). Therefore, the echo envelope as a function of τ is modulated by a function $(1 - \lambda cos(\omega_b - \omega_a)\tau)$. The same holds for all other combinations of spinpackets. Therefore, we can expect all NMR frequencies to occur in the echo envelope. This phenomenon is called the quantum beat effect. By Fourier transformation of the echo-envelope an ENDOR like spectrum is obtained. The intensities of the "ENDOR" lines, however, are completely determined by the "forbidden" EPR transition-probabilities. As mentioned already both, two- and three-pulse, echo experiments show the nuclear modulation effect. In most cases the three-pulse technique is used because it offers some advantages over the two-pulse experiment:

- In the two-pulse experiment sum and difference frequencies of NMR transitions occur which may cause crowdy spectra, whereas the three-pulse experiment yields only the basic NMR frequencies.

- Since the two-pulse echo decay time is determined by the homogeneous T_2, which is rather short for most interesting materials, the modulations will disappear on a short timescale and they are, therefore, difficult to analyse. The three-pulse echo decay as a function of T extends over a much longer time period (typically 500 μs for diluted paramagnetic centres in single crystals) and is, therefore, better suited for transformation to the frequency domain.

I.4 ESE-ENDOR

Another application of the three-pulse echo method is the ESE-ENDOR effect which is induced by applying RF-energy during the waiting time T between the second and third pulse. When an NMR-frequency is "hit" the stimulated echo is reduced as a result of the frequency changes in the EPR spin packets. A qualitative understanding can be obtained as follows:

After the first two pulses the magnetisation "cones" will average in the x'y'-plane (fig. 3d) and a pattern of M_z components remains. The z-component of a spin packet depends on how its precession frequency "fits" in the waiting time τ. E.g. spin packets exactly at resonance will be oriented along the negative z-axis whereas spin packets with the frequency in the rotating frame $\omega_i' = \pi/\tau$ will be oriented along the positive z-axis. In figure 6 the M_z'-components are plotted as a function of the frequency ω_i'. In a standard three-

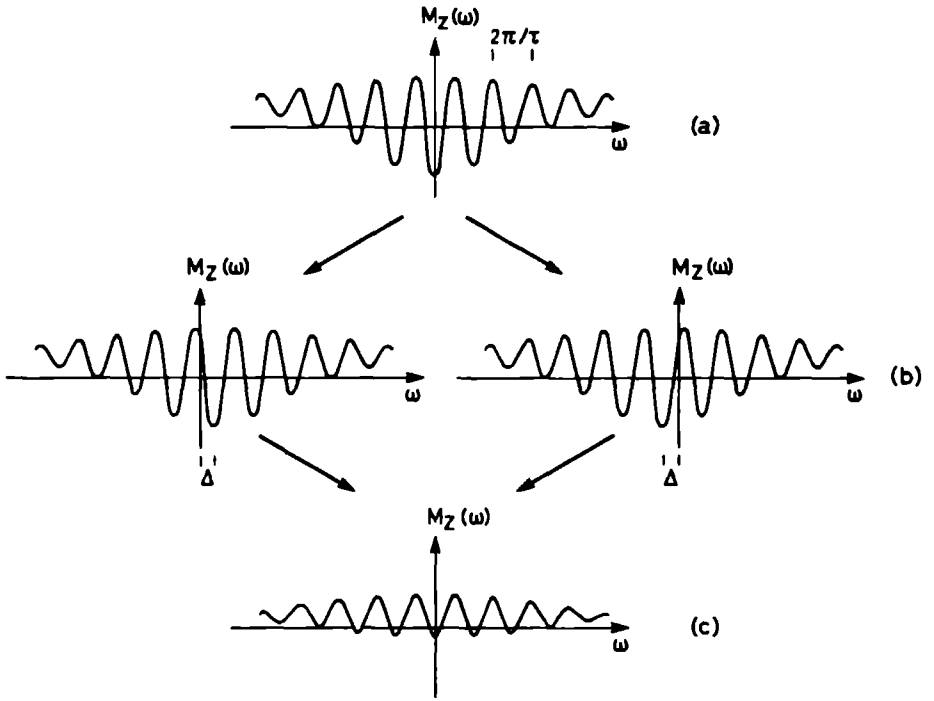

Figure 6. The pattern of M_z-components as a function of the offset frequency of the spin packets ($\omega = \omega_i'$) after two 90° pulses have been applied with a time space of τ (a) When a nuclear spin transition is induced, the frequency pattern will shift either up or downwards with an amount equal to the hyperfine energy $\Delta = \omega_{hyp}$ (b) Unless $\omega_{hyp} = (2n-1)\pi/\tau$ the frequency pattern will be blurred (c) and the echo intensity is reduced

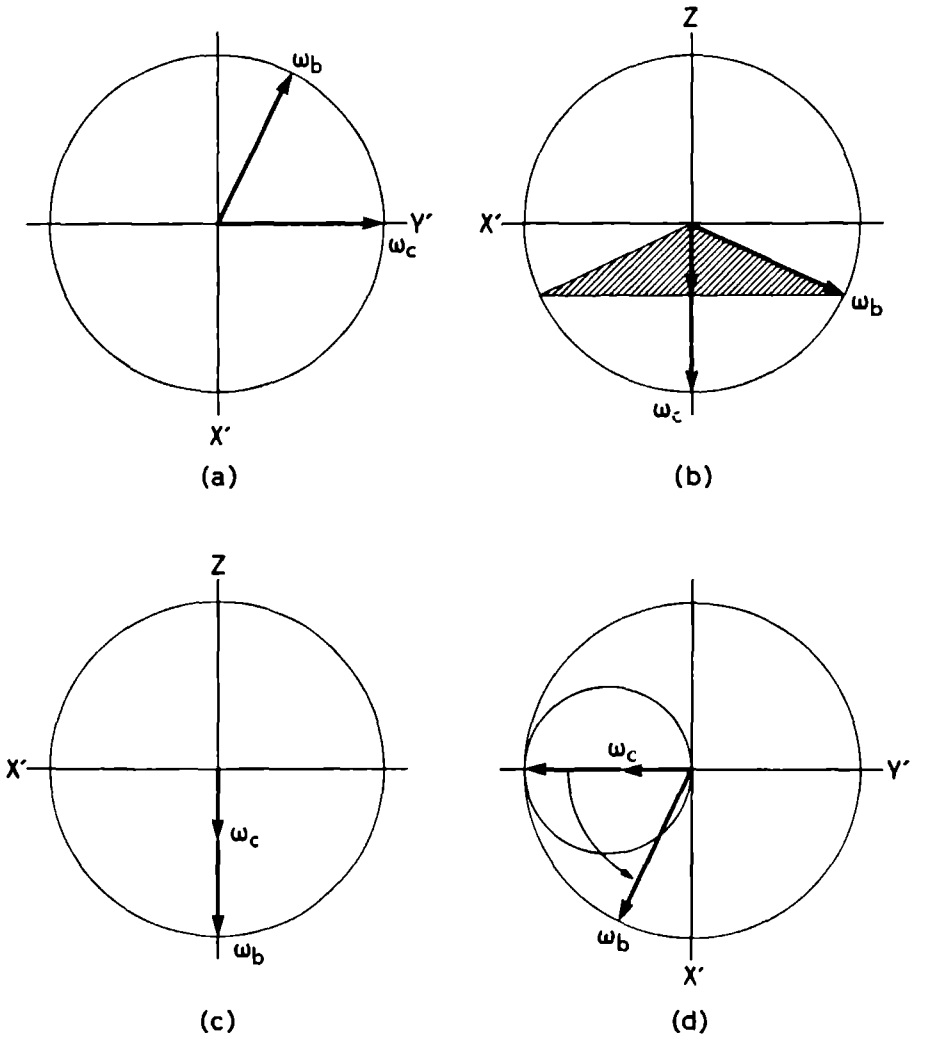

Figure 7 Time behaviour for the magnetisation of spin packets b and c during an ESE-ENDOR sequence (in this description, spinpacket c is on resonance) (a) time τ after the first 90° pulse, (b) after the second 90° pulse , (c) after the RF-pulse where ideally the frequencies ω_b and ω_c are interchanged, (d) at the time of the stimulated echo Note that spin packet "b" (with intensity "stolen" from "c") is dephasing out of the area of the three pulse echo which is indicated by the circle, this will reduce the echo intensity as compared to the situation where no RF-pulse would be applied

pulse experiment the whole pattern refocusses at time τ after the last pulse (fig. 3g). When during the RF pulse a nuclear spin transition is hit, e.g. transition 1-2 in figure 4, the frequency of spin packet "b" will change to that of spin packet "c" and vice versa. The frequency difference is $\omega_{hyp} = \omega_{1-3} - \omega_{2-4}$. Referring to figure 3 this means that a number of spin packets undergo a frequency shift of ω_{hyp} up or downwards (this is indicated as a shift Δ in figure 6b). Therefore, the pattern of M_z components will be blurred in most cases (fig. 6c), reducing the effective intensity of M_z components which will contribute to the echo. For spin packets "b" and "c" this is illustrated in figure 7. Only when $\omega_{hyp} = n \cdot 2\pi/\tau$ the pattern is retained and the echo intensity is unaffected. In other words the echo intensity will be modulated by a factor $\gamma \cos\omega_{hyp}\tau$ where γ is the effectiveness of the NMR transitions. The "blind spots" at $2n\pi/\tau = \omega_{hyp}$ are the only drawback of the ESE-ENDOR technique. One can circumvent this problem by taking ENDOR spectra at different τ-values. When it is possible to do a real two-dimensional experiment i.e. taking ESE-ENDOR spectra as a function of τ, this modulation can be turned into an advantage since a Fourier transformation of the τ domain will yield cross-peaks which correlate different ENDOR transitions belonging to the same nucleus (17).

I.5 New developments

Although the three-pulse ESEEM signal usually extends over a much longer time period as compared to the two-pulse ESEEM signal, still serious problems may arise during spectral analysis. The main problem is the loss of the first part of the data due to the spectrometer dead time. This causes artefacts (sidelobes and phase distortions) in the frequency domain spectrum obtained by Fourier transformation. Especially in the case of powder samples where the modulations are damped quickly because of destructive interference, these artefacts inhibit a proper data analysis. In order to minimize the artefacts one may consider a tranformation technique where one remains maximally noncommittal about the unrecorded data so that the frequency spectrum is essentially unaffected by the loss of initial data. A transformation of this kind exists and is extensively used in geophysics, neurophysics, radar, etc (18). The so-called "Maximum Entropy Method" and the related "Auto Regressive Modeling" technique have been applied recently to ESEEM-signals (19,20). The basic assumption made in these techniques is that the signal is stationary, i.e. the signal has a time independant normal probability density. To satisfy this condition, in most cases preprocessing of the data is necessary (multiplication with the inversed decay function). Although the Signal to Noise Ratio and the spectral resolution of these methods are far superior to the FFT-technique, problems arise such as increased computing time and the occurence of artefacts in the frequency domain: shifting and/or splitting of peaks.

Another way of analysing the time domain independently from the initial data fragment, is the "Linear Prediction with Singular Value Decomposition" method (21). In the LPSVD-procedure the data is modelled to a series of damped sine waves with arbitrary *frequency, intensity, phase, and damping factor.* The advantage of this method is that for every spectral line these four parameters become available. On the other hand, in many cases the ESEEM signal is not built up from damped sine waves. In these cases a lot of parameters (without physical meaning) are needed to fit the data. If, however, the fit is good enough, the parameters can be used to extrapolate the ESEEM signal back into the dead time region. Subsequently, the "polished" data can be Fourier transformed without artefacts.

Apart from the data analysis approach which reduces the effect of the dead time, also several efforts have been made to reduce the instrumental dead time itself. Many groups use low Q microwave resonators (see Chapter III) sometimes combined with active or passive delay lines to reduce the resonator ringing time (22,23). Also phase-cycling methods are employed to reduce the dead time in a three pulse ESEEM experiment (see section II.1).

Very recently a new ESE technique has been reported (24). In the so-called "Extended Time Excitation" (ETE-ESE) technique the 90° pulse of a two pulse sequence is replaced by a long weak selective pulse, whereas the 180° pulse remains short and intense (non selective). Due to the linear response properties of most electron spin systems, the whole two-pulse ESEEM signal will be present in the extended echo response. In other words, this method offers a way of obtaining the two-pulse ESEEM signal in a single transient! This opens possibilities of increasing the sensitivity of the ESEEM experiment by orders of magnitude. It remains to be seen, however, whether the usually poorer information content of the two-pulse ESEEM signal can be compensated for with the increased sensitivity.

References

1. R.J. Blume, Phys. Rev. *109*, 1867 (1958)
2. L.G. Rowan, E.L. Hahn, and W.B. Mims, Phys. Rev. *137*, 61 (1965)
3. W.B. Mims and J. Peisach, Biochemistry *15*, 3863 (1976)
4. D. Davidov, F. Moraes, A.J. Heeger, F. Wudl, H. Kim, and L.R. Dalton Solid State Commun *53*, 497 (1985)
5. L. Kevan in "Time Domain Electron Paramagnetic Resonance" (Eds, L. Kevan and R.N. Schwartz, John Wiley, New York, 1979), Chap. 8.
6. J.R. Norris, M.C. Thurnauer and M.K. Bowman, Adv. Biol. Med. Phys. *17*, 316 (1980)
7. T.S. Lin, Chem. Rev. *84*, 1 (1984)
8. E.J. Reijerse, M.L.H. Paulissen, and C.P. Keijzers, J. Magn. Reson. *60*, 66 (1984)
9. Bruker Report 1/1983 (page 31) ER 280 I Pulse ESR Spectrometer.
10. I.D. Abella, N.A. Kurnit and S.A. Hartman, Phys. Rev. *141*, 391 (1966).
11. U. Haeberlen, "High Resolution NMR in Solids, Selective Averaging" (Academic Press, New York 1976).
12. W.B. Mims, Phys. Rev. *B5*, 2409 (1972); Phys. Rev. *B6*, 3543 (1972).
13. W.B. Mims, "Electron Spin Echoes", in Electron Paramagnetic Resonance, edited by S. Geschwind (Plenum Press, New York, 1972).
14. L. Kevan and L.D. Kispert, "Electron Spin Double Resonance Spectroscopy", (Wiley Interscience, New York, 1976).
15. J. Vanier, Basic Theorie of Lasers and Masers, A Density Matrix Approach (Gordon and Breach, New York, 1971).
16. E.L. Hahn, Phys. Rev. *80*, 580 (1959)
17. R.P.J. Merks, Ph.D. Thesis, Delft University Press, 1979
18. Topics in Applied Physics, Vol. 34, (Ed. S. Haykin, Springer, Berlin, 1979).
19. D. van Ormondt and K. Nederveen, Chem. Phys. Lett. *82*, 443 (1981)
20. H. Barkhuijsen, R. de Beer, E.L. de Wildt, and D. van Ormondt J. Magn. Reson. *50*, 299 (1982)

21. H. Barkhuijsen, R. de Beer, W.M.M.J. Bovee, and D. van Ormondt J. Magn. Reson. *61*, 465 (1985)

22. J.L Davis and W.B. Mims, Rev. Sci. Instrum. *52*, 131 (1981)

23. P.A. Narayana, R.J. Massoth, and L. Kevan, Rev. Sci. Instrum. *53*, 624 (1982)

24. L. Braunschweiler, Thesis ETH Zurich (1985)

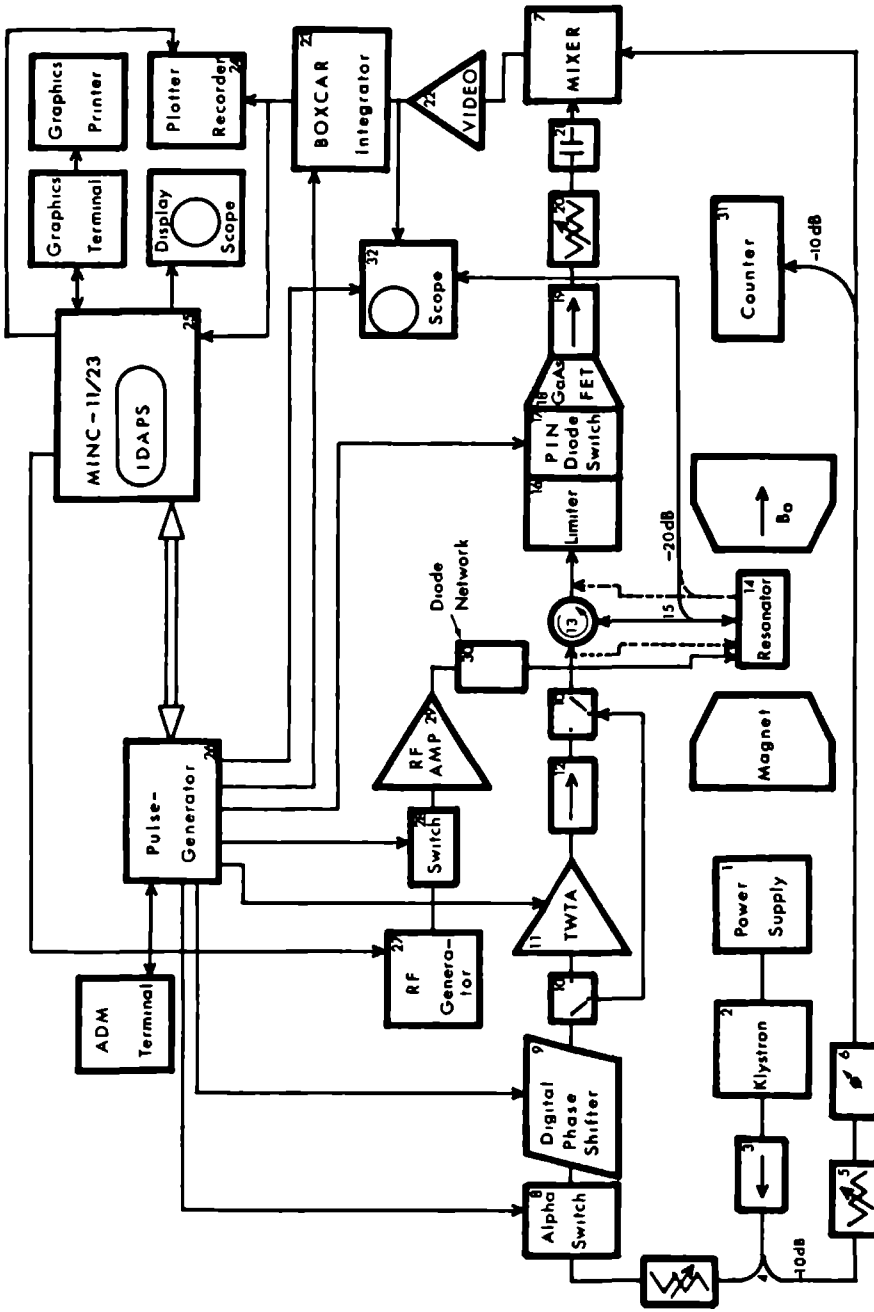

Figure 1. Block diagram of the ESE-(ENDOR) spectrometer.

CHAPTER II

Instrumental

II.1 The spectrometer hardware

Since the ESE spectrometer of our department has been described only briefly in the literature (1) and because during the last year some improvements have been made we give a fairly detailed description of the instument in its present condition. In figure 1 the complete block diagram of the spectrometer is presented. The components are labelled with numbers <n> which will be referred to in the following description.

The microwave source is a .7W klystron <2> fed by a Narda universal power supply <1>. Via an isolator <3> and a directional coupler <4> 10% of the power is directed to the reference arm. The reference signal is led to one input of a double balanced mixer <7> via an attenuator <5> and a manual phaseshifter <6>. Part of the reference signal is used for monitoring the klystron frequency <31>. 90 % of the microwave signal is led via an attenuator, an "Alpha Instuments" PIN-diode switch <8>, a digital phaseshifter <9>, and a manual bi-throw switch <10> to the input of a high power (1 kW) Travelling Wave Tube Amplifier (TWTA) <11>. The microwave switch, the digital phaseshifter and the TWTA are controlled by a homebuilt fast pulse-generator <26>. For tuning purposes the microwave power can be led around the TWTA via two bi-throw switches <10>. The high power microwave pulses are fed into the resonator <14>. In case of a transmission type resonator the transmitted signal is directly fed into the receiver circuit; in case of a reflection type resonator this is done via a circulator <13>. In both cases 1% of the signal is tapped via a directional coupler <15> for diagnostic purposes.

The detection circuit consists of a low noise GaAs-FET amplifier (30dB) <18> which is protected from the high power excitation pulses by a limiter <16> and a microwave switch <17> (controlled by the pulse generator <26>).

The amplified (echo) signal is fed into the second input of the double balanced mixer <7> via a variable attenuator <20> and a DC-block <21> (inserted to prevent groundloops).

The output signal of the double balanced mixer is directed to a broad-band video amplifier <22>. Finally the amplified echoes (total of 70 dB amplification) are fed into a Boxcar integrator <23> which is triggered by the pulse generator <26>. The signal can also be monitored on an oscilloscope <32>. The output signal of the Boxcar integrator can be recorded immediately <24> or in most cases it is sampled and stored in a Minc 11/23 laboratory minicomputer <25> where the signals are processed and graphically manipulated.

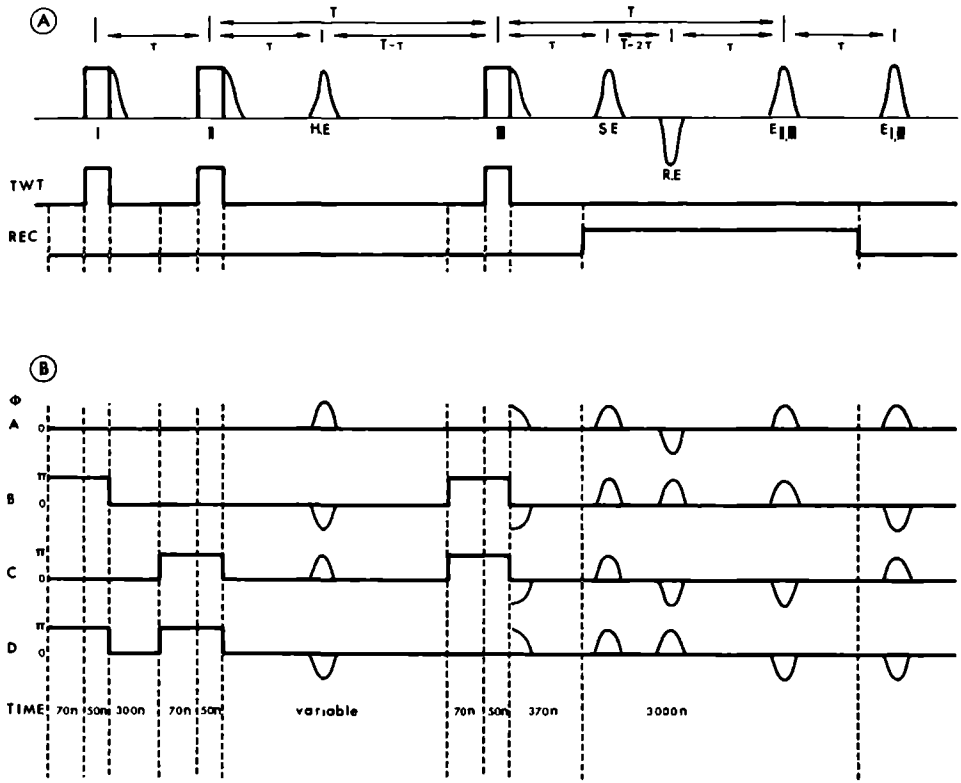

Figure 2. A) Coherent effects in the standard three-pulse experiment: The Free Induction Decays of pulses I, II, and III, the two pulse- or Hahn Echo (H.E.), the three-pulse or Stimulated Echo (S.E.), the Hahn Echo which is refocussed by pulse III (R.E.), the echo formed by pulse II and III ($E_{II,III}$), and the echo formed by pulse I and III ($E_{I,III}$).

B) Timing diagram of a three-pulse experiment with four-step phase cycling. The line indicated with TWT shows the switching of the TWT-amplifier (fig. 1 <11>); The line indicated with REC shows the switching of the receiver circuits (switch <17> and the BOXCAR integrator <23> in figure 1). The gate of the BOXCAR will be tuned to integrate the area of the stimulated echo (SE). The subsequent lines (A-D) indicate the switching of the phase shifter (<9> in figure 1) during the four components of the pulse sequence. As can be inferred from the figure, each component experiment has to be programmed in 11 times, the four components will thus give rise to a 44 time pulse sequence. The bottom line shows a timing used in a typical experiment. The stimulated echo intensities in each component experiment are accumulated in the usual way.

ESE-ENDOR experiments are carried out using a 300W RF-amplifier <29> fed by an RF-sweeper <27> of which the output signal is modulated by an RF-switch <28>. Obviously, the RF-switch is controlled by the pulse gen-

erator <26>.

The philosophy in the design of both, hard- and software, components of the spectrometer is based on the idea of modularity and flexibility. Any module of the system should be upgradable independent of the other modules. The operation of the spectrometer hardware is solely the responsibility of the pulse generator which has its own user-interface. Therefore, tuning, testing and simple experiments can be carried out independent of the mini-computer which in these cases is free for other applications such as the processing of previously accumulated experiments. In fact, in many cases the mini-computer can be replaced by a simple hardware time averaging computer. On the other hand, the pulse generator is able to communicate via a serial line and a simple protocoll with any host-computer, thus making fully computer controlled experiments feasable. The pulse generator has the following specifications:

- A hardware time resolution of 10 ns
- 64 time intervals can be defined ranging from 20 ns to 1 second.
- Each time interval can be incremented (or decremented) by variable amounts (in steps of 10ns) in two stages to support two dimensional experiments.
- During each time, 8 different gates can be operated.

In figure 2a the basic timing sceme of a three-pulse experiment is presented. In order to prevent interference of the stimulated echo with "unwanted" echoes, the waiting time T has to be chosen at least twice as long as the time τ (see fig. 2a). Unfortunately this leads to the loss of the initial part of the signal. By cycling the relative phases of the three microwave pulses, it is possible to cancel the unwanted echoes (2). In figure 2b this pulse sceme that consists of 44 times is illustrated. The pulse sceme employed in our instrument is a modification of the one proposed by Fauth et al. (2) such that the stimulated echo always has a positive contribution to the signal and can be accumulated without the need of post-processing of the data.

II.2 IDAPS: Interactive Data Acquisition and Processing System

As was already mentioned in section II.1 the basic philosophy in the spectrometer design is "modularity and flexibility". Throughout the course of the project the software has been redesigned, polished, cleaned and massaged several times so that it evolved into a large system of routines and modules which can be developed further separately depending on the hardware changes

and future types of experiments. The software was written on a lab-computer (MINC 11-23) in PDP-11 assembler under the operating system RT-11. The complete description is beyond the scope of this thesis and the interested reader is referred to some internal reports (3). Some general aspects of the design, however, may be interesting enough to touch upon in this section.

The IDAPS program is designed as an extendable system of subroutines to control any multidimensional (real time) experiment in which point to point data-acquisition is involved. Such an experiment will produce an analogue signal as a function of one or more experimental conditions (Time, Field, Frequency, Temperature, Orientation.... etc). In the application of Electron Spin Echo Spectroscopy the program has to communicate with several devices (see fig. 1):

- A Boxcar integrator <23> which produces the analogue integral of one or more Electron Spin Echoes. This signal is fed into an A/D channel of the MINC laboratory computer <25>.

- A pulse programmer <26> which will signal IDAPS when the echo signal is ready to be sampled by the A/D converter.

- An RF-sweeper to control ENDOR experiments <27>. This device is connected to a Digital to Analogue Converter (DAC) channel of the MINC laboratory computer.

- A display scope for real time display of the experimental and processed data. This device is driven by two DAC channels of the MINC laboratory computer.

The program can be adapted to work with other experimental setups by writing new device drivers to control the peripheral devices involved in the experiment. Because of the flexibility of the program in its applications, the user interface has to be "device oriented". This means that the program acts as an interface between the user and the equipment which performs the experiment. Therefore, the user has to approach the devices involved individually.

In figure 3 the top level SADT-diagram[†] of IDAPS is scetched. In this diagram both, experimental and user, data-flow are shown. The names in the boxes refer to the five different tasks the system is able to perform. The names on the arrows indicate the type of data which is transferred between the task-modules. Each task is implemented in one or more program submodules.

[†] "SADT" is short for Structured Analysis and Design Technique. "SADT" is a trademark of SofTech corporation of Massachusetts USA.

The monitor task-module interprets the user input which may consist of commands to set system variables (experimental parameters, filenames ... etc), to switch from task environment (mode) or to execute a system function (start an experiment, process data ... etc). In figure 4 the SADT diagram of the monitor is sketched. The procedure to process a user input-string is as follows: When a system function needs user-input, it sets the delimitter list, and sets the "prompt-string" to tell the user (when necessary) what kind of input is requested. The routine "isolate item" checks whether any input-item is left in the input-buffer. If the buffer is empty, the module "get user input" is activated which actually types the promptstring on the console terminal and waits until the user types a response. During the waiting or "idle" loop of the monitor, important system processes are monitored (behaviour of slow sweep-devices, messages from device drivers). The input string typed by the user is stored in the input-buffer. This buffer is passed to the module "isolate item" which will use the delimitter list to select the first input-item. This item is passed to the processing module "convert item" where it is either recognized as a command, or converted into a numerical representation. When the conversion failed, an error message is generated and the input buffer is flushed. The control is passed again to module "get user input" which will repeat the prompt message. In case of a succesful conversion, the system function (which asked for input) is executed and the resulting messages are directed via the "handle ouput" module to the console terminal. The monitor has the following design features.

- The vocabularies are implemented as linked lists (see fig. 5). Therefore, a hierarchic command structure is possible presenting the user only those commands which are appropriate in a given task environment. Moreover, this structure is extremely usefull in building a modular system since every task module can be made to correspond to a node in the vocabulary list.

- The monitor is implemented as a "Threaded Interpretive Language". This in principle enables "macro processing", i.e. supplying the user with the possibility of defining his own commands. In the current system this feature is not yet implemented. A feature of immediate convenience is the fact that the input can be supplied in a continuous string of (abbreviated) commands without the need of waiting for replies or new prompts. Hence the system behaves friendly to both beginning and experienced users.

Figure 3. Toplevel SADT-diagram of IDAPS. Boxes represent actions; arrows represent flow of data, arrows entering downwards carry control data, arrows entering horizontaly carry passive data. Double arrows with dots indicate a feedback or two-ways trafic of data.

Figure 4. SADT-diagram of monitor module. Note that the data-flow is consistent with the top level diagram.

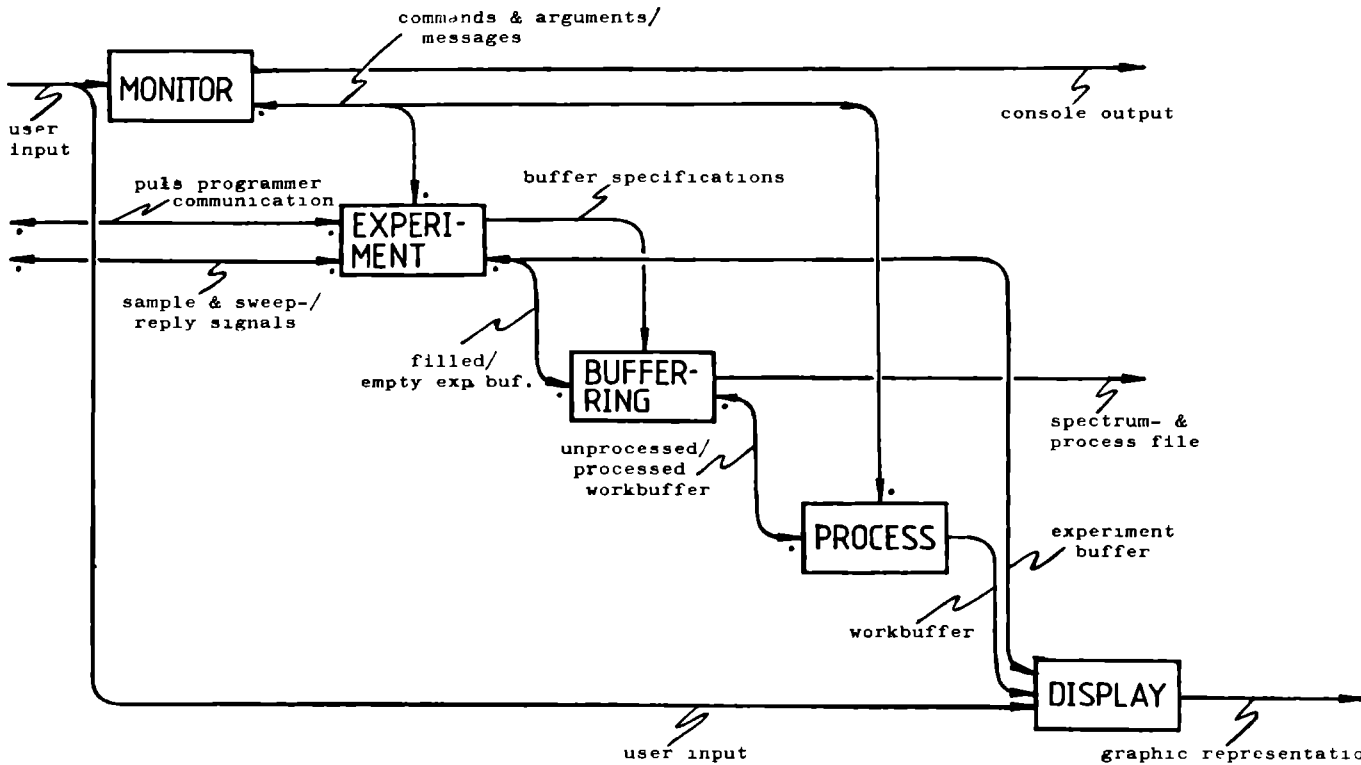
commands & arguments/
messages
MONITOR
user
input
console output
puls programmer
communication
buffer specifications
EXPERI-
MENT
sample & sweep-/
reply signals
filled/
empty exp buf.
BUFFER-
RING
spectrum- &
process file
unprocessed/
processed
workbuffer
PROCESS
experiment
buffer
workbuffer
DISPLAY
user input
graphic representation

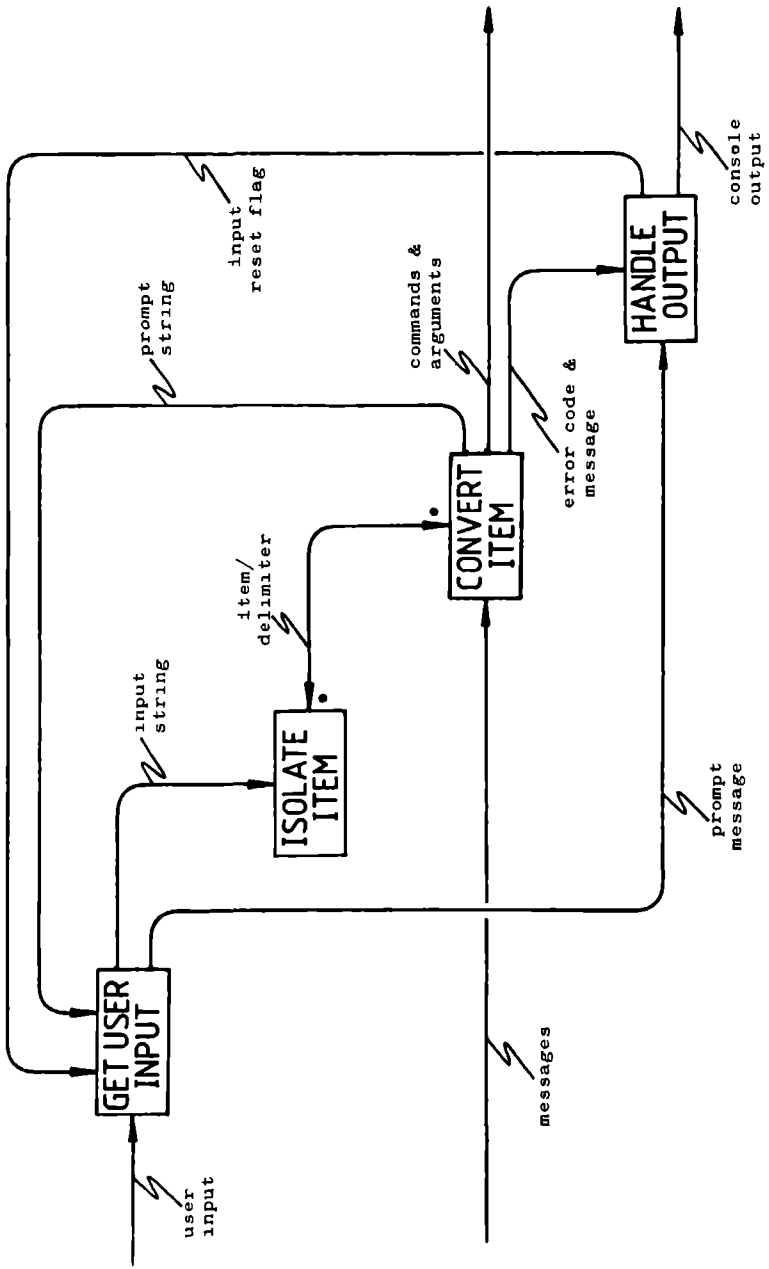
GET USER INPUT
ISOLATE ITEM
CONVERT ITEM
HANDLE OUTPUT
user input
input string
item/ delimiter
prompt string
input reset flag
commands & arguments
error code & message
console output
prompt message
messages

The central data structure of IDAPS is the "Mode Descriptor Block". As an example, the data structure of the SETUP mode and the SWEEP (sub)mode are shown in figure 5. The SETUP mode is reached by typing "SETUP" after initial program loading (other possible commands are "XSTART", "XSTOP", "XRESUME" to start, stop and resume and experiment, respectively). It is the environment which enables the user to setup the parameters of the software device drivers which control the hardware devices that perform the actual experiments. Also the way in which the experimental data is arranged (number and size of buffers, storage device, ...) can be specified in this mode. In other words, the whole experiment is defined in the SETUP mode. The first address of the Mode Descriptor Block is the pointer to the code to be executed by the monitor on recognition of a keyword. In this case, "Mode Code" and "Argument Code" are the executable code. The subsequent field in the "Mode Descriptor Block" are the arguments to this code. The recognisable keywords are stored in the so called "Directory" of the current Mode. Referring to figure 5, let us suppose the system in the SETUP mode. This means that the current prompt message is "setup:" and the current directory pointer points to the linked list of directory entries starting with keywords "sweeper", "receiver", "aquisition".,. Each directory entry consists of a mode-pointer, a pointer to the keyword-string and a pointer to the next directory entry. When the user types the keyword "sweeper", the monitor will recognize this keyword, and execute the corresponding code, "Mode Code". This routine simply changes the current prompt-pointer and the current directory-pointer to the new ones. The monitor will now search in the sweepmode directory. When subsequently e.g. the keyword "dimension" is typed, the related code, "Argument Code" is executed. This code prompts the user to specify a list of numerical arguments: "nsamp" = the number of accumulated in one channel; "nchan1" = the number of channels per buffer in the first dimension of the experiment; "nsweep1" = the number of sweeps over one buffer in the first dimension... etc. After this procedure, the system returns to the SWEEP mode of the monitor. When the keyword "return" is recognized in any mode, the previous mode is restored using the return-pointer in the Mode Descriptor Block. The Mode Descriptor Block may also contain ENTRIES to subroutines which are execut-

Figure 5. Data structure of SETUP mode. Boxes indicate memory locations In this case these memory locations contain adresses of other memory locations such as starting adresses of executable code The names inside the boxes specify the nature of the pointer. The arrows lead to the referred memory locations and the quoted names indicate ascii strings in memory. The "code boxes" at the top contain executable code NIL indicates the end of a linked list The monitor loop reads a command string from the terminal, isolates a command from this string, recognizes this command by searching the directory allong the arrows and then executes the corresponding code. "Modecode" switches the monitor to a new environment by modifying the prompt and the directory pointer

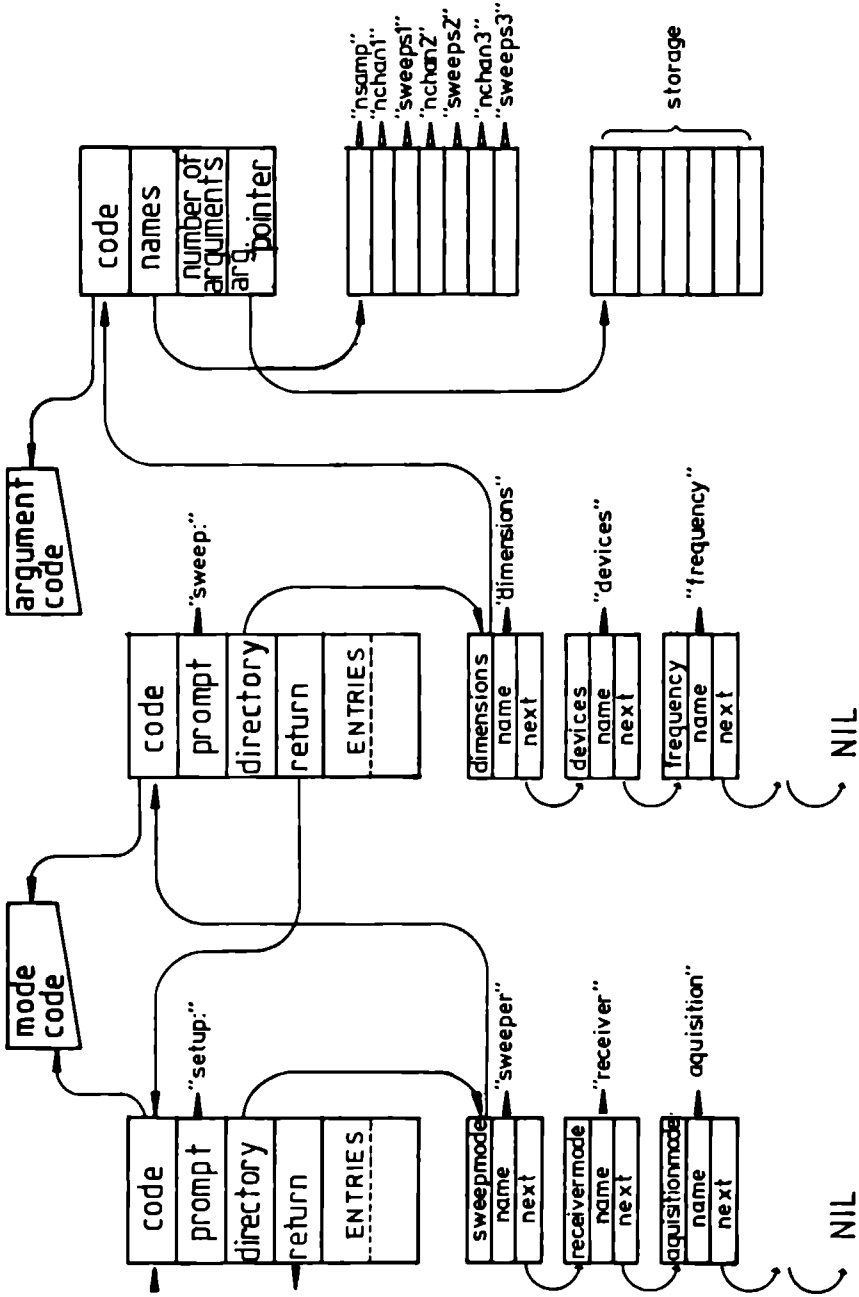
code
names
number of arguments
arg. pointer
"nsamp"
"nchan1"
"sweeps1"
"nchan2"
"sweeps2"
"nchan3"
"sweeps3"
storage
argument code
code
prompt
directory
return
ENTRIES
"sweep:"
dimensions
name
next
"dimensions"
devices
"devices"
frequency
"frequency"
NIL
mode code
"setup:"
sweepmode
"sweeper"
receivermode
"receiver"
aquisitionmode
aquisition"

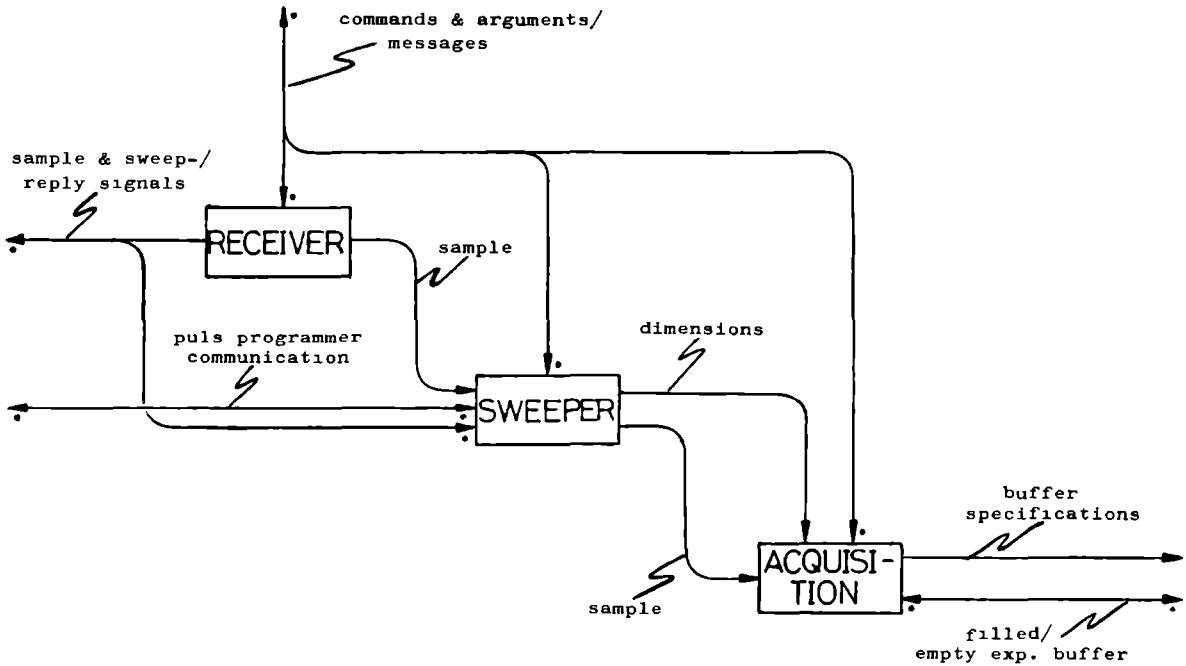

Figure 6 SADT diagram of the experiment module

ed during an experiment via interrupt service routines. This design feature makes it possible to access all routines in any mode in the same way, namely via the first address of the Mode Descriptor Block.

How the experiment is actually controlled, is shown in figure 6 where the SADT diagram of the "Experiment" task-module is presented. During the experiment no user input is needed since the hardware devices communicate with the system via interrupt signals. Therefore, all routines controlling the experiment and the data acquisition are interrupt service routines functioning according to the setup arguments previously supplied by the user.

Three different tasks have to be performed: The device producing the data-samples is controlled by the "receiver-device-driver". In the current implementation this is a simple routine servicing the interrupts generated by the pulse-programmer via the A/D converter. The data-samples are transferred to the "Sweep-device-driver" which stores them temporarily in a ring-buffer (in core). According to the user-specified sweep- & acquisition-arguments (e.g. number of points in each dimension) this module is able to control devices which vary experimental conditions such as the magnetic field strength and orientation, RF-frequency, temperature, timing ... etc. When the specified sweep-device (if any) has its correct value a reply signal is generated and the experiment can proceed.

The acquisition system transfers the data-samples to the experiment buffer according to the same "sweep- & acquisition-arguments". Moreover, options such as double precision, automatic scaling, Vernier and backup generation may be specified.

The experiment buffers are handled by the "Buffer-Ring-System" which is a Memory Management system designed to interact with any direct access files-tructured RT-11 device driver (e.g. Tape, Floppy, Hard Disk and RAM-Disk). This buffer-ring system plays a central role in the performance of IDAPS: both the Experiment and the Process module are enabled to request for spectrum buffers. Therefore, already during the experiment, the user is able to process the spectra and use the display facilities to decide whether the S/N ratio has reached a satisfactory level. At the end of the experiment the data is automatically stored on the userspecified storage device.

The Process module in combination with the Display system allow the user to interactively process and plot experimental data units (i.e. parts of the experiment consisting of one or more sweeps in one dimension). Several processing routines are currently implemented: filtering, apodization, Fourier transformation and phase correction. Once a suitable processing procedure is determined (interactively), a single command is sufficient to process an entire multidimensional experiment and store it under a previously specified name.

References

1) E.J. Reijerse, M.L.H. Paulissen, and C.P. Keijzers, J. Magn. Reson. *60* , 66 (1984)

2) J.M. Fauth, A. Schweiger, L. Braunschweiler, J. Forrer, and R.R. Ernst, J. Magn. Reson. *66* , 74 (1986)

3) A.H. Thiers and E.J. Reijerse, IDAPS Maintainance Document; IDAPS User Manual. Internal Reports, Department of Molecular Spectroscopy, University of Nijmegen.

CHAPTER III[†]

A Variable Temperature ESE-ENDOR resonator for Single Crystal Studies

E.J. Reijerse and A.A.K. Klaassen

Department of Molecular Spectroscopy, University of Nijmegen
Toernooiveld, 6525 ED Nijmegen, The Netherlands

A microwave resonator is described for performing Electron Spin Echo (ESE) and Electron Spin Echo ENDOR (ESE-ENDOR) measurements on single crystals The ENDOR coil arrangement allows the crystal to be rotated about two independent axes The system operates in a temperature range from 4K to 300K using a helium flow cryostate

---

[†] Appearing in "The Review of Scientific Instruments"

III.1 Introduction

ESE experiments require microwave resonators with a low Q (50-500) as opposed to resonators which are used in conventional CW-experiments. In order to compensate for the loss in sensitivity of such a resonator, the filling factor must be increased. In the case of powdered samples one may be able to make a tradeoff between the filling factor and the sample volume using a conventional rectangular TE102 cavity with an enlarged iris in order to reduce the Q-factor, or one may consider using a cylindrical TM110-ENDOR-cavity which combines a relatively low Q (500-1000) with a high ENDOR sensitivity.

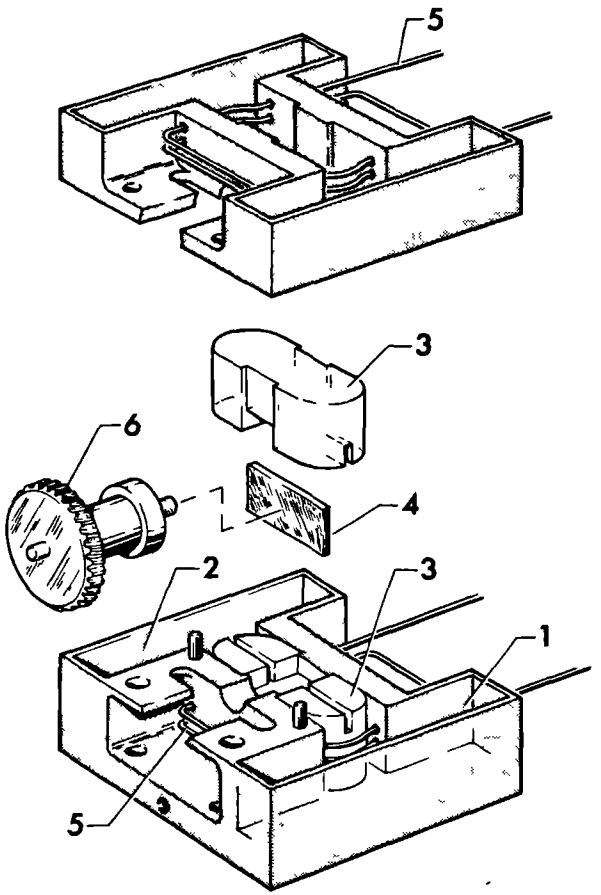

Figure 1 Exploded view of the resonator: 1),2) tapered waveguide sections; 3) perspex support for resonating strip, 4) half-λ resonating strip, 5) ENDOR RF-coil arrangement, 6) sample holder and rotor

In the case of single crystals these tradeoffs usually cannot be made. Resonators which satisfy both criteria of low Q and high filling-factor have been described earlier (1-4). The Q of the resonator described by Davis and Mims (3,4) can be varied from about 50 to 500 and because of the high filling factor this resonator is very suitable for measuring small-volume samples. We describe a modification of this resonator which makes it particularly suitable for doing both ESE and ESE-ENDOR studies on single crystals.

III.2 The resonator

The modified version of the resonator of Davis and Mims (3,4) is shown in fig. 1. In the improved design of Hutchinson, a rotor is introduced with its rotation axis perpendicular to the strip (5). The crystal is mounted at the end of a quartz rod in the center of a rotor. In our setup, the position of a 15 turn pot-meter knob on top of the cryostat is transferred to the rotor via a stainless steel drive-bar and a worm-wheel arrangement (fig. 2). The accuracy of this crystal rotation is about 0.2 degrees which is more than satisfactory for most single crystal studies. Apart from the rotor, also the magnetic field can be rotated with a rotating base magnet. In this way the external B_0 field and the microwave B_1 field are perpendicular in all orientations of the crystal. Since in a pulsed ENDOR experiment it is not essential to keep B_1 and B_2 (ENDOR RF) perpendicular (because they are applied at different times) it is convenient to align the B_2 field along B_1 keeping them both perpendicular to B_0 at all orientations of the crystal. This is achieved by placing eight posts through the resonator perpendicular to the strip alignment and, hence, perpendicular to the microwave electric field. Each post consists of two wires which are connected in such a way that they form an eightturn Helmholtz-like RF-coil. The posts are situated at some distance from the strip at a point where the microwave electric field is at a minimum. The Helmholz-like arrangement ensures a homogeneous B_2 field at the location of the crystal. In Figure 3 the electric E_1 and magnetic fields (B_1 and B_2) in the resonator are scematically indicated.

Figure 2 shows an outline of the X-band ESE-ENDOR resonator insert as used on our department. The resonator and the part connecting it to the input and output wave-guides are made from brass using spark-erosion techniques. The half-λ copper strip is contained in a perspex support. The RF-posts consist of a .2 mm copper wire wound twice through holes of 1 mm in the resonator wall (see fig. 1). In order to minimize heat-leakage the waveguides as well as the rotor drive-bar are made from thin-walled stainless steel. Apart from the sample-rotation port, the insert-flange containes a multipin electrical feed-through in order to enable RF-irradiation of the sample and to measure the temperature directly at the resonator wall. For the latter purpose a callibrated carbon resistor is used for the low temperature range and a Pt-100 resistor for the range 20K-300K.

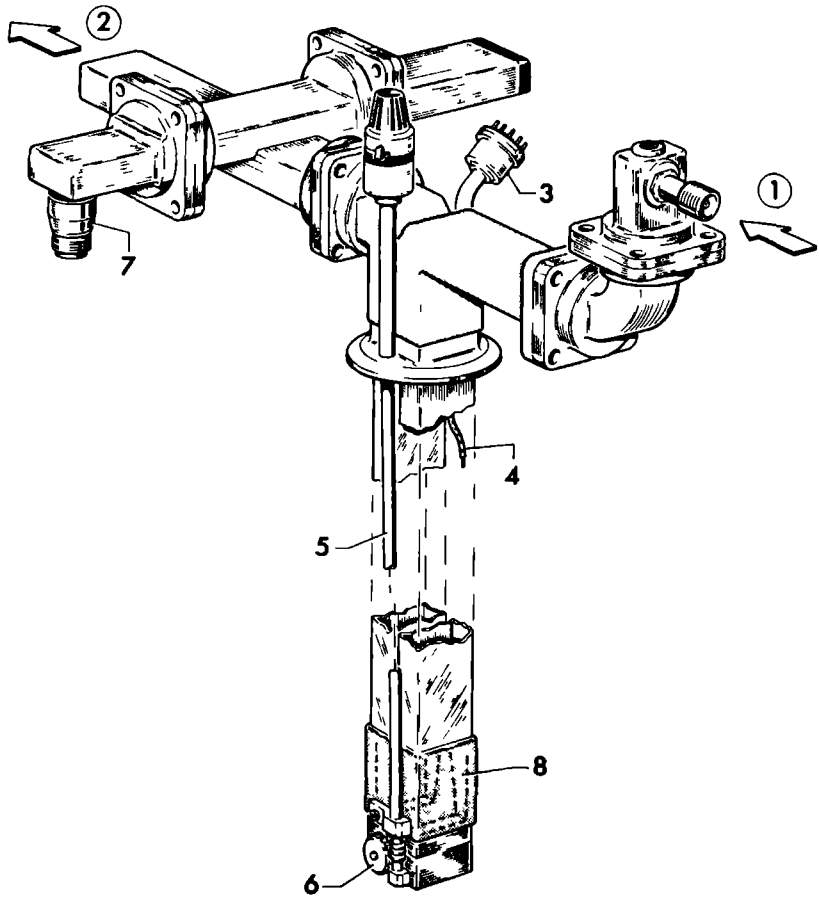

Figure 2 ESE-ENDOR resonator assembly· 1) microwaves in (excitation), 2) microwaves out (echo detection), 3) multipin electrical feedthrough, 4) ENDOR RF-coaxial line, 5) sample rotation drive, 6) sample holder and rotor, 7) -20dB crossguide coupler for monitoring the microwave pulses, 8) waveguide tapering section

III.3 Results

The ESE-ENDOR configuration was tested with the ESE-ENDOR spectrometer which has been described recently (6,7). ^{14}N ESE-ENDOR spectra were measured of 1% doped Cu(II)/Ni(II) bis(N,N-di-ethyl-dithiocarbamate) and tetra-butyl-ammonium Cu(II)/Ni(II) bis(cis 1,2-dicyanoethene-dithiolate) For both complexes the ^{14}N ESEEM as well as the ^{13}C and ^{1}H CW-ENDOR spectra were measured previously (6,8-10). In addition for the dithiocarbamate complex also the ^{14}N CW-ENDOR spectra are known (11,12).

Single crystals of these complexes (size 0.8*2*2 mm^3) were oriented with the magnetic field either parallel or perpendicular to the molecular plane. All experiments were carried out at a temperature of 15K using the stimulated (3-pulse) echo sequence. Microwave pulses of 20 ns and an RF-pulse of 200 μs were used; the timespace between the first and the second microwave pulse was set at the optimum value of 500 ns. The microwave power was about 1 kW whereas for the RF-power approximately 100 W was needed for optimum ENDOR response. In the frequency range from 10 to 15 MHz proton ENDOR effects (reduction of the stimulated echo) of 70% were observed for both complexes. Figure 4 shows some typical ^{14}N ESE-ENDOR spectra recorded in the low frequency range (1-5 MHz) with the B_0 field oriented in the molecular plane. All spectra were recorded with one RF sweep from 1 to 5 MHz in 180 s. The ENDOR linewidth was about 5 kHz for both complexes, which is compar-

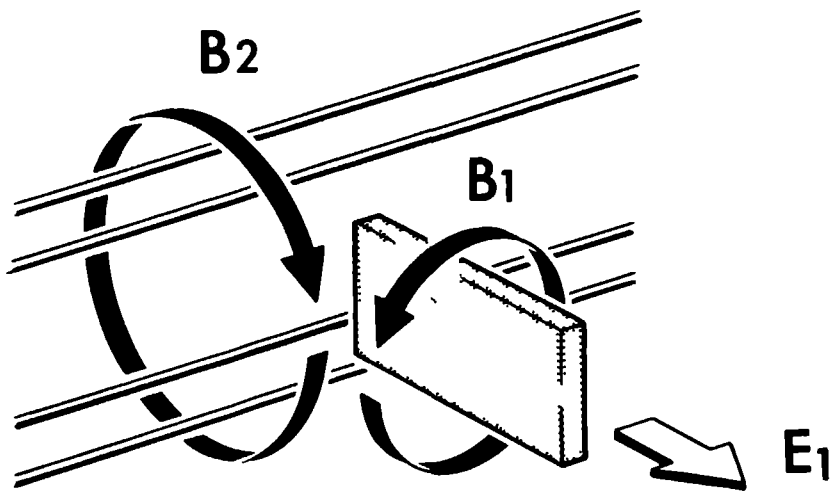

Figure 3 Perspective view of the resonating strip and part of the ENDOR RF-coil The electric (E) and magnetic fields (B_1 and B_2) are schematically indicated For clarity reasons only four of the eight ENDOR posts are shown

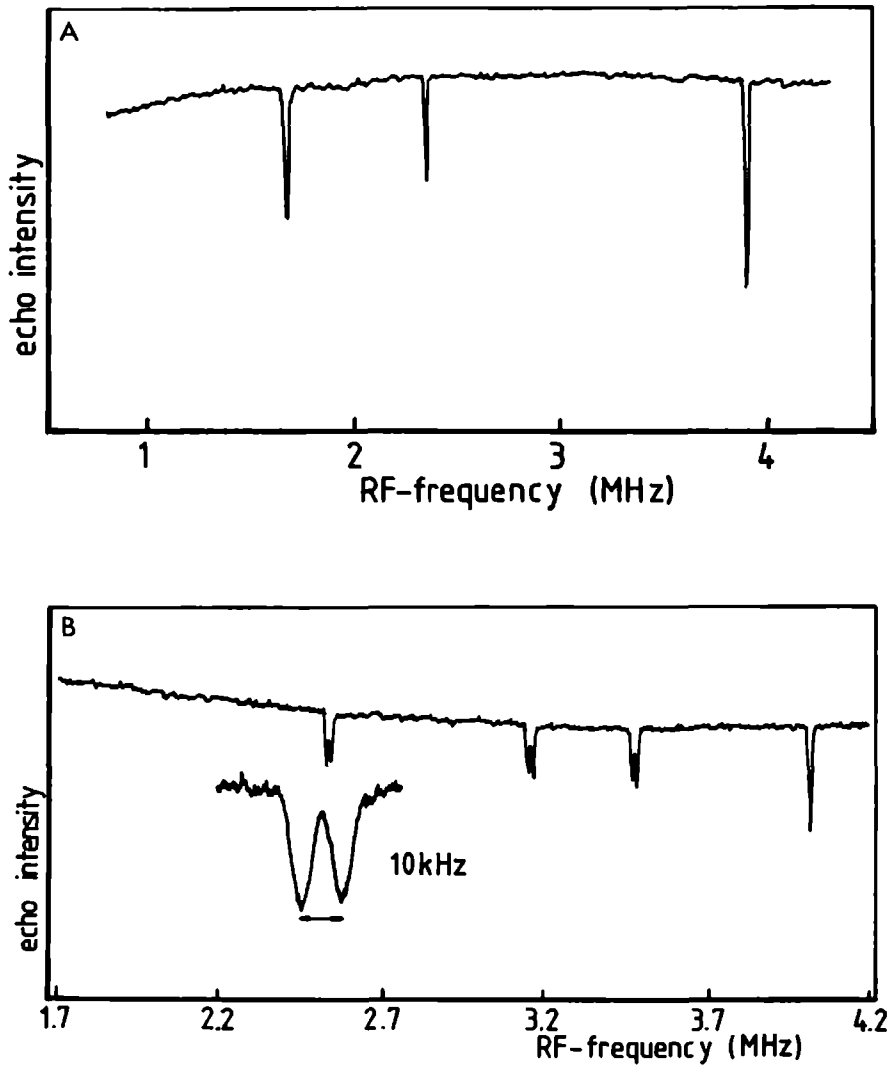

Figure 4 ^{14}N ESE-ENDOR spectra of Cu(II)/Ni(II) bis (N,N di-ethyl- dithiocarbamate) (a) and Cu(II)/Ni(II) bis(cis 1,2-dicyanoethene-dithiolate) (b) The Magnetic field was oriented in the molecular plane Experimental data MW-power 1 kW, RF-power 100 W, 3-pulse echo sequence with τ= 500ns, RF-pulselength = 200 μs, MW-pulselength = 20 ns

able to the 5-7 kHz linewidth observed in the ^{14}N CW-ENDOR spectra of the dithiocarbamate complex (12). ENDOR effects of 10% were observed for most lines whereas for the $\Delta m_I=2$ transitions ENDOR effects of 20% could be reached.

III.4 Conclusions

The ENDOR arrangement in the stripline resonator described above enables single crystal studies with full-rotational freedom in a large temperature range. The ESE-ENDOR response is very good at proton frequencies and satisfactory at ^{14}N frequencies. The frequency resolution is excellent.

Acknowledgments

The authors thank Dr. C.P. Keijzers and Prof. E. de Boer for critically reading the manuscript. This work is financially supported by the Netherlands Foundation for Chemical Research (SON).

References

1. C. Back, M. Mehring, H. Seidel, and H. Weber, Bull. Magn. Res. *2*, 421 (1981)
2. M. Mehring and F. Freysoldt, J. Phys. E. Sci. Instrum. *12*, 894 (1980)
3. W.B. Mims, Rev. Sci. Instrum. *45*, 1583 (1974)
4. J.L. Davis and W.B. Mims, Rev. Sci. Instrum. *49*, 1095 (1978)
5. C. Hutchinson, private communication
6. E.J. Reijerse, M.L.H. Paulissen, and C.P. Keijzers, J. Magn. Reson. *60*, 66 (1984)
7. E.J. Reijerse, N.A.J.M. van Aerle, C.P. Keijzers, R. Böttcher, R, Kirmse and J. Stach, J. Magn. Reson. *67*, 114 (1986).
8. R. Kirmse, J. Stach, U. Abram, W. Dietzch, R. Böttcher, M.C.M. Gribnau, and C.P. Keijzers, Inorg. Chem. *23*, 3333 (1984)

9. D. Snaathorst, C.P. Keijzers, A.A.K. Klaassen, E. de Boer, V.P. Chacko, and R. Gomperts, Mol. Phys. *40*, 585 (1980)

10. E.J. Reijerse, A.H. Thiers, R. Kanters, M.C.M. Gribnau and C.P. Keijzers, J. Chem. Phys. submitted.

11. R. Kirmse, U. Abram, and R. Böttcher Chem. Phys. Lett. *90*, 9 (1982)

12. W. Möhl and E. de Boer, J. Phys. E. Sci. Instrum. *18*, 479 (1985)

CHAPTER IV

Spectral Simulations

IV.1 Magres, a General Spin hamiltonian Program.

Already in the early stages of the EPR work in the department of Molecular Spectroscopy one felt the necessity to calculate and simulate the spectra of complicated paramagnetic spin systems. This resulted finally in the computer program MAGRES that was developed over the years and was applied to calculate single crystal spectra of paramagnetic systems with non-coinciding interaction tensors (1,2). The program is able to work with any number of spin particles (electrons and nuclei) with any spin quantum number. Apart from the Zeeman interaction, a particle is allowed to have an interaction with any other particle (hyperfine, exchange, J-coupling) including itself (quadrupole- and zero-field interaction). These interactions may be specified as isotropic, symmetric or asymetric tensors in a laboratory frame of axes. Obviously, the quadrupole- and zero-field interactions can only be specified by symmetric traceless tensors. A typical hamiltonian is the following:

$$\mathcal{H}_0 = \mu_b \mathbf{B}\cdot\mathbf{g}\cdot\mathbf{S} + \sum_i \mathbf{S}\cdot\mathbf{A}_i\cdot\mathbf{I}_i + \mathbf{S}\cdot\mathbf{D}\cdot\mathbf{S} + \sum_i \mathbf{I}_i\cdot\mathbf{Q}_i\cdot\mathbf{I}_i - \sum_i \gamma_{N_i}\hbar\mathbf{B}\cdot\mathbf{I}_i \qquad [1]$$

The hamiltonian matrix H_0 is set up in the laboratory frame using spin matrices S_x, S_y and S_z and I_x, I_y and I_z and direct product techniques. To save computing time when calculating a series of spectra with different magnetic field orientations, the field independent part H_z and the field dependent part H_{B_0} of the hamiltonian (for a field strength unity) are calculated and stored separately. For each magnetic field direction the field dependent hamiltonian is calculated and combined with the field independent part. The resulting hamiltonian matrix $H_0 = H_z + B \times H_{B_0}$ is diagonalized:

$$E = C^{\dagger} H_0 C \qquad [2]$$

yielding the diagonal eigenvalue matrix E and the eigenfunction matrix C. If transition probabilities are needed the matrix H_{B_1} of the the perturbation hamiltonian is set up on the same basis-functions as used for H_{B_0} and thereafter transformed into the H_0 representation:

$$C^{\dagger} H_{B_1} C = T \qquad [3]$$

yielding the transition moment matrix T. This "two-index" transformation is

optimized for a sparse H_{B_1}-matrix by avoiding multiplication by zero elements of H_{B_1} and by selecting the transitions in the spectral range of interest. The obtained set of transition positions and intensities can be plotted with a standard lineshape function (Lorentzian, Gaussian, absorption or derivative) of variable width. The program is written as a subroutine that can be called by a minimization program. The error function to be minimized is

$$\varepsilon = \sum_n |\nu_n^{exp} - \nu_n^{calc}|^2 \qquad [4]$$

where ν^{exp} and ν^{calc} are the experimental and calculated spectral positions, respectively. The minimization program may have as its minimizing arguments: the tensor elements (or the tensor orientations and the principle values), and the directions of the intersection lines of the planes in which the experiments were carried out. With the latter variation possibility, the effect of the experimental error made in the orientation of the crystal may be reduced (for an application of this feature see (1)).

Recently the program has been adapted for the simulation of powder spectra (3). To this end, a spiral of orientations over half a unit-sphere is taken as the set of magnetic field orientations for which the spectra are "integrated". Typically 1000 - 10000 orientations are needed for a more or less smooth powder spectrum.

In the course of the current project on ESEEM spectroscopy, the program MAGRES has been extended to calculate ESEEM and ENDOR spectra related to a user specified EPR excitation range. These applications will be discussed in sections 3 and 4. First we will discuss some computational details and some possible optimizations of the program that are useful in the subsequent discussion of special techniques (ESEEM and ENDOR).

IV.2 Methods of reducing the computing time

The program in its current form uses the brute force method by calculating the complete spin hamiltonian matrix with all eigenvalues and eigenfunctions. Although this takes considerable computing time, the method works excellent for most single crystal applications, the advantage being that the program can be applied to any (orbitally non-degenerate) spin system. There are several reasons, however, to speed up the calculation of single crystal and powder spectra with the restriction that the general applicability of the program is maintained:

1) The time limiting steps in the spectral simulations are the diagonalization of the spin hamiltonian matrix [2] and the similarity transformation [3] to obtain the transition moments. These steps have a complexity of, respectively, the second and the third power of the total spin multiplicity, N, of the system. The necessary computer memory increases with N^2. Adding spin particles to the hamiltonian increases the total spin multiplicity very rapidly. Therefore, ligand systems with many interacting nuclei will not be accessible to the program in this form.

2) ESEEM simulations use algorithms with even a higher complexity (N^4). Especially ESEEM powder simulations are, therefore, limited to small systems. The majority of the interesting systems, however, involves hyperfine couplings with several (ligand) nuclei which leads to a large total spin multiplicity.

3) Many interesting materials are only available in powder form. The EPR and related spectra of these compounds are difficult to analyse since peak assignment is almost impossible. Therefore, an important application of the simulation program would be the fitting of powder spectra. Since many iterations are needed to optimize such a fit, the calculation of the individual powder spectra must be as efficient as possible.

IV.2.1 Reduction of the spinmultiplicity

Since the dimensionality of the spin system is the most important factor that influences the computing time, it would be very worthwhile to reduce the multiplicity of the problem in a justified way. In the case of a paramagnetic centre interacting with several (ligand) nuclei via small hyperfine interactions a "legal" way of reducing the multiplicity without being unacceptably inaccurate, is to partition the hamiltonian into sub-hamiltonians: All "strong" interactions are contained in a so called "core" hamiltonian, e.g.

$$\mathcal{H}_0^C = \mu_b \mathbf{B}\cdot\mathbf{g}\cdot\mathbf{S} + \mathbf{S}\cdot\mathbf{A}^{Cu}\cdot\mathbf{I}^{Cu} + \mathbf{I}^{Cu}\cdot\mathbf{Q}^{Cu}\cdot\mathbf{I}^{Cu} - \gamma_N\hbar\mathbf{B}\cdot\mathbf{I}^{Cu} \qquad [5]$$

for an electron in a copper complex. The nuclei with small couplings to the paramagnetic centre are contained in separate sub-hamiltonians:

$$\mathcal{H}_0^L = \mathbf{S}\cdot\mathbf{A}^L\cdot\mathbf{I}^L + \mathbf{I}^L\cdot\mathbf{P}^L\cdot\mathbf{I}^L - \gamma\hbar\mathbf{B}\cdot\mathbf{I}^L \qquad [6]$$

resulting in the total hamiltonian

$$\mathcal{H}_0 = \mathcal{H}_0^C + \sum_L \mathcal{H}_0^L \qquad [7]$$

The essence of this approximation will be that the core hamiltonian eigenstates are supposed not to be influenced by the weak interactions of the other nuclei which are treated as "ligands", i.e. no mixing of core eigenfunctions is allowed. In other words: the ligand hamiltonians are treated in the "effective field" of the core hamiltonian. It is implied, therefore, that there be no degeneracy in the core levels and that the energy separation between the core levels is much larger than that between the ligand levels.

The first step of the procedure is to diagonalize the matrix of the core hamiltonian:

$$C^{\dagger} \cdot H^C \cdot C = E^C \qquad [8]$$

This yields N^C eigenvalues and eigenfunctions. In the case of one ligand L, for each core eigenfunction $\vec{c}_n$, with eigenvalue e_n, a ligand sub hamiltonian matrix is calculated:

$$\vec{c}_n^{\dagger} \otimes U^L \cdot H^L \cdot \vec{c}_n \otimes U^L = H_n^L \qquad [9]$$

where H^L is set up in the full $(N^L \times N^C)$ multiplicity of the total hamiltonian matrix. U^L is the unit matrix of dimension $2I^L+1$. As a result we have H_n^L of dimension $2I^L+1$, defined on the core representation of eigenstate n. In fact, the transformation [9] is merely a "limited" similarity transformation of the ligand hamiltonian to the core representation retaining only the matrix elements belonging to one core eigenfunction. The transformation can be done very efficiently since H^L is a sparse matrix.

A practical implementation of this method is suggested by Mims (3): The ligand hyperfine interaction is factored out in the following way:

$$\mathcal{H}_{SI} = \mathbf{S} \cdot \mathbf{A} \cdot \mathbf{I} = \mathbf{I}_x \sum_i a_{ix} \mathbf{S}_i + \mathbf{I}_y \sum_i a_{iy} \mathbf{S}_i + \mathbf{I}_z \sum_i a_{iz} \mathbf{S}_i \qquad i = x, y, z \qquad [10]$$

The matrices of $\sum_i a_{ij} \mathbf{S}_i$ are calculated in the basis of the core hamiltonian and subsequently transformed to the core representation retaining only diagonal elements.

$$H_{SI} = I_x \otimes \Sigma_x^C + I_y \otimes \Sigma_y^C + I_z \otimes \Sigma_z^C \qquad [11]$$

The diagonal elements of Σ_x^C, Σ_y^C and Σ_z^C are the coefficients to set up the $\mathcal{H}_{SI}$ contributions of the ligand hamiltonian in each core eigenstate, $\vec{c}_n$,

$$H_n^L = \Sigma_x^C(n,n)I_x^L + \Sigma_y^C(n,n)I_y^L + \Sigma_z^C(n,n)I_z^L + \sum_{ij}^{xyz} I_i^L \cdot p_{ij}^L \cdot I_j^L \qquad [12]$$

$$- \gamma\hbar\left\{B_x I_x^L + B_y I_y^L + B_z I_z^L\right\}$$

The resulting sub-hamiltonians H_n^L are now diagonalized separately yielding eigenvectors $l_{n,i}$ and eigenvalues $e_{n,i}^L$ (matrices L_n and E_n^L). The indices n,i indicate ligand level i, associated with core level n. The transition moments between the core levels and between the ligand levels are calculated separately:

$$C^{\dagger}H_1^C C = T^C \text{ with elements } \langle c_n | H_1^C | c_m \rangle \qquad [13]$$

$$L_n^{\dagger}H_1^L L_n = T_n^L \text{ with elements } \langle l_{n,i} | H_1^L | l_{m,j} \rangle$$

where H_1^C and H_1^L are the core- and ligand perturbation hamiltonians, respectively, describing the interaction with the EM-field. The total transition probabilities are easily calculated from these components:

$$P_{n,i\to m,j} = |\langle c_n l_{n,i} | H_1^C + H_1^L | c_m l_{m,j} \rangle|^2 \qquad [14]$$

$$= |\langle c_n | H_1^C | c_m \rangle \langle l_{ni} | l_{mj} \rangle + \delta_{n,m} \langle l_{ni} | H_1^L | l_{mj} \rangle|^2$$

For pure EPR work ($n \neq m$) only the first term has to be calculated, while for pure NMR work only the second term has to be retained, thus leading to a significant simplification of the calculating procedure. For ESEEM as a pure EPR technique, this method is particularly useful. In fact, as will be discussed in section 3, the ESEEM modulation relations are derived using the same formalism of sub-hamiltonians. For ENDOR as a double resonance technique, in principle both terms in [14] have to be calculated.

This procedure of subdivision of the problem opens possibilities for major shortcuts in the calculating process since, depending on the type of the experiment, parts of the calculation can be skipped. The implementation in MAGRES can be arranged such that the user has a free choice of grouping particles and interactions into the core-, and one or more sub-hamiltonians. If no interaction between particles in different ligand sub-hamiltonians is allowed, each ligand can be treated separately.

IV.2.2 Powder calculations: interpolating single crystal spectra

A significant problem in the calculation of powder spectra is the "noise" caused by the limited number of single crystal spectra in the integration. It would be worthwhile to compute spectra at intermediate orientations to fill up the gaps, without actually calculating them but, by deriving them from spectra that were calculated for nearby field orientations. One very simple and efficient way of doing this is to make use of first order perturbation theory. To this end the field dependent part of the hamiltonian, $\mathcal{H}_{B_0}$, is rewritten as:

$$\mathcal{H}_{B_0} = B_x^0 \sum_k \sum_i g_{xi}^k \mathbf{S}_i^k \mu_k + B_y^0 \sum_k \sum_i g_{yi}^k \mathbf{S}_i^k \mu_k + B_z^0 \sum_k \sum_i g_{zi}^k \mathbf{S}_i^k \mu_k \qquad [15]$$

$$= B_x^0 \mathbf{F}_x + B_y^0 \mathbf{F}_y + B_z^0 \mathbf{F}_z$$

$$= \vec{B}_0 \cdot \vec{\mathbf{F}}$$

where i=x,y,z and k runs over the particles in the spin system. The total hamiltonian can be written as

$$\mathcal{H}_0 = \mathcal{H}_z + \vec{B}_0 \cdot \vec{\mathbf{F}} \qquad [16]$$

where $\mathbf{H}_z$ is the field independent part. Suppose a single crystal spectrum is calculated for field $\vec{B}_0$ and we wish to calculate the spectrum at a slightly different magnetic field $\vec{B}$. The perturbed hamiltonian is now defined as

$$\mathcal{H} = \mathcal{H}_0 + \vec{d} \cdot \vec{\mathbf{F}} \qquad [17]$$

where $\vec{d} = \vec{B} - \vec{B}_0$. The eigenvalue problem can now be written as

$$(H_0 + \vec{d} \cdot \vec{F}) C = EC \qquad [18]$$

where $C = (C^0 + \vec{d} \cdot \vec{C}^1 + \ldots)$ and $E = (E^0 + \vec{d} \cdot \vec{E}^1 + \ldots)$. The terms linear in $\vec{d}$ yield the first order equations:

$$(H_0 C_\gamma^1 + F_\gamma C^0) = (C^0 E_\gamma^1 + C_\gamma^1 E^0) \qquad [19]$$

with $\gamma = x, y, z$. Making use of the orthogonality of C^0, the fact that H_0 is hermitian and the fact that E^0 is diagonal, we obtain:

$$E_\gamma^1 = C^{0\dagger} F_\gamma C^0 \qquad \gamma = x,y,z \qquad [20]$$

In the matrices E_γ^1 only the diagonal elements are retained thus yielding the first order dependencies of the eigenvalues on the x,y and z components of the magnetic field. These can be used to calculate the shift in spectral positions as a result of a small change $\vec{d}$ in magnetic field. An analogous calculation of the corrections for the spectral intensities is not feasible, since this would involve a first order perturbation treatment of the eigenfunctions, which has about the same complexity as an entire new calculation. It can easily be shown, however, that a first order perturbation treatment of the transition probabilities will never reveal any transitions that are completely forbidden in zero order. When P is the transition matrix in the H_0 representation, the first order corrected one is given by $P^0+\vec{d}\cdot\vec{P}^1$. As a consequence, the transition probability P_{nm} can be written as

$$(P_{nm})^2 = (P_{nm}^0)^2 + 2\vec{d}\cdot\vec{P}_{nm}^1 P_{nm}^0 + \textit{higher order terms} \qquad [21]$$

and $P_{nm} = 0$ if $P_{nm}^0 = 0$. Using the above procedure, it is possible to define a very dense grid of orientations over the unit sphere, for which only say 10% of the spectra must be fully calculated. The rest can be interpolated. This would yield an enormous reduction in computing time.

This treatment would also lead to a slight optimization of the individual (exact) single crystal calculations: According to equation [16], the field dependency part of the hamiltonian is calculated from the components F_x, F_y and F_z which need to be calculated only once. Therefore, the conversion of the interaction tensors and spin matrices into a hamitonian matrix of the final multiplicity, has been completely reduced to a preconditioning step for the subsequent calculations of spectra along a series of different magnetic fields.

IV.3 ESEEM calculations.

The calculation of Electron Spin Echo Envelope Modulation intensities for an arbitrary spin system is based on the expressions that have been derived by Mims (3). In order to illustrate the implementation of these relations into MAGRES and to indicate possible extensions of these relations to ESEENDOR, we will briefly review the derivation of these expressions.

The main task in describing a pulsed Magnetic Resonance experiment is to find an expression for the evolution of the density matrix ϱ during the successive radiation pulses (along the x-axis) and free precession intervals. The expectation value of the transverse magnetization M_y can be obtained from the density matrix at any time from the relation

$$<M_y>(t) = Tr(\varrho(t)M_y) \qquad [22]$$

The hamiltonian is defined the same way as in section 2.1 equation [7], i.e. it is divided into a core contribution (e.g. an electron coupled to a Cu-spin) and one or more ligand contributions (e.g. one or more nitrogen spins coupled to the electron spin). The following treatment will be limited to one ligand because, as will be demonstrated, the extension of the final expressions to more ligands is very straightforward. The following hamiltonian is used:

$$\mathcal{H} = \mathcal{H}_0^C + \mathcal{H}_0^L + \mathcal{H}_1(t) \qquad [23]$$

where $\mathcal{H}_0^C$ and $\mathcal{H}_0^L$ are defined in equations [5] and [6]. With MAGRES, the eigenfunctions and eigenvalues of $\mathcal{H}_0^C+\mathcal{H}_0^L$ are calculated exactly, i.e. including all anisotropy. For S = 1/2 and at X-band fields, the eigenvalues can be distinguished into two manifolds, separated by ~ the X-band frequency if hyperfine and other interactions for copper and the ligands have "normal" magnitudes. Although the eigenfunctions are mixtures of m_S = +1/2 and -1/2 (due to anisotropic hyperfine) we will indicate the two manifolds as α and β for simplicity reasons. The time dependent perturbation hamiltonian $\mathcal{H}_1(t)$ is considered to induce only transitions between different "m_S" manifolds. The remaining matrix elements are calculated exactly by MAGRES, taking account of the g-anisotropy. Therefore, we can write the matrix of $\mathcal{H}_1(t) = 2V\cos\omega t$ in the H_0 representation as follows:

$$H_1(t) = \begin{bmatrix} 0 & 2<\phi_i^\alpha|V|\phi_k^\beta>\cos\omega t \\ 2<\phi_n^\beta|V|\phi_j^\alpha>\cos\omega t & 0 \end{bmatrix} \qquad [24a]$$

where ϕ_t are eigenfunctions of $\mathcal{H}_0$. The time dependence can be decomposed into two counter-rotating components, one of which is neglected because it is far off-resonance:

$$H_1(t) = \begin{bmatrix} 0 & <\phi_i^\alpha|V|\phi_k^\beta>e^{-i\omega t} \\ <\phi_n^\beta|V|\phi_j^\alpha>e^{i\omega t} & 0 \end{bmatrix} \qquad [24b]$$

The matrix can be rewritten as:

$$H_1(t) = e^{-i\omega\Sigma_S t}\begin{bmatrix} 0 & V_{ik} \\ V_{jn}^* & 0 \end{bmatrix}e^{i\omega\Sigma_S t} \qquad [24c]$$

where Σ_S is defined as $\frac{1}{2}\begin{bmatrix} U & 0 \\ 0 & -U \end{bmatrix}$ (U is the unit matrix of the dimension of the α and β manifolds). The time dependence can now be removed by the

transformation (to the "rotating frame"):

$$\hat{\mathcal{H}}_1 = e^{i\omega\Sigma_S t}\,\mathcal{H}_1(t)\,e^{-i\omega\Sigma_S t} = V \qquad [25]$$

The transformation [25] is equivalent to transforming the eigenfunctions ϕ_i of $\mathcal{H}_0$ into $e^{\pm i\omega t/2}\phi_i$ (- for the α-manifold and + for the β-manifold); in other words: the time dependence is transferred from the operator $\mathcal{H}_1(t)$ to the eigenfunctions of the stationary Hamiltonian. As a concequence, the full hamiltonian must be transformed with the same transformation. In order that the eigenfunctions of the time dependant Schrödinger equation are invariant, this results in the transformed hamiltonian:

$$\hat{\mathcal{H}}_N = (\mathcal{H}_0^C + \mathcal{H}_0^L) - \hbar\omega\Sigma_S + V \qquad [26a]$$

This is the hamiltonian working during nutation periods of a pulse sequence. For a zero resonance field, i.e. during free precession periods, we can write the hamiltonian as:

$$\hat{\mathcal{H}}_F = (\mathcal{H}_0^C + \mathcal{H}_0^L) - \hbar\omega\Sigma_S \qquad [26b]$$

The time dependence of the density matrix in the rotating frame is expressed as:

$$\frac{d\hat{\varrho}}{dt} = \frac{i}{\hbar}\left[\hat{\varrho},\hat{\mathcal{H}}\right] \qquad [27]$$

The general solution for an arbitrary time interval is given by:

$$\hat{\varrho}(t_2) = e^{-\frac{i}{\hbar}\hat{\mathcal{H}}(t_2-t_1)}\,\hat{\varrho}(t_1)\,e^{\frac{i}{\hbar}\hat{\mathcal{H}}(t_2-t_1)} \qquad [28]$$

Neglecting the time period of the microwave pulses, the time evolution during a three-pulse ESE experiment can now be written as:

$$\hat{\varrho}(2\tau+T+t) = R^{\dagger}(2\tau+T+t)\,\hat{\varrho}(0)\,R(2\tau+T+t) \qquad [29]$$

where $R(t) = e^{i/\hbar\mathcal{H}t}$. The rotation operator, R, is composed of the subsequent nutation and free precession operators:

$$R(2\tau+T+t) = R_N R_F(\tau) R_N R_F(T) R_N R_F(\tau+t) \qquad [30]$$

The rotation matrices $R_F(t) = e^{i/\hbar\mathcal{H}_F(t)}$ which account for the free precession intervals are easy to calculate since H_F in the H_0 representation is completely diagonal. Therefore, $R_F(\tau)$ will be diagonal as well:

$$R_F^{\alpha}(i)(\tau) = e^{\imath(\omega_i^{\alpha} - \frac{1}{2}\omega)\tau} \quad ; \quad R_F^{\beta}(k)(\tau) = e^{\imath(\omega_k^{\beta} + \frac{1}{2}\omega)\tau} \qquad [31]$$

ω_i^{α} and ω_k^{β} are the eigenvalues in the α and β "m_S" manifolds, repectively, expressed in frequency units.

The nutation matrices $R_N(t_p) = e^{\frac{\imath}{\hbar}\mathcal{H}_N t_p}$ are somewhat more involved to calculate. The common procedure is first to diagonalize the nutation hamiltonian which is defined in [26a] :

$$V_N^{\dagger}\, \hat{H}_N\, V_N = \Lambda_N \qquad [32]$$

subsequently calculating the exponential nutation operator in this representation: $e^{\imath/\hbar\Lambda_n t_p}$ and then transforming back to the H_0 representation:

$$R_N = V_N\, e^{\frac{\imath}{\hbar}\Lambda_N t_p}\, V_N^{\dagger} \qquad [33]$$

Where t_p is the pulse duration (negligibly short as compared to the precessing time intervals). Let's consider the effect of this procedure on an EPR transition element connecting two core eigenstates α_i and β_j using a standard two level treatment:

$$\hat{H}_N\{\alpha_i,\beta_n\} = \begin{bmatrix} E_i^{\alpha} - \frac{1}{2}\hbar\omega & \langle\phi_i^{\alpha}|V|\phi_n^{\beta}\rangle \\ \langle\phi_n^{\beta}|V|\phi_i^{\alpha}\rangle & E_n^{\beta} + \frac{1}{2}\hbar\omega \end{bmatrix} \qquad [34]$$

in a simplified notation:

$$\begin{bmatrix} c & 0 \\ 0 & c \end{bmatrix} + \begin{bmatrix} a & b \\ b^{*} & -a \end{bmatrix} \qquad [35]$$

Where

$$a = \tfrac{1}{2}(E_i^{\alpha} - E_n^{\beta} - \hbar\omega),\ c = \tfrac{1}{2}(E_i^{\alpha} + E_n^{\beta})$$

and

$$b = \langle\phi_i^{\alpha}|V|\phi_n^{\beta}\rangle = |b|e^{\imath\phi_b}$$

Defining

$$\sin 2\eta = \frac{|b|}{(a^2 + bb^{*})^{\frac{1}{2}}} \quad \text{and} \quad \cos 2\eta = \frac{a}{(a^2 + bb^{*})^{\frac{1}{2}}} \qquad [36]$$

we obtain eigenvalues $\varepsilon_{1,2} = c \pm p$ $(p = (a^2 + bb^{*})^{\frac{1}{2}})$ with column eigenvectors

$$V_N = \begin{bmatrix} \cos\eta & -sin\eta\, e^{i\Phi_b} \\ \sin\eta\, e^{-i\Phi_b} & \cos\eta \end{bmatrix} \qquad [37]$$

The angle η is a measure of the mixing between the connected levels. When the radiation frequency is at resonance, the levels are degenerate in the rotating frame and the mixing is at a maximum (a=0; $\eta = \pi/4$). After transforming back to the H_0 representation, the corresponding part of R_N looks like:

$$e^{i\omega_c t_p} \begin{bmatrix} \cos^2\eta\, e^{i\omega_p t_p} + \sin^2\eta\, e^{-i\omega_p t_p} & 2isin\eta\cos\eta\, e^{i\Phi_b} sin(\omega_p t_p) \\ 2isin\eta\cos\eta\, e^{-i\Phi_b} sin(\omega_p t_p) & \cos^2\eta\, e^{-i\omega_p t_p} + \sin^2\eta\, e^{i\omega_p t_p} \end{bmatrix} \qquad [38]$$

Where $\omega_c = c/\hbar$ and $\omega_p = p/\hbar$. In the case of on-resonance excitation ($\eta = \pi/4$), the nutation part reduces to:

$$e^{i\omega_c t_p} \begin{bmatrix} \cos\omega_p t_p & ie^{i\Phi_b}\sin\omega_p t_p \\ ie^{-i\Phi_b}\sin\omega_p t_p & \cos\omega_p t_p \end{bmatrix} \qquad [39]$$

while for completely off-resonance excitation (a>>b) the off-diagonal elements disappear. In this case the nutation operator reduces to a free-precession operator:

$$e^{i\omega_c t_p} \begin{bmatrix} e^{-i\omega_p t_p} & 0 \\ 0 & e^{+i\omega_p t_p} \end{bmatrix} \qquad [40]$$

The microwave pulses used in an ESEEM experiment usually excite only one core EPR transition, i.e only one EPR transition is at resonance, while the others are completely off-resonance. For the description of an ESEEM experiment it is, therefore, sufficient to treat the core part as a two-level system. In the case of short, intense microwave pulses, however, the ligand levels associated with these two core levels are connected completely at resonance. This is the reason why in [23] H_0 was divided into a "core" and a "ligand" part. For the calculation of the eigenvalues there is no distinction between core and ligand. For the derivation of the modulations due to the ligand, however, we assume that all ligand levels belonging to one core-level are at the same time in resonance, i.e. the spread due to the ligand interactions is much smaller than the pulsewidth. In that case the nutation matrix can be written in the complete H_0 representation as:

$$e^{i\omega_c t_p} \begin{bmatrix} U\cos\omega_p t_p & iM\sin\omega_p t_p e^{i\Phi_b} \\ iM^{\dagger}e^{-i\Phi_b}\sin\omega_p t_p & U\cos\omega_p t_p \end{bmatrix} \qquad [41]$$

Where U is the unit matrix, and M is the "ligand overlap" matrix defined as $M = \langle L^{\alpha\dagger} | L^{\beta} \rangle$ (see [13,14]). Both matrices have dimension N^L. Also the free precession operators can be represented in terms of submatrices:

$$R_F(\tau) = \begin{bmatrix} R_\tau^\alpha & 0 \\ 0 & R_\tau^\beta \end{bmatrix} \quad ; \quad R_\tau^\alpha(i,i) = e^{\frac{i}{\hbar}H_F\tau} = e^{i(\omega_i^\alpha - \frac{1}{2}\omega)\tau} \qquad [42]$$

It has been shown by Mims (3) that equation [29] can be multiplied manually using this sub-hamiltonian treatment retaining only terms for which phase cancellation takes place at the time of the echo, resulting in:

$$\langle M_y \rangle (2\tau+T) = \frac{1}{2(2I+1)} \mathrm{Re} \Big[Tr(R_\xi^{\beta\dagger} M^\dagger R_\tau^{\alpha\dagger} R_\phi^{\alpha\dagger} M R_\xi^\beta M^\dagger R_\tau^\alpha R_\phi^\alpha M)$$

$$+ \; Tr(R_\xi^{\beta\dagger} R_\phi^{\beta\dagger} M^\dagger R_\tau^{\alpha\dagger} M R_\xi^\beta R_\phi^\beta M^\dagger R_\tau^\alpha M) \Big] \qquad [43]$$

The free precession operator products of the form $R_\tau R_T$ can be replaced by $R_{\tau+T}$. The two modulation terms are now equivalent under interchange of τ and $\tau+T$. Therefore, defining $\tau' = \tau+T$, we can write:

$$\langle M_y \rangle (2\tau+T) = \frac{1}{2}[V(\tau',\tau) + V(\tau,\tau')] \qquad [44]$$

where $V(\tau',\tau)$ is expressed as:

$$V(\tau',\tau) = \frac{1}{2(2I+1)} \left\{ Tr(R_{\tau'}^{\beta\dagger} M^\dagger R_{\tau'}^{\alpha\dagger} M R_\tau^\beta M^\dagger R_\tau^\alpha M) + CC \right\} \qquad [45]$$

$$= \frac{1}{2(2I+1)} \left\{ \sum_{ijkn} e^{i(\omega_i^\alpha - \omega_j^\alpha)\tau'} e^{i(\omega_k^\beta - \omega_n^\beta)\tau} M_{jn}^* M_{jk} M_{ik}^* M_{in} + CC \right\}$$

Indices i,j and k,n run over the α and β M_s manifolds respectively. Expression [45] can be simplified further by combining with the complex conjugate:

$$V(\tau',\tau) = \chi_o + \tfrac{1}{2}\sum_{i>j} \chi_{ij} \cos\omega_{ij}^\alpha \tau' \qquad [46]$$

$$+ \tfrac{1}{2}\sum_{k>n} \chi_{kn} \cos\omega_{kn}^\beta \tau$$

$$+ \sum_{i>j,k>n} \chi_{ij,kn} \cos\omega_{ij}^{\alpha}\tau' \cos\omega_{kn}^{\beta}\tau$$

where the modulation coefficients are defined as follows:

$$\chi_o = \frac{1}{2I+1} \sum_{i,k} |M_{ik}|^4 \qquad [47]$$

$$\chi_{ij} = \frac{2}{2I+1} \sum_{k} |M_{ik}|^2 |M_{jk}|^2$$

$$\chi_{kn} = \frac{2}{2I+1} \sum_{i} |M_{ik}|^2 |M_{in}|^2$$

$$\chi_{ij,kn} = \frac{2}{2I+1} Re[M_{jn}^{*} M_{jk} M_{ik}^{*} M_{in}]$$

From these expressions, the modulation intensities of a three pulse ESEEM experiment as a function of τ or τ' (both experiments are identical in this case) can be calculated directly from the transition moments M_{ik} and ENDOR frequencies ω_{ij}^{α} and ω_{kn}^{β} and the fixed time parameter (τ' or τ).

$$P_{kn}^{\beta} = \frac{1}{2} \left\{ \tfrac{1}{2}\chi_{kn} + \sum_{i>j} \chi_{ij,kn} \cos\omega_{ij}^{\alpha}\tau \right\} \qquad [48]$$

$$P_{ij}^{\alpha} = \frac{1}{2} \left\{ \tfrac{1}{2}\chi_{ij} + \sum_{k>n} \chi_{ij,kn} \cos\omega_{kn}^{\beta}\tau \right\}$$

The second term represents the so called "suppression effect" causing modulation of the intensity as a function of τ with frequencies of the opposite m_S manifold. E.g when $\chi_{ij,kn} = -\tfrac{1}{2}\chi_{ij}$ (as is the case for spin I=1/2), frequency ω_{ij} is completely suppressed when τ is chosen an integer times $2\pi/\omega_{kn}$.

For the two-pulse ESEEM experiment a similar expression can be derived. It is easily inferred from the three-pulse result by putting $\tau = \tau'$ i.e. T=0:

$$\langle M_y \rangle_{2\tau} = \frac{1}{2(2I+1)} \{ Tr(R_{\tau}^{\beta\dagger} M^{\dagger} R_{\tau}^{\alpha\dagger} M R_{\tau}^{\beta} M^{\dagger} R_{\tau}^{\alpha} M) + CC \} \qquad [49]$$

$$= \frac{1}{2(2I+1)} \{ \sum_{ijkn} e^{i\omega_{ij}^{\alpha}\tau} e^{i\omega_{kn}^{\beta}\tau} M_{jn}^{*} M_{jk} M_{ik}^{*} M_{in} + CC \}$$

$$= \chi_o + \sum_{i>j} \chi_{ij} \cos\omega_{ij}^{\alpha}\tau + \sum_{k>n} \chi_{kn} \cos\omega_{kn}^{\beta}\tau$$

$$+ \sum_{i>j,k>n} \chi_{ij,kn} \{ \cos(\omega_{ij}^{\alpha} + \omega_{kn}^{\beta})\tau + \cos(\omega_{ij}^{\alpha} - \omega_{kn}^{\beta})\tau \}$$

with the same basic intensities χ_{ij} and χ_{kn}. The terms $\chi_{ij,kn}$ which in the three-pulse experiment were involved in the suppression effect, are now producing sums and differences of ENDOR frequencies belonging to opposite m_s manifolds.

It is easy to show, in fact, that in a two-dimensional three-pulse experiment (i.e. recording the stimulated echo as a function of both τ and τ') cross peaks of intensity $\chi_{ij,kn}$ occur at positions $(\omega_{ij},\omega_{kn})$ in the two-dimensional frequency spectrum, correlating frequencies of different m_s manifold to each other. This feature can be used to assign peaks in complicated ESEEM spectra as is nicely demonstrated by Merks et al. (4) and Barkhuysen et al. (5).

Relations [48] and [49] are the actual expressions implemented in MAGRES. The first step is to calculate the basic modulation intensities χ_{ij} and χ_{kn}. To save computing time in calculating three-pulse modulation spectra, the suppression term in [48] may be omitted thus giving rise to a "suppression free" spectrum. The experimental analogue would be a two-dimensional ESEEM spectrum integrated over one dimension. The suppression term in [48] is so to say integrated over al possible values of τ leading to the average of zero. Since the sub-hamiltonian approximation is not yet implemented in MAGRES, instead of the ligand overlap matrix M, the full transition moment matrix T is used (see eq [3]). The transition moments are weighed with the lineshape function associated with the excitation area:

$$T_{ik}' = T_{ik}\ G(\omega_o - \omega_{ik}) \qquad [50]$$

where ω_o is the microwave excitation frequency. This feature opens the possibility of calculating powder ESEEM spectra of systems with an anisotropic core-hamiltonian (e.g. a Copper complex with anisotropic g and A-tensor such as the one studied in Chapter VI).

The extension of the modulation expressions to the case of more than one interacting ligand, is quite straightforward since in our sub-hamiltonian approximation the ligands are treated completely independently from each other. Therefore, the resulting submatrices of the α and β manifold are merely direct product expansions between the individual ligand submatrices:

$$M^{L_1L_2} = M^{L_1} \otimes M^{L_2} \qquad [51]$$

$$R_N^{\alpha L_1 L_2} = R_N^{\alpha L_1} \otimes R_N^{\alpha L_2}$$

Using the theorem $Tr(A \otimes B) = TrA \times TrB$, the traces in equation [45] and [49] can be factored out into the contributions of the individual ligands. The final expression for the two- and three pulse ESEEM experiment on multi ligand systems are quite compact:

$$<M_y>_{stim}(2\tau+T) = \prod_k N_k V^k(\tau,\tau') + \prod_k N_k V^k(\tau',\tau) \qquad [52]$$

$$<M_y>_{2p}(2\tau) = \prod_k N_k V^k(\tau,\tau)$$

where N_k is some appropriate normalization constant. Note that in the three-pulse case only combinations can occur between frequencies of different ligands but belonging to the same m_s manifold, while in the two-pulse case all combination frequencies may be generated. A very efficient way of implementing these expressions would be to calculate for every ligand sub-hamiltonian the frequency domain spectrum; subsequently transforming them to the time-domain via an inverse Fast Fourier Transformation; then multiplying all ligand time-domain spectra and finally, if one would be interested in the frequency spectrum, a forward Fast Fourier Transformation. Moreover, it can be shown that when the modulation intensities are small it is sufficient to add the individual frequency domain spectra directly. In this case the calculations are particularly simple. Following the above procedure, and the optimization strategies sketched in section 2, the fitting of powder ESEEM spectra would become feasable.

IV.4 ENDOR calculations

The CW-ENDOR technique is a well known alternative for ESEEM spectroscopy. As will be discussed in Chaper VII, the two techniques yield complementary information since the spectral intensities are bases on different types of transitions. The ESEEM intensities are governed by the EPR transition moments, while the ENDOR intensities in principle depend on both EPR and NMR transition probabilities (mainly on NMR). In MAGRES the ENDOR spectral intensities are calculated as follows:

$$P_{ij} = T_{ij}(\sum_k T_{ik} G(\omega_o - \omega_{ik})) \times (\sum_k T_{jk} G(\omega_o - \omega_{jk})) \times B(i,j) \qquad [53]$$

where

$$B(i,j) = \frac{e^{-E_i/kT} - e^{-E_j/kT}}{\sum_k e^{-E_k/kT}}$$

$G(\omega)$ is the excitation lineshape around the carrier frequency of the microwave pulses (ω_0). T_{ij} are the transition moments between states i and j. B(i,j) is the Boltzmann equilibrium correction factor. The levels are so to say weighed with the transition moments of the associated EPR transitions near the pumping frequency. Therefore, levels that are not excited by the microwave radiation are skipped in the calculation. The experimental CW-ENDOR intensities do not only reflect the NMR transition moments, but also depend on the balance of cross-relaxation times involved in a CW-experiment. Moreover, instrumental effects such as the impedance match of the RF-coil may cause deviations of the experimental intensities from the NMR intensities. Unlike ESEEM, the ENDOR simulations will thus only give a qualitative picture of the experimental spectrum. It is, therefore, not feasible to try to fit ENDOR powder spectra.

The third technique that was employed in the course of our project was ESE-ENDOR, the pulsed variant of CW-ENDOR. As was discussed in Chapter I, the RF irradiation takes place during waiting time T of a stimulated echo sequence. Instead of a desaturation effect like in CW-ENDOR, the ENDOR effect is based on the phase destruction of EPR spin packets during the 3-pulse experiment, thus leading to a reduction of the echo. Apart from the NMR transitions, also the EPR transition moments and the phase coherence between them should be included in an ESE-ENDOR simulation. To our knowledge, no closed form relations are reported for this type of experiment. Obviously, the starting point of such a calculation would be the evaluation of the traces in [43] where the free precession operator R_T is replaced by an RF-nutation matrix. Liao and Hartmann (6) derived an expression following this procedure, however, under a set of limiting conditions: a very short RF pulse relative to the waiting time T and no modulation effect (i.e. putting the ligand overlap matrix M in [43] equal to the unit matrix U). When e.g. transition f,g in the α or β manifold is "hit", the expression of Liao and Hartmann can be written as:

$$\langle M_y \rangle_{stim} = \frac{1}{4}(1 + \frac{1}{2I+1}\{2I - 1 + 2cos^2\tfrac{1}{2}\theta + 2\sin^2\tfrac{1}{2}\theta\cos[\omega_{fg}^{\alpha} - \omega_{fg}^{\beta}]\tau\}) \qquad [54]$$

where θ is the RF-pulse angle. This expression indicates a modulation of the

ENDOR effect as a function of τ with the (isotropic) hyperfine frequency $(\omega_{fg}^{\alpha}-\omega_{fg}^{\beta})$.

The most general approach, however, is to include mixing of the ligand part of the eigenfunctions (the two sub-hamiltonians H_α and H_β no longer commute with each other) i.e. $M \neq U$ and, therefore, to allow ESEEM as well as ENDOR effects to occur simultaneously. When the RF frequency is resonant with some frequency in the α manifold ω_{fg}^{α}, the matrix R_T^{α} in the trace [44] would have to be replaced by the combined nutation and free precession matrix $F^{\alpha}(T)$ (R_T^{β} would not be affected). In order to calculate this matrix first the time dependence of the RF-interaction hamiltonian has to be removed by applying a similar transformation as in eq. [25], i.e. entering the rotating frame for the nuclear spin coordinates. The hamiltonian in this representation (both microwave- and RF- rotating frame and H_0 representation) is expressed analogously to [26] as:

$$\mathcal{H}_N^{RF} = (\mathcal{H}_0^C + \mathcal{H}_0^L) - \hbar\omega\Sigma_S + \hbar\omega_{rf}\Sigma_I + V_{rf} \qquad [55]$$

The operator that transforms the ligand sub-hamiltonian to the rotating frame is given by:

$$R_L(t) = e^{i\omega_{rf}\Sigma_I t} \qquad [56]$$

Since the stimulated echo is (phase sensitive) detected at the microwave frequency, this "RF-transformation" should be present only at the time of the RF-irradiation and has to be made undone at the time of detection:

$$F^{\alpha}(T) = R_L^{\alpha}(\tau)\bar{F}^{\alpha}(T)R_L^{\alpha}\dagger(\tau+T) \qquad [57]$$

$\bar{F}$ represents the RF-nutation operator in the RF-rotating frame. In our case of a completely selective RF-pulse on an NMR transition f,g in the α-manifold, the nutation part of $\bar{F}^{\alpha}(T)$ has the same shape as [38]:

$$\bar{F}^{\alpha}(T) = e^{i(\omega_f^g+\omega_f^g)t} \begin{bmatrix} \cos\omega_p t & i\sin\omega_p t\ e^{i\phi_h} \\ i\sin\omega_p t\ e^{-i\phi_h} & \cos\omega_p t \end{bmatrix} \qquad [58]$$

ω_p is the RF-nutation frequency $(2\omega_p = \gamma|\langle f|H_{rf}|g\rangle|)$ ω_f^g and ω_g^g are the corrections on the precession frequencies of eigenstates f and g, imposed by the RF-rotating frame. When transition f,g is at resonance, the precession frequencies of f and g become equal, i.e. $\omega_f^g+\omega_f^g = \omega_g^{\alpha}+\omega_g^g$. When the RF irradiation is present during time T, F(T) has the following elements:

$$F_{ii}^{\alpha}(T) = e^{i\omega_i^{\alpha}T} \qquad i \neq f,g \qquad [59]$$

$$F_{ff}^{\alpha}(T) = \cos\omega_p T\, e^{i\omega_f^{\alpha}T}$$

$$F_{gg}^{\alpha}(T) = \cos\omega_p T\, e^{i\omega_g^{\alpha}T}$$

$$F_{fg}^{\alpha}(T) = i\sin\omega_p T\, e^{i\phi_b} e^{-i(\omega_f^{\beta}-\omega_g^{\alpha})\tau} e^{i\omega_g^{\alpha}T}$$

$$F_{gf}^{\alpha}(T) = i\sin\omega_p T\, e^{-i\phi_b} e^{i(\omega_f^{\beta}-\omega_g^{\alpha})\tau} e^{i\omega_f^{\beta}T}$$

The expression for the stimulated echo is now converted to

$$E_{endor}^{\alpha} = \langle M_y \rangle_{endor}^{\alpha}(2\tau+T) = \frac{1}{2}\{\, V(\tau,\tau+T) + V^{RF}(\tau+T,\tau) \,\} \qquad [60]$$

$$V^{RF}(\tau+T,\tau) = \frac{1}{2(2I+1)}\{\, Tr(R_{\tau}^{\beta\dagger} M^{\dagger} F_T^{\alpha\dagger} R_{\tau}^{\alpha\dagger} M R_{\tau}^{\beta} M^{\dagger} F_T^{\alpha} R_{\tau}^{\alpha} M) \,\}$$

In order to separate the τ-dependence of the ENDOR effect from the T-dependence (time T is kept constant in most applications of ESE-ENDOR), it is convenient to factor out the terms $e^{i\omega_{fg}\tau}$ in [59] ($\omega_{fg} = \omega_f - \omega_g$), making use of the fact that $\omega_f^{\alpha} - \omega_g^{\alpha} = \omega_g^{\sigma} - \omega_f^{\sigma}$, leading to the following redefinition of F_T^{α}:

$$F_T^{\alpha} = R_{\tau}^{\alpha\dagger} G_T^{\alpha} R_{\tau}^{\alpha} \qquad [61]$$

$$G_{ii}^{\alpha} = F_{ii}^{\alpha} \qquad \textit{(for all i)}$$

$$G_{fg}^{\alpha} = i\sin(\omega_p T) e^{i\phi_b} e^{i\omega_g^{\alpha}T}$$

$$G_{gf}^{\alpha} = i\sin(\omega_p T) e^{-i\phi_b} e^{i\omega_f^{\beta}T}$$

The new expression of V^{RF} is now:

$$V^{RF}(\tau+T,\tau) = \frac{1}{2(2I+1)}\left\{Tr(R_\tau^{\beta\dagger}M^\dagger R_\tau^{\alpha\dagger}G_T^{\alpha\dagger}MR_\tau^{\beta}M^\dagger R_\tau^{\alpha\dagger}G_T^{\alpha}R_\tau^{\alpha}R_\tau^{\alpha}M)\right\} \quad [62]$$

$$= \frac{1}{2(2I+1)}\left\{\sum_{u'jj'kn} e^{i\omega_{kn}^{\beta}\tau}e^{\imath\omega_{i'i}^{\alpha}\tau}e^{\imath\omega_{j'j}^{\alpha}\tau}M_{jn}^{*}M_{j'k}M_{ik}^{*}M_{i'n}G_{j'j}^{*}G_{ii'} + CC\right\}$$

In the limiting case where no forbidden EPR transitions are allowed, the state mixing matrix M is replaced by a unit matrix U. In this case it is readily inferred from equation [62] by putting j=n=i' and j'=k=i that the expression reduces to the one derived by Liao and Hartman (6). Their approximation of very short RF-irradiation does not seem to be necessary (!).

$$V_{fg}^{RF} = \frac{1}{2I+1}\{2\cos(\omega_{fg}^{\beta}-\omega_{fb}^{\alpha})\tau\sin^2\omega_p T + 2\cos^2\omega_p T + 2I-1\} \quad [63]$$

Where $\omega_p T = \frac{1}{2}\theta$, i.e. half the RF-pulse angle. Equation [62] is suitable for implementation in a simulation program. The stimulated echo as a function of τ will be modulated by combinations of three frequencies, two from the manifold in which the NMR transitions are induced, and one from the opposite manifold. The resulting signal will be very complicated. To illustrate this complexity, we present the complete ESE-ENDOR signal for the simplest case: S=1/2, I=1/2 and a 180° RF-pulse on ω_α. To this end the following substitutions are made in eq. [62]:

$$G_{11}^{\alpha} = 0 \quad ; \quad G_{22} = 0 \quad [64]$$

$$G_{12}^{\alpha} = ie^{-i\phi_b}e^{\imath\omega_1 T} \quad ; \quad G_{21}^{\alpha} = ie^{\imath\phi_b}e^{\imath\omega_2 T}$$

$$M = \begin{bmatrix} v & u \\ -u^* & v^* \end{bmatrix}$$

After a somewhat tedious but straighforward calculation, the following result is obtained:

$$V^{RF}(\tau+T,\tau) = 4|v|^2|u|^2\cos\omega_\alpha\tau \quad [65]$$

$$+ 2|u|^4\cos(\omega_\beta+\omega_\alpha)\tau + 2|v|^4\cos(\omega_\beta-\omega_\alpha)\tau$$

$$+ 4(1+cos\,\omega_\beta\tau)\cos\{\omega_\alpha(2\tau+T)+\phi\}\,|(u)^2(v)^2e^{i2\phi_b}|$$

where

$$\phi = arctg\frac{\mathrm{Re}(u^2v^2e^{i2\phi_b})}{\mathrm{Im}(u^2v^2e^{i2\phi_b})} \qquad [66]$$

The contribution from the β-manifold is not influenced by the RF-irradiation:

$$V(\tau,\tau+T) = |v|^4+|u|^4+|v|^2|u|^2\times \qquad [67]$$

$$\left\{\cos\omega_\alpha\tau + \cos\omega_\beta(\tau+T) + 2cos\,\omega_\alpha\tau\cos\omega_\beta(\tau+T)\right\}$$

Note that in the case of isotropic hyperfine interaction (u=0) only the third term in eq. [65] is retained which is equivalent to the expression derived by Liao and Hartman (6) and by Mims (7). It is striking that according to eq [65] phase shifted double frequency modulations occur as a function of τ. It would be interesting to verify this behaviour experimentally.

Summarizing, we can state that although we derived a closed form expression [62] for the ESE-ENDOR effect, in most cases the ESE-ENDOR signal and, therefore, the corresponding expression will be too complicated to be handled without a computer. However, the expression clearly indicates which combination frequencies can be expected.

References

1. C.P. Keijzers, G.F.M. Paulussen, and E. de Boer, Mol. Phys. *29*, 973 (1975)
2. D. Snaathorst and C.P. Keijzers, Mol. Phys. *51*, 509 (1984)
3. W.B. Mims, Phys. Rev. *B5*, 2409 (1972) ; W.B. Mims, Phys. Rev. *B6*, 3543 (1972)
4. R.P.J. Merks and R. De Beer, J. Phys. Chem. *83*, 3319 (1979)
5. H. Barkhuijsen, R. de Beer, E.L. de Wild, and D. van Ormondt, J. Magn. Reson. *50*, 299 (1982)
6. P.F. Liao and S.R. Hartmann, Phys. Rev. *B8*, 69 (1973)
7. W.B. Mims in "Electron Paramagnetic Resonance" (Geschwind Eds.) Plenum Press New York (1972)

JOURNAL OF MAGNETIC RESONANCE 60, 66–78 (1984)

CHAPTER V

An Electron Spin-Echo Envelope Modulation Study of ^{14}N Nuclear Hyperfine and Quadrupole Coupling in Copper(II)/Nickel(II) Bis(*N*,*N*-di-*n*-butyl-dithiocarbamate)

E. J. REIJERSE, M. L. H. PAULISSEN, AND C. P. KEIJZERS

Department of Molecular Spectroscopy, University of Nijmegen, Toernooiveld, 6525 ED Nijmegen, The Netherlands

Received April 24, 1984

The electron spin-echo envelope modulation technique (ESEEM) is used to determine the ^{14}N hyperfine and quadrupole tensors in copper-doped nickel(II) bis(*N*,*N*-di-*n*-butyl-dithiocarbamate) The line positions and peak intensities of the Fourier-transformed ESEEM spectra are interpreted using simulated spectra, obtained by diagonalizing the full spin-Hamiltonian matrix The ^{14}N quadrupole tensor can be accounted for theoretically by extended Huckel molecular orbital calculations. For the interpretation of the ^{14}N hyperfine tensor, however, an unrestricted molecular orbital calculation is necessary. Therefore, one should be cautious in drawing conclusions about spin-density distributions from small hyperfine couplings of nuclei in higher coordination spheres

It is well known that the amplitude of the electron spin echo can show a periodic variation superimposed on the relaxation decay (*1*). This modulation effect is caused by magnetic interactions between the electron spins and nuclear spins involving in general (a) hyperfine interactions (HFI), (b) nuclear Zeeman interactions (NZI), and (c) nuclear quadrupole interactions (NQI). The modulation frequency and amplitude depend on the magnitude of these interactions. By Fourier transformation of the echo envelope one obtains Fourier-transformed electron spin-echo envelope modulation spectra (FT-ESEEM spectra) from which the interactions can be determined, thus offering an alternative to conventional ENDOR (*2*). One attractive feature of the FT-ESEEM spectrum is that its intensities depend only on the spin Hamiltonian of the system and not, as in cw-ENDOR, on any relaxation rate. Therefore, the FT-ESEEM intensities can be calculated in a straightforward manner (*3*).

A necessary condition for the observation of the modulation effect is that the spin states of the system are mixed; i.e., during the excitation of the system by a microwave pulse both first-order "allowed" and "forbidden" transitions must occur simultaneously inducing a "branching" over the $M_s = +1/2$ and $M_s = -1/2$ manifolds. This requires HFI and/or NQI of the same order of magnitude as the NZI. In many systems which do have a NQI, this interaction turned out to be much smaller than the NZI and the HFI. In most of these cases it was neglected completely to obtain analytical expressions for the modulation pattern (*3, 4*). Only in a few instances was the NQI taken into account as a perturbation which affects only the amplitude of the modulations (*5*). However, we are interested in various

Jahn–Teller systems with nitrogen-containing ligands (*6*). Because the nitrogen atoms are in the second coordination sphere, it is to be expected that their HFI and most probably also their NQI are of the same order of magnitude as the NZI. Therefore, in these systems we had no other alternative than to diagonalize the complete spin-Hamiltonian matrix and to make use of the exact modulation formula (*3*).

Since these Jahn–Teller systems contain at least three sets of two equivalent nitrogen atoms, which gives rise to very complicated spectra, we decided to measure first a system with only one set of equivalent nitrogen molecules but with HFI and NQI which are expected to be of the same order of magnitude as the NZI. For this model system, we have chosen copper(II)/nickel(II) bis(*N*,*N*-di-*n*-butyl-dithiocarbamate) (Cu/Ni(bu_2dtc)$_2$) because much is known already about its electronic structure from EPR and ENDOR measurements and various molecular orbital (MO) calculations (*7–10*).

EXPERIMENTAL

The 1% Cu-doped Ni(bu_2dtc)$_2$ crystals were grown by slow evaporation of an acetone solution that contained the two complexes in the appropriate ratio.

Field swept spectra were measured by continuously monitoring the intensity of a two-pulse echo (pulse sequence: $\pi/2$–τ–π–τ–echo, i.e., two microwave pulses separated by time τ) while sweeping the magnetic field. These spectra are equivalent to a conventional cw-EPR spectrum in absorption mode.

The ESEEM spectra were measured using the stimulated echo sequence ($\pi/2$–τ–$\pi/2$–T–$\pi/2$–τ–echo) which consists of three equal pulses (*11*), and sweeping time T between the second and the third pulse. For τ, a constant value of 300 ns was used. T was swept from 1 to 51 μs in steps of 0.1 μs. The repetition time was 10 ms.

All measurements were carried out at a temperature of 15 K in an Oxford CF200 liquid helium flow cryostat with two orthogonal rotation axes (one inside the stripline resonator ($Q \sim 100$ (12)) and one being the cavity itself).

The microwave pulses had a length of 20 ns and were generated by a home-built programmable pulse generator with a time resolution of 10 ns. They were amplified by a 1 kW Litton TWT amplifier. The electron spin echoes were sampled and integrated in a boxcar PAR 162/164. The data were collected and processed in a MINC 11/23 minicomputer with home-written software. The modulation envelopes were transformed into the frequency domain using standard procedures: high-pass filtering (cut-off frequency 50 kHz), Fourier transformation, and transformation to amplitude mode. The microwave frequency was measured with a Hewlett–Packard 5246L counter, equipped with a 5255A plug-in unit. The magnetic field was monitored with a Bruker B-NM12 gauss meter.

RESULTS

Determination of the Nitrogen Interactions

Figure 1 shows a typical field-swept spectrum. The host crystal has space group $P2_{1/c}$, with two magnetically nonequivalent molecules per unit cell. Since the

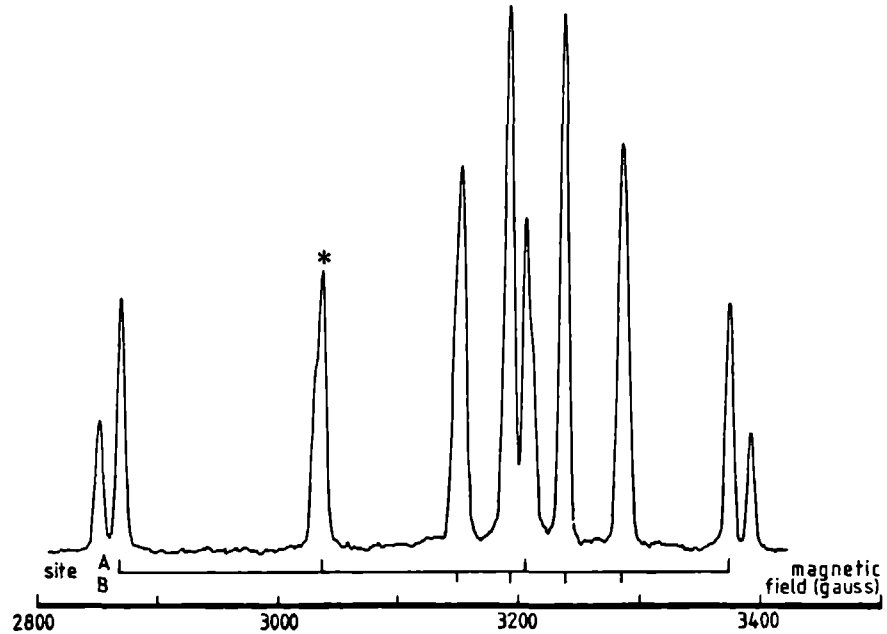

FIG. 1. Field-swept spectrum of 1% Cu doped $Ni(bu_2dtc)_2$ in the YZ plane. Angle with Y axis = 80°, τ = 300 ns.

copper-containing molecules accept the structure of the nickel complex (*10, 14*), this gives rise to two copper hyperfine quartets (except when the magnetic field is along the *b* axis or in the *ac* plane). All lines are partly split due to the naturally occurring ^{63}Cu and ^{65}Cu isotopes, each with a nuclear spin 3/2 but with a slightly different magnetic moment. From these field-swept ESE spectra we determined the *g*, the Cu-HFI, and the Cu-NQI tensors. The principal values are listed in Table 1. The principal axes of the *g* tensor are indicated in Fig. 2. They were chosen as the axes of rotation in the determination of the ^{14}N coupling tensors. The maximum *g* value and the maximum copper HFI coincide along the normal to the molecular plane. In the plane, both tensors are almost axial. Surprisingly, the HFI tensor has been rotated by 29° relative to **g**. However, one should bear in mind that the error in the in-plane angle is quite large because of the mentioned near axiality. The Cu NQI is very small compared to the Cu HFI. Its maximum value coincides with the maximum Cu HFI and the maximum *g* value along the normal to the molecular plane. However, the NQI tensor is clearly nonaxial, as opposed to the other two tensors.

The ESEEM spectra were recorded by pulsing on one of the copper-hyperfine lines of one site (marked with an asterisk in Fig. 1). In Fig. 3 a typical ESEEM spectrum is shown; the filtered signal and the FT spectrum are also presented. The angular dependence of the FT-ESEEM spectra in the *YZ* plane of the molecule is shown in Fig. 4. From the comparison of these FT-ESEEM spectra with some spectra measured for the analogous ethyl complex, we concluded that only the shaded peaks are due to ^{14}N coupling in the complex. The other signals most

TABLE 1

Measured and Calculated S Hyperfine, ^{63}Cu Hyperfine, and Quadrupole Interaction Tensors (in Units of 10^{-4} cm^{-1}) and g Tensor of Cu/Ni(R_2dtc)$_2$ Complexes

	Measured		Calculated			
R·	n-Butyl	Ethyl	Ethyl	H	H	H
Temp	15 K	25 K				
Method	ESE	ESR[a]	EH[b]	EH[c]	UHFS[d]	RHFS[d]
g_x	2 016	2 017	2.019	2 020	2 029	2 029
g_y	2.023	2.020	2 024	2 025	2.037	2 039
g_z	2 084	2 084	2 074	2.078	2.116	2.114
Cu–A_1	43 8 [29][e]	42 6	39 6	40 6	44 3	38 5
A_2	39 9 [29][e]	41.4	38 9	39.9	45 0	41.1
A_z	−83 7 [1][e]	−84 0	−78 6	−80 5	−89 3	−79 6
A-iso	−81 7	−84.5	0 0	0 0	−56 9	22.9
Cu–P_x	−0 9 [2][e]		−1.4	−1 4		
P_y	−0 3 [2][e]		−1 3	−1 3		
P_z	1.2 [2][e]		2 7	2 8		
S–A_1		10 2	10.4	10.3	7 8	7.8
A_2		−5 9	−5.1	−5 1	−4 0	−3 9
A_3		−4.3	−5 2	−5 2	−3 8	−3 9
A-iso		11 6	11 3	11 7	17 0	12 2

[a] g tensor and copper data obtained from ref (*10*) Sulphur data obtained from Ref (*16*)
[b] Data based on EH calculations of Ref (*9*) with ethyl groups retained
[c] Data based on EH calculations of Ref (*9*) with ethyl groups replaced by protons.
[d] Data obtained from Ref (*8*)
[e] Angle of the principal axis with the corresponding one of the g tensor.

probably originate from strong couplings with protons of neighbor molecules. From the line positions in the three measured planes (depicted in Fig. 5), it can easily be concluded that the ^{14}N coupling tensors are almost axial in the XY plane. This gave a clue to the assignment of the peaks in the spectra: model calculations could be restricted to axial and coinciding HFI (A^N) and NQI (P^N) tensors. They led to the assignment of the peaks as indicated in Fig. 5. The corresponding energy-level diagram for the orientation of the ESEEM spectrum in Fig. 3 is given in Fig. 6. Because the two ^{14}N atoms in the complex are equivalent, all line positions in Fig. 5 were fitted to this six-level scheme of one electron and one ^{14}N nucleus. The introduction of the second ^{14}N spin results only in small splittings of the ^{14}N lines

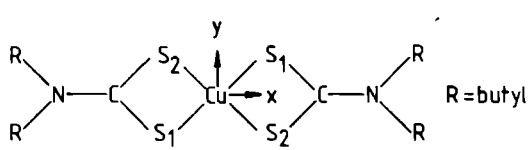

FIG. 2 Orientation of the principal axes of g (tensor) in Cu/Ni(bu_2dtc)$_2$

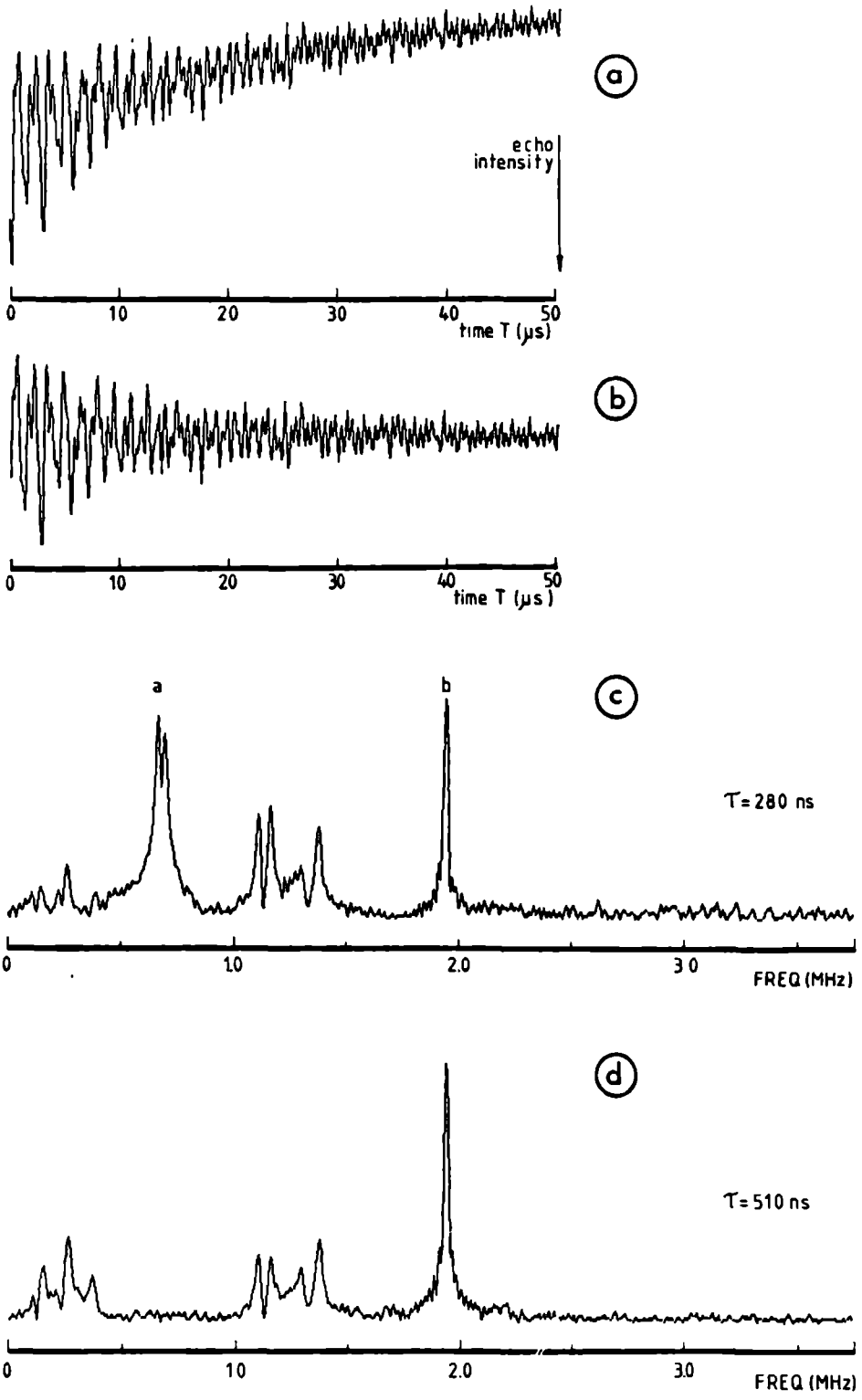
a
echo
intensity
0
10
20
30
40
50
time T (μs)
b
0
10
20
30
40
50
time T (μs)
a
b
c
T = 280 ns
0
1.0
2.0
3.0
FREQ (MHz)
d
T = 510 ns
0
1.0
2.0
3.0
FREQ (MHz)

which splittings are, albeit observable in the spectra (e.g., peak a in Fig. 3c), too small to affect the fit of the ^{14}N interaction tensors. Further refinement was accomplished by relaxing the restrictions of axial and coinciding nitrogen tensors and by including the g and Cu-HFI tensors. The resulting nitrogen tensors are presented in Table 2. As expected, they are almost axial in the XY plane. The HFI is dominated by its isotropic part, which is three times as large as the anisotropic contribution. Along the principal axis, perpendicular to the molecular plane, the HFI and the NQI are almost equal ($\sim 0.5 \times 10^{-4}$ cm^{-1}) and of the same order of magnitude as the nuclear Zeeman interaction ($\sim 0.3 \times 10^{-4}$ cm^{-1}). This prevented the use of approximate formulae for the modulation pattern, as was mentioned above. By fitting the FT-ESEEM spectra we could not distinguish the absolute or relative signs of the interactions; the signs listed in Table 2 are based on theoretical calculations (see below).

Intensities of the Spectra

To check the reliability of the measured tensors we calculated the modulation intensities with the general equations derived by Mims (*3*). The intensity of a three-pulse echo is a function of time τ between the pulses 1 and 2, and time T between the pulses 2 and 3; apart from relaxation effects and instrumental properties, it is given by the following equation:

$$E_\tau(T) = \chi_0 + \frac{1}{2}\sum_{i>j}\chi_{ij}\cos\omega_{ij}\tau + \frac{1}{2}\sum_{k>n}\chi_{kn}\cos\omega_{kn}\tau + \sum_{i>j}\cos\omega_{ij}(T+\tau)$$
$$\times\left(\frac{1}{2}\chi_{ij} + \sum_{k>n}\chi_{ij,kn}\cos\omega_{kn}\tau\right) + \sum_{k>n}\cos\omega_{kn}(T+\tau)\left(\frac{1}{2}\chi_{kn} + \sum_{i>j}\chi_{ij,kn}\cos\omega_{ij}\tau\right) \quad [1]$$

where $i \neq j$ and $k \neq n$ and indices i, j run over the spin states within the electron spin manifold $M_s = -1/2$, while k, n run over the states of electron spin manifold $M_s = +1/2$. The quantity ω_{ij} is the energy difference (in rad s^{-1}) between the i and j spinstate. The terms in Eq. [1] which describe the amplitudes of the modulations have the following form:

$$\chi_0 = \left[\frac{1}{2I+1}\right]\sum_{i,k}|M_{ik}|^4 \quad [2]$$

$$\chi_{ij} = \left[\frac{2}{2I+1}\right]\sum_{k}|M_{ik}|^2|M_{jk}|^2 \quad [3]$$

$$\chi_{kn} = \left[\frac{2}{2I+1}\right]\sum_{i}|M_{ik}|^2|M_{in}|^2 \quad [4]$$

FIG. 3. (a) Typical ESEEM signal measured on the second peak of site A at the same orientation as in Fig. 1, τ = 280 ns. (b) Corresponding filtered signal (cutoff frequency = 50 kHz). (c) FT-ESEEM spectrum, 1000 points, Fourier transform of signal in Fig. 3b. (d) FT-ESEEM spectrum, 1000 points, τ = 510 ns, same orientation. The choice of τ = 510 ns ($1/\tau$ = 1.9 MHz) suppresses the corresponding frequency of peak b in the other M_s manifold (apparently peak a).

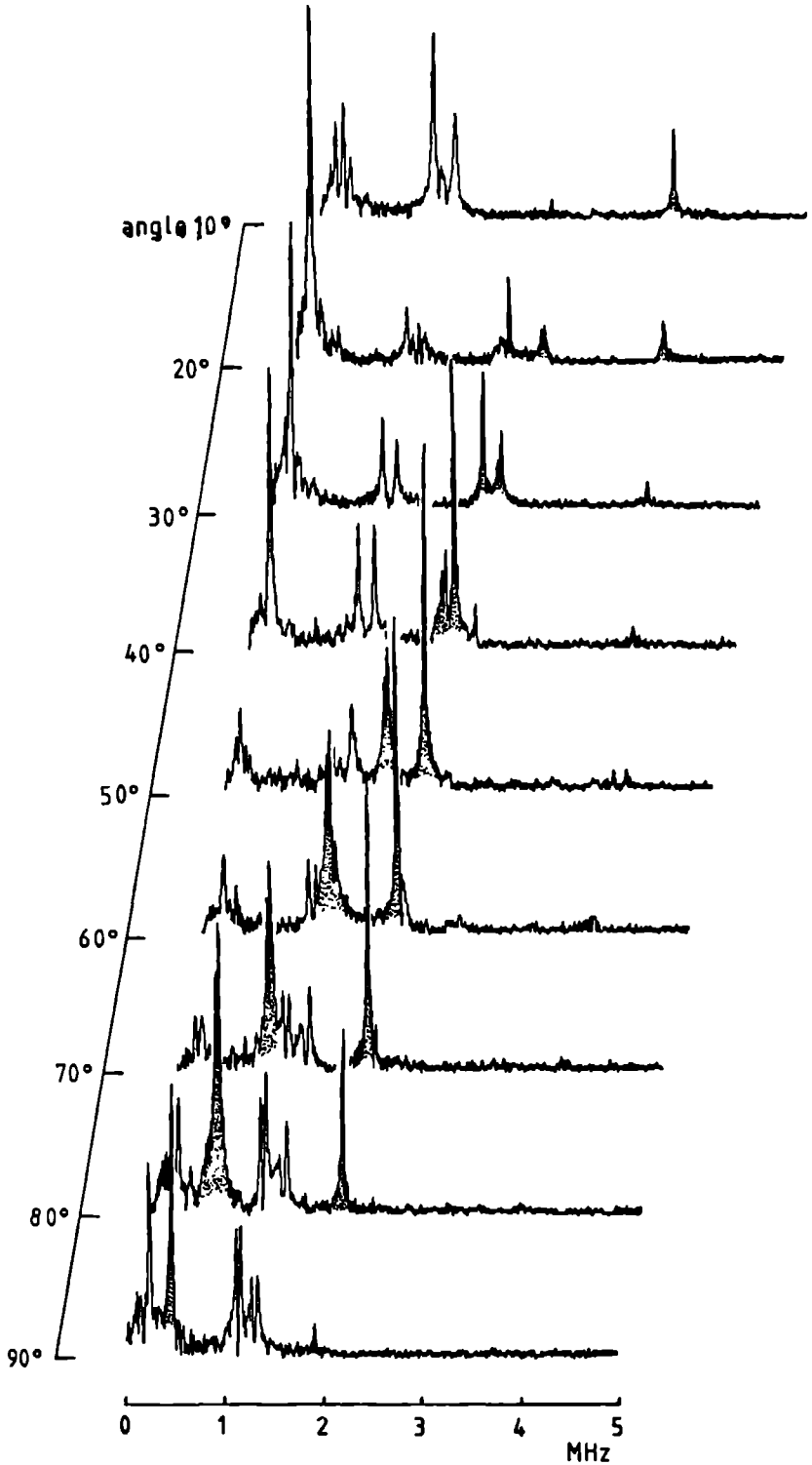

FIG. 4. Angular dependence of FT-ESEEM spectra in the *YZ* plane.

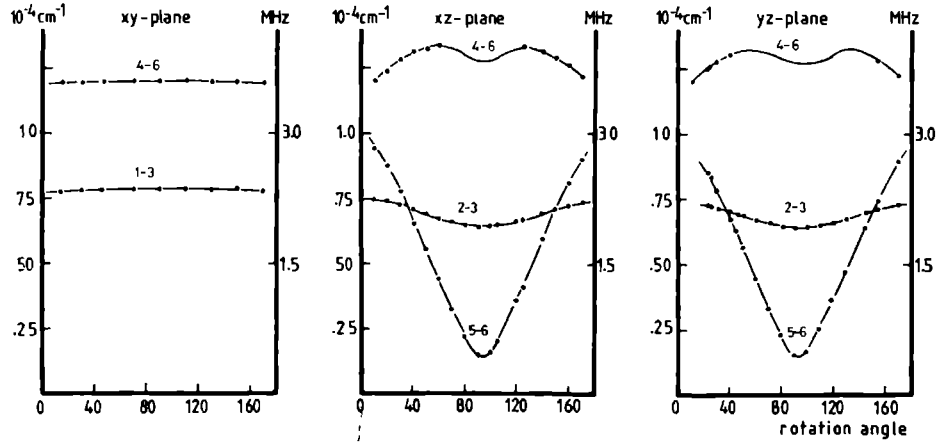

FIG. 5. Line positions of FT-ESEEM spectra in three planes.

$$\chi_{ij,kn} = \left[\frac{2}{2I+1}\right] \mathrm{Re}(M^*_{ik}M_{in}M^*_{jn}M_{jk}). \qquad [5]$$

M_{ik} are the elements of a unitary state-mixing matrix with dimension $2I + 1$; they can be referred to as the EPR transition moments from state i to state k. The transition moments can be calculated from the eigenvectors of the Hamiltonian (*3*). From this equation it is clear that the amplitude of the modulation at frequency ω_{ij}, is modulated with frequency ω_{kn} from the other M_s manifold and vice versa. By chosing appropriate values for τ, one is able to suppress or enhance the amplitude of frequencies of the *opposite* manifold. Complete suppression can occur when $\chi_{i,j} = \chi_{k,n}$, $\chi_{ij,kn} = -(1/2)\chi_{k,n}$ (which appeared to be the case for our spin Hamiltonian) and τ is chosen such that it is a multiple of $2\pi/\omega_{ij}$ or $2\pi/\omega_{kn}$. In this way one can use the suppression effect to assign modulation frequencies to different M_s manifolds. This is demonstrated in Figs. 3c and d where peaks a and b are assigned to different M_s manifolds. The calculated intensities for the three-pulse ESEEMs with τ = 300 ns are plotted as a function of the angle in the YZ plane in Fig. 7. In the calculation we used a spin Hamiltonian with one electron spin $S = 1/2$, and two ^{14}N nuclear spins $I = 1$; the Cu spin $I = 3/2$ was omitted as it turned out to have hardly any influence. It should be noticed, however, that for the calculation of the line positions (vide supra) only one of the two equivalent ^{14}N nuclear spins was taken into account. The introduction of the second (equivalent) ^{14}N spin led only to small splittings in the ^{14}N line positions but, more important, it leads also to an increase of the calculated intensities by a factor of 1.7 as compared to the one-^{14}N spin case. In principle it is possible to determine the "normalized" modulation intensities (relative to the echo intensity) from the spectra (*13*). However, the overlap with proton signals, the mentioned splittings of the ^{14}N signals and the limited S/N ratio prevented us from obtaining reliable intensity data from the spectra, but as can be judged from a comparison of Figs. 4 and 7, the overall correspondence of the calculated intensities and the experimental data is very good.

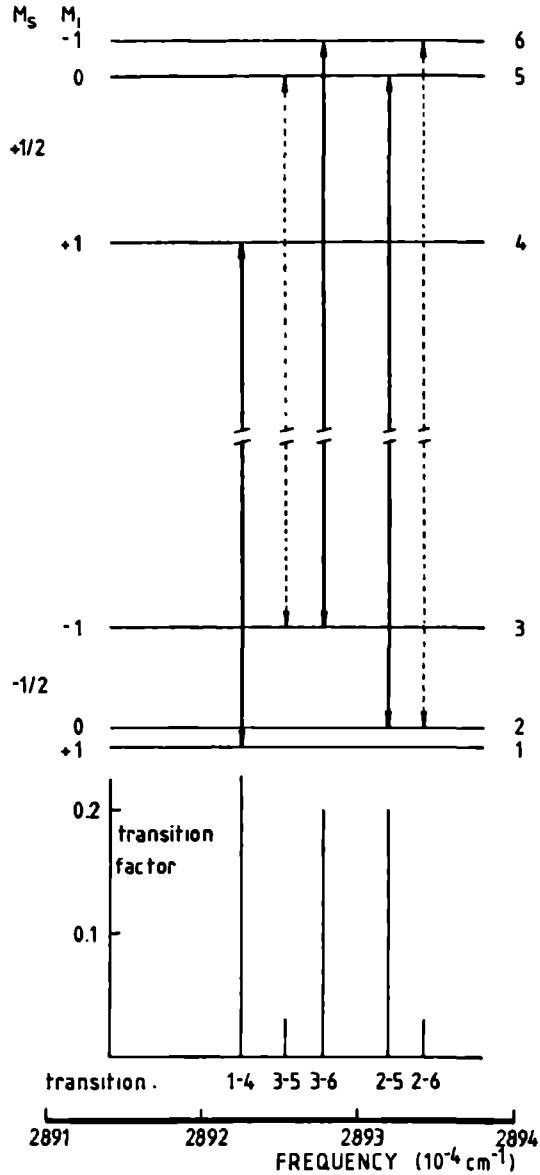

FIG. 6. Calculated energy-level diagram using a spin Hamiltonian with one electron spin $S = 1/2$ ($g = 2.032$) and one ^{14}N nuclear spin $I = 1$ with the hyperfine interaction and quadrupole interaction of Table 2 for the orientation of Fig. 1.

DISCUSSION

The g tensor and the Cu-HFS data are in agreement with the data of Weeks and Fackler (*14*) and Snaathorst *et al.* (*10*) for the ethyl complex. The ^{14}N data can only be compared with the ENDOR studies by Kirmse *et al.* (*15*), also for the ethyl

TABLE 2

Measured and Calculated ^{14}N-Hyperfine and Quadrupole Interaction Tensors in $Cu/Ni(R_2dtc)_2$ Complexes (in Units of 10^{-4} cm^{-1})

	Measured		Calculated							
			1-center				2 + 3-center	1 + (2 + 3)center[j]		
R	*n*-Butyl	Ethyl	Ethyl	H	H	H	H			
Temp	15 K	27 3 K								
Method	FT-ESEEM	ENDOR[a]	EH[b,g]	EH[c,g]	RHFS[d]	URHF[d]	EH[e]	EH	RHFS	UHFS
N–A_x	0 06		−0 01	−0 01	−0 03	0 08	0 05	0 04	0 02	0 13
A_y	0 06		0 02	0 02	0 05	0 16	−0 01	0 01	0 04	0 15
A_z	−0 12 [2][h]		−0 01	−0 01	−0 03	−0 24	−0 04	−0 05	−0 07	−0 28
A-iso	−0 375	0 50	0 0	0 0	0 0	−0 56	0 0	0 0	0 0	−0 56
N–P_x	0 24		0 55	0 66						
P_y	0 23		0 46	0 41						
P_z	−0 47 [3][h]	0 35 [17][h]	−1 01	−1 07						

[a] Data obtained from Ref (*15*)
[b] Data based on EH calculations from Ref (*9*), with full ethyl groups retained
[c] Data based on EH calculations from Ref (*9*), with ethyl groups replaced by protons
[d] Data obtained from Ref (*8*)
[e] Data obtained from Ref (*9*)
[j] 1-center contribution from method mentioned (2 + 3)-center from EH method of Ref (*9*)
[g] The 1-center contributions calculated with the EH method include first- and second-order contributions
[h] Angle of the principal axis with the corresponding one of the g tensor.

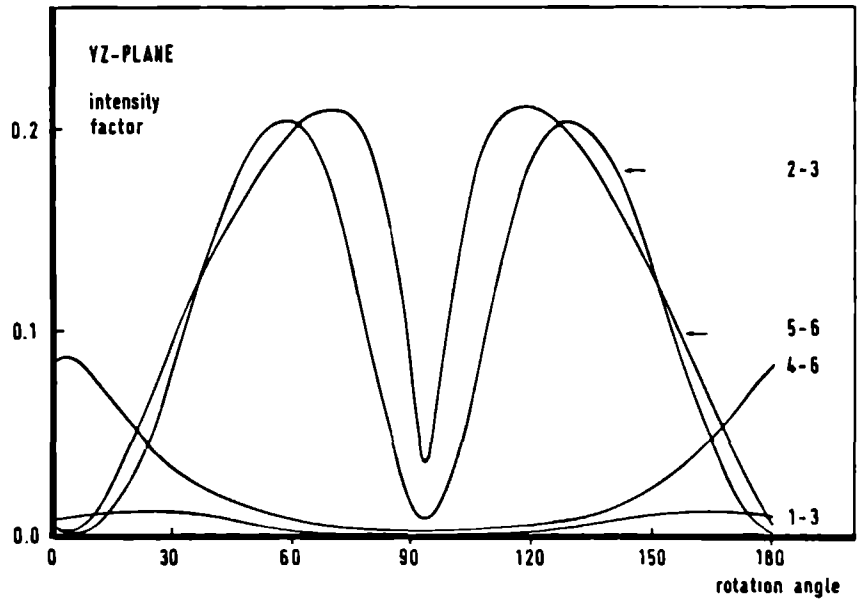

FIG. 7. Calculated three-pulse FT-ESEEM intensities (τ = 300 ns) in the YZ plane; the numbering of the energy levels is according to Fig. 6. 4° = Y axis; 94° = Z axis.

complex. Because the ENDOR signals were too weak for a full rotational study, only approximate values could be obtained; these are listed in Table 2. Their data show some deviations from ours: In our study both the maximum P^N and A^N direction coincide with the maximum g direction, while the study of Kirmse *et al.* indicates for the P_{max} direction a deviation of 17 ± 5° from the molecular axis system (Fig. 2); both, the estimated A^N-iso and the P^N_{max} values show a deviation of ~25% from our values. On the other hand, the estimated order of magnitude of 0.1×10^{-4} cm^{-1} for the dipolar part of the ^{14}N hyperfine interaction, agrees with our experimental result.

Several studies have been made to calculate the magnetic coupling parameters of Cu/Ni(et$_2$dtc)$_2$ (*7–9*). The most recent calculation (*9*) included two- and three-center contributions to the first-order anisotropic HFI. The second-order HFI is generally rather small, and two- and three-center integrals are, therefore, neglected. The first-order contribution is brought about by the electron spin–nuclear spin dipole–dipole interaction (e.g., with nucleus N) and can be expressed as

$$A^N_{ij} = \left(\frac{\mu_0}{4\pi}\right) g_e g_N \mu_b \mu_n \left\langle \psi_0 \left| \frac{F^N_{ij}}{r^3_N} \right| \psi_0 \right\rangle \qquad [6]$$

where μ_0 is the permeability of free space, μ_b is the Bohr magneton, g_e the free-electron g value, and g_N the gyromagnetic ratio of nucleus N; i, j are x, y, z, F^N_{ij} is a component of a symmetrical traceless tensor operator related to the dipolar interaction and r_N is the electron–nucleus distance. If ψ_0, the molecular orbital of the unpaired electron, is expanded as a linear combination of atomic orbitals ϕ^A_i centered on nuclei A, then Eq. [6] can be rewritten

$$A_{ij}^{N} = \left(\frac{\mu_0}{4\pi}\right) g_e g_N \mu_b \mu_n \times \sum_A \sum_B \sum_{i \in A} \sum_{j \in B} \left\langle C_i^A \phi_i^A \left| \frac{F_{ij}^N}{r_N^3} \right| C_j^B \phi_j^B \right\rangle$$
$$= (A_{ij}^N)_1 + (A_{ij}^N)_{2,1} + (A_{ij}^N)_{2,2} + (A_{ij}^N)_3 \qquad [7]$$

where $(A_{ij}^N)_1$ and $(A_{ij}^N)_3$ are the one and three-center contributions, respectively. $(A_{ij}^N)_{2,1}$ and $(A_{ij}^N)_{2,2}$ are two-center contributions, $(A_{ij}^N)_{2,2}$ having one atomic orbital centered on nucleus N (A or B = N) and $(A_{ij}^N)_{2,1}$ having both orbitals centered on the same nucleus, not being N (A = B ≠ N). In Ref. (*9*), the hyperfine couplings were calculated with spin densities which were obtained from extended Hückel (EH) calculations in which the ethyl groups of the complex were replaced by protons. This reduces the computing time considerably but, since it is to be expected that this approximation will not be valid for the ^{14}N NQI, we used those EH data from Ref. (*9*) which were obtained by retaining the ethyl groups. The calculated first- and second-order one-center contributions to the hyperfine interactions of copper, sulfur, and nitrogen and to the quadrupole couplings of copper and nitrogen are summarized in Tables 1 and 2. The experimental g and the A^{Cu} and A^S tensors are in good agreement with the theoretical calculations, both with the semi-empirical extended Hückel (EH) method and with the ab initio Hartree–Fock–Slater (HFS) method. The picture that emerges from both methods is that the unpaired electron is located in the center of the molecule: ~50% on Cu and ~50% on the four sulfur atoms. The density on the other atoms is very small. It is, therefore, to be expected that the anisotropic dipolar part of the A^N tensor is dominated by two- and three-center interactions between the magnetic moment of the nitrogen nucleus and the unpaired electron on copper and sulfur (*9*). Hence, the main principal axis of A^N is expected to be located in the molecular plane, pointing from N to Cu (if the molecule has D_{2h} symmetry). Is was, therefore, very surprising that the axial component of A^N is not located along the X axis but, on the contrary, points along the Z axis, perpendicular to the molecular plane.

It turned out that the restricted MO methods (both EH and RHFS) could not explain this discrepancy. Both methods yield a one-center contribution which is axial along the Y axis (because of the fact that the unpaired electron is located in the p_y orbital of N, which orbital mixes with the $3d_{xy}$ orbital of Cu). The (2 + 3)-center contributions were calculated only from the spin densities which were obtained via the EH method with the same procedure as was used in Refs. (*9, 10*). From previous calculations of ^1H-hyperfine interactions in the same molecule, it was concluded that these multicenter terms are very accurate, notwithstanding the semi-empirical nature of this MO method (*9, 10*).

The multicenter contribution is of the same order of magnitude as the one-center term and far from axial: its minimum value is along Y, the direction of maximum one-center contribution! The total of the calculated A^N tensor has its maximum value along Z. The deviation from axial symmetry is much larger than in the experiment. The strongest discrepancy is, however, that the calculated isotropic part of the tensor is zero, as must be expected for an MO with b_{1g} symmetry. To explain the full tensor, we must turn to the results of unrestricted HFS calculations (*8*) (Table 2). They yield a one-center contribution which indeed has its main axis along Z and also has a large isotropic component. The correction with the (2 + 3)-

center contributions (from EH) results in a tensor which has the experimental symmetry but is too large. The latter must be caused by an overestimation of the very small spin-density on N.

The quadrupole-interaction tensor was calculated only with the EH method. Although it is too large, its symmetry is in perfect agreement with the experiment.

CONCLUSION

It is shown that in a transition-metal complex the magnetic interaction parameters of weakly coupled nuclei can be determined accurately by FT-ESEEM spectroscopy. Theoretically, however, these parameters can only be accounted for by unrestricted molecular orbital calculations. This implies that one has to be very careful in extracting information about chemical bonding from these experimental results.

ACKNOWLEDGMENTS

The authors gratefully acknowledge the indispensible technical support from Mr. Jan van Os and Mr. Adrie Klaassen who designed and built our electron spin echo spectrometer. Professor E. de Boer who initiated our activities in the field of ESE spectroscopy is thanked for critically reading the manuscript and for his continued interest. This work is financially supported by the Netherlands Foundation for Chemical Research (SON).

REFERENCES

1. L. G. ROWAN, E. L. HAHN, AND W. B. MIMS, *Phys. Rev. A* **137**, 61 (1965).
2. H. BARKHUYSEN, R. DE BEER, E. L. DE WILD, AND D. VAN ORMONDT, *J. Magn. Reson.* **50**, 299 (1982).
3. W. B. MIMS, *Phys. Rev. B* **5**, 2409 (1972); *Phys. Rev. B* **6**, 3543 (1972).
4. W. B. MIMS *in* "Electron Paramagnetic Resonance" (S. Geschwind, Ed.), Chap. 4, Plenum, New York, 1972.
5. A. A. SHUBIN AND S. A. DIKANOV, *J. Magn. Reson.* **52**, 1 (1983).
6. J. S. WOOD, C. P. KEIJZERS, E. DE BOER, AND A. BUTTAFAVA, *Inorg. Chem.* **19**, 2213 (1980).
7. C. P. KEIJZERS, H. J. M. DE VRIES, AND A. VAN DER AVOIRD, *Inorg. Chem.* **11**, 1138 (1972).
8. P. J. M. GEURTS, P. C. P. BOUTEN, AND A. VAN DER AVOIRD, *J. Chem. Phys.* **73**, 1306 (1980).
9. C. P. KEIJZERS AND D. SNAATHORST, *Chem. Phys. Lett.* **69**, 348 (1980).
10. D. SNAATHORST, C. P. KEIJZERS, A. A. K. KLAASSEN, E. DE BOER, V. P. CHACKO, AND R. GOMPERTS, *Mol. Phys.* **40**, 585 (1980).
11. E. L. HAHN, *Phys. Rev.* **80**, 580 (1950).
12. J. L. DAVIS AND W. B. MIMS, *Rev. Sci. Instrum.* **49**, 1095 (1978).
13. H. BARKHUYSEN, R. DE BEER, AND D. VAN ORMONDT, *Chem. Phys. Lett.* **101**, 494 (1983).
14. M. J. WEEKS AND J. P. FACKLER, *Inorg. Chem.* **7**, 2548 (1969).
15. R. KIRMSE, U. ABRAM, AND R. BÖTTCHER, *Chem. Phys. Lett.* **90**, 9 (1982).
16. R. KIRMSE AND B. V. SOLOVEV, *J. Inorg. Nucl. Chem.* **39**, 41 (1977).

CHAPTER VI[†]

Electron Spin Echo Envelope Modulation study of bis(tetrabutylammonium) bis(maleonitriledithiolato) Nickelate(II) doped with Copper(II)

E.J. Reijerse, A.H Thiers, R. Kanters, M C.M. Gribnau and C P. Keijzers,

Department of Molecular Spectroscopy,
Research Institute of Materials
University of Nijmegen, Toernooiveld, 6525 ED Nijmegen, The Netherlands

The Electron Spin Echo Envelope Modulation (ESEEM) technique is used to determine the ^{14}N hyperfine and quadrupole interaction tensors in bis(tetrabutylammonium) bis(maleonitriledithiolato) Cu(II), 3% doped in the diamagnetic Ni(II) host The line positions and peak intensities of the Fourier transformed ESEEM spectra are interpreted by using simulated spectra The latter are obtained by diagonalizing the full spin-Hamiltonian matrix which includes interactions of the ^{63}Cu spin I = 3/2 and two non-equivalent ^{14}N spins I = 1 A good correspondence between the experimental and the simulated spectra is obtained The ^{14}N-hyperfine and quadrupole interactions are calculated with Molecular Orbital coefficients obtained with an Extended Huckel method For the calculation of the hyperfine interactions, two- and three-center contributions are included The correspondence with the experimental tensors is astonishing! In the interpretation of the electronic structure a comparion is made with earlier work on Cu(II)/Ni(II) bis (N,N di-n-butyl-dithiocarbamate)

[†] Submitted for publication in the "Journal of Chemical Physics"

VI.1 Introduction

Complexes of transition metals with dithiolene ligands have been studied extensively with EPR and various other techniques (1-9) because of their interesting properties: formation of 1-dimensional conductors (3,10) and π-donor-acceptor complexes (11,13) and the stabilization of rare, formal, oxidation states (14,15). Especially the rare oxidation states, but probably also the other properties, are caused by the highly covalent character of the metal-sulphur bond by which the actual charge of the metal-ion is much smaller than the formal charge. This highly covalent character is confirmed by molecular orbital (MO) calculations (8) and, as far as the unpaired spin density is concerned, by EPR experiments (1). With the last technique, and especially with related methods as ENDOR, it is possible to measure hyperfine interactions (HFI's) with the sulphur atoms (16) and recently also with the atoms in the second and higher coordination spheres (8,9). This resulted in a very good insight in the electronic structure of these systems, especially in the density distribution of the unpaired electron. Therefore, these molecules are very good test systems for MO calculations but also for new experimental techniques.

Electron Spin Echo Envelope Modulation (ESEEM) is such a technique that was described already years ago (17,18) but that is reaching perfection only in the last years. The advantage of this technique, as compared to ENDOR, is that the line intensities are not influenced by relaxation effects so that they can be calculated easier, *in principle*. A disadvantage of this technique is that the spectra may be very complicated, especially for quadrupole nuclei and certainly for powder samples. In order to analyse these spectra, it is necessary to be able to generate reliable simulations. This is the reason why recently a number of papers was published, with theoretically calculated spectra, which test the limits of the interpretations (19,21).

In order to judge the quality of the calculated spectra it is necessary to compare them with good quality experimental spectra. For that purpose powder samples are difficult, especially if the g-value is isotropic because in that case all orientations are excited at once. Therefore, single crystals are much better suited for this purpose. That is why we measured recently the ^{14}N interactions in the system Copper bis(N,N di n-butyldithiocarbamate) ($Cu(dtc)_2$) doped in the diamagnetic Nickel host (22). Although this is a simple system with only two equivalent (inversion symmetry) nitrogen atoms, the analysis of the spectra was quite difficult since the HFI, the nuclear quadrupole interaction (NQI) and the nuclear Zeeman interaction (NZI) were of the same order of magnitude. In a second paper we published the powder spectra of this system and also the simulated spectra which were of a very good quality (23).

In this respect, the system Copper bis(maleonitriledithiolate)$^{2-}$ ($Cu(mnt)_2^{2-}$) diluted in the diamagnetic Nickel(II) host is a challenge because this molecule contains two sets of two equivalent nitrogen atoms (see I) so that the spectra are expected to be much more complex.

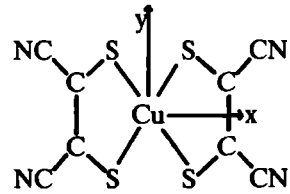

I

Furthermore, the Cu-N distance is much larger than in $Cu(dtc)_2$ (fourth and third coordination sphere, respectively) so that a different ratio of the HFI, NQI and NZI is to be expected. This system is therefore another, demanding, test for the ESEEM simulation program that has been improved considerably recently.

Another reason to study this system with ESEEM is that CW-ENDOR succeeded in measuring ^{13}C HFI (8) (also in the non-planar Zn-host (9)) of the ring- and the CN-carbon atoms but ^{14}N interactions could be observed only in a few directions. This was rather surprising because $Cu(dtc)_2$ caused no problem at all for the CW technique, neither for the ^{13}C (24,25) nor for the ^{14}N (25,26) interactions. A possible reason is that the NMR transition probabilities are larger in $Cu(dtc)_2$ because of a larger HFI (smaller Cu-N distance). In section 4 of this paper we compare and discuss the calculated dtc- and mnt-spectra. In Section 2 the experimental techniques are reported and the experimental results are presented in section 3. In section 5 the experimental results are discussed on the basis of M.O. calculations and elaborate computations of the spin Hamiltonian parameters.

VI.2 Experimental

The measurements were performed at 30K in an Oxford Instuments CF200 helium flow cryostat with two orthogonal rotation axes by which every crystal orientation relative to the magnetic field can be reached. With the help of field swept spectra, the crystal was oriented in the principal axis system of the g-tensor. These spectra were measured by monitoring the intensity of a two-pulse echo (pulse sequence $\pi/2 - \tau - \pi - \tau$ - echo, τ = 210 nsec) while sweeping the dc magnetic field.

Spectra were measured with orientation intervals of 5-10°. From the field swept spectra, the g-tensor and the copper HFI tensor are obtained which can be compared with literature data (1,27) in order to judge the accuracy of the measurements.

The ESEEM spectra were measured with the stimulated echo sequence ($\pi/2$ - τ - $\pi/2$ - T - $\pi/2$ - τ - echo, τ=210 nsec, repetition time = 3 msec.) by sweeping the time T from 0.80 to 26.35 μsec in steps of 50 nsec. The length of the $\pi/2$ pulses was 20 nsec. The spectrometer has been described previously (22). The magnetic field and the microwave frequency were measured with a Bruker B-NM12 gauss meter and a Hewlett-Packard 5246L counter, respectively.

The copper and nickel complexes, $(N-but_4)_2M(mnt)_2$ $M=Cu,Ni$), were synthesized according to the literature method (28). Single crystals with ~ 1% Cu in the diamagnetic Ni(II) complex were grown by slow solvent evaporation of an acetone/ethanol solution of the two complexes in the mentioned concentration ratio.

VI.3 Experimental results

Both, guest and host, crystallize in the triclinic space group $P_{\bar{1}}$ with Z=1. In the guest crystal, the anions are separated by the bulky $N(n-but)_4^+$ counter ions (29), whereas in the pure copper crystal they form linear stacks (3). If the guest molecules accept the host structure, as was concluded from ^{13}C ENDOR measurements (8), the anion is nearly planar and close to D_{2h} symmetry.

The echo-induced (field-swept) spectra show the resonance of only one molecule, in accord with the crystal structure, split by the interaction with the copper nuclear spin. The measured principal values of the g-tensor and the ^{63}Cu HFI tensor are listed in Table I. They are close to the room temperature values which were measured with CW EPR (1). The crystal was oriented in the axis system of the copper HFI-tensor using the field swept spectra. The copper HFI axis system is assumed to coincide with the molecular axis system ($A_1//X$, $A_2//Y$, $A_3//Z$, see I), following the findings of Maki et al (1). Because of the near-axiality of the g-tensor, the experimental error in the position of its in-plane axes is rather large and the angle of 35° between A_1 and g_1 has a large error.

Fig. 1a shows the experimental ESEEM spectra in the three measured planes. Every spectrum has peaks in the region below 1 MHz. Especially in the XY-plane these peaks don't fit the transitions of the cyanide nitrogen atoms. Therefore, they are thought to arise from the dipolar interaction between the unpaired electron and the nitrogen atoms of the $N(n-but)_4^+$ counterions. This Cu-N distance is 4.686 Å (in the host structure), almost 1 Å smaller than the distance between copper and the cyanide nitrogens.

TABLE 1

Experimental and calculated tensors in the axis system of A^{Cu} and in the molecular axis system, respectively, at a temperature of 30 K. (HFI and NQI in units of $10^{-4}cm^{-1}$).

		EXPERIMENTAL				CALCULATED			
		values	axis			values	axis		
			A_1	A_2	A_3		x	y	z
	g_1	2.018	35	55	91	2.021	1	90	91
	g_2	2.022	55	145	86	2.024	90	0	90
	g_3	2.086	92	86	5	2.079	89	90	1
^{63}Cu	A_1	40.2	0	90	90	39.4	14	76	89
	A_2	44.7	90	0	90	39.1	103	14	90
	A_3	-84.9	90	90	0	-78.5	90	90	1
	A_{iso}	-85.5				-11.9			
$^{14}N_1$	A_1	-0.106	34	111	65	-0.105	24	114	86
	A_2	-0.162	112	80	25	-0.161	89	80	11
	A_3	0.268	66	24	90	0.269	66	26	100
	A_{iso}	0.102				0.059			
$^{14}N_2$	A_1	-0.083	41	63	62	-0.091	21	70	87
	A_2	-0.157	116	100	27	-0.145	90	89	9
	A_3	0.240	61	151	86	0.239	69	157	108
	A_{iso}	0.077				0.058			
$^{14}N_1$	P_1	0.260	87	91	3	0.180	96	91	6
	P_2	0.349	62	28	91	0.269	58	32	86
	P_3	-0.609	28	118	93	-0.449	32	122	86
$^{14}N_2$	P_1	0.274	82	96	10	0.182	95	87	6
	P_2	0.368	57	145	110	0.267	60	149	85
	P_3	-0.642	34	56	93	-0.449	31	60	87

Another rather puzzling feature of the experimental spectra is the splitting which is observed on several peaks in the XY- and YZ-plane. The splittings vary between 40 and 80 kHz with a maximum at orientations of maximum angular dependence of the peak position. The nature of these splittings is not understood as will be discussed in the next section. In the fitting procedure of the tensors, the average frequency positions were used.

The frequencies of the peaks which are assigned to the cyanide nitrogens are plotted in Fig. 2. Assigning these frequencies to the right m_S-manifold of the right nitrogen atom is not straightforward. However, since all peaks (six for

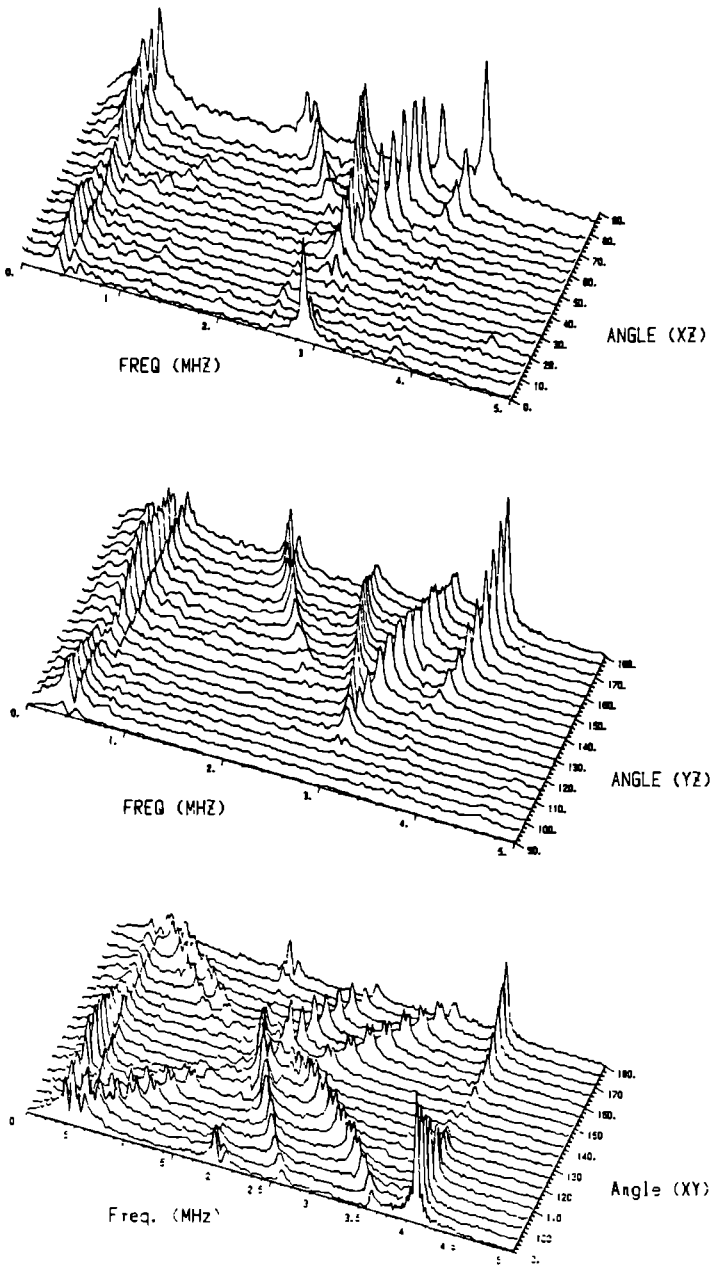

Figure 1a. Experimental FT-ESEEM spectra of $Cu/Ni(mnt)_2$ measured in three planes. Experimental data: Three-pulse echo; pulselength = 20 nsec; τ = 210 nsec; T is stepped from 0.80 to 26 35 μsec in steps of 50 nsec.

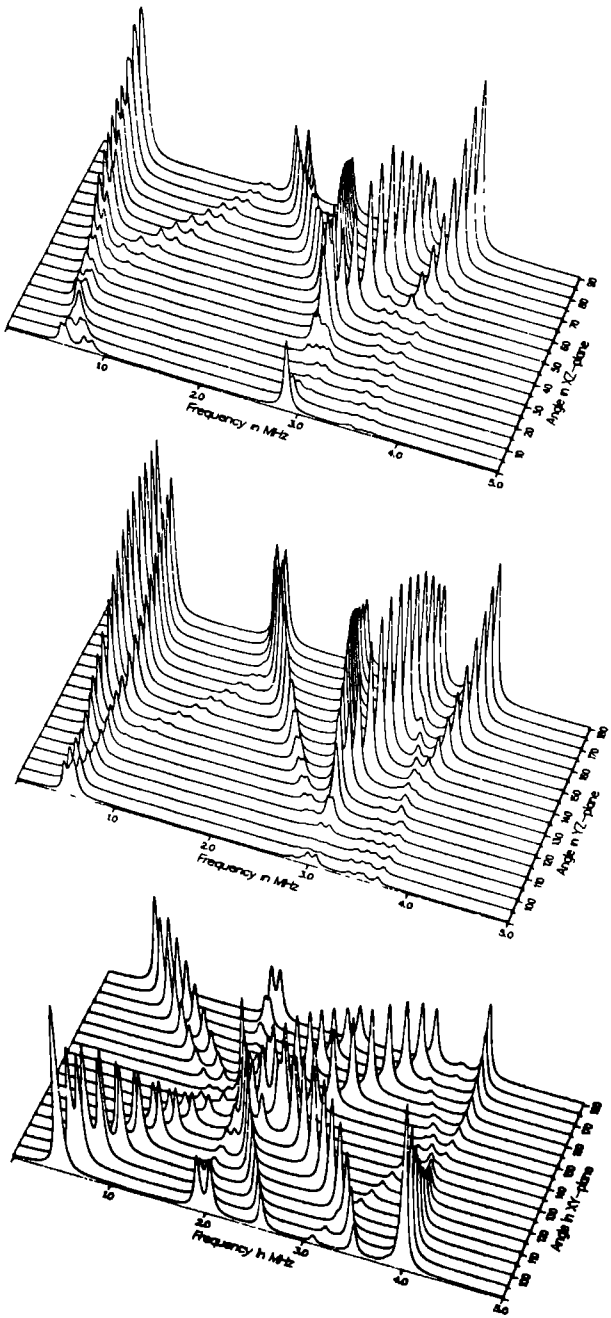

Figure 1b. Simulated FT-ESEEM spectra according to Hamiltonian (1) with $\tau = 210$ nsec.

each nitrogen atom because I=1) were observed, it was possible to select the three frequencies in one m_S-manifold by demanding that the sum of two of them equals the third (see fig. 3). These three transitions were used to determine the nitrogen HFI and NQI tensors in the following way: the transition frequencies were calculated with the spin Hamiltonian

$$\mathcal{H} = \mu_B \mathbf{B}\cdot\mathbf{g}\cdot\mathbf{S} + \mathbf{S}\cdot\mathbf{A}^{Cu}\cdot\mathbf{I}^{Cu} - g_{Cu}\mu_n \mathbf{B}\cdot\mathbf{I}^{Cu} \tag{1}$$

$$+ \mathbf{I}^N\cdot\mathbf{P}^N\cdot\mathbf{I}^N + \mathbf{S}\cdot\mathbf{A}^N\cdot\mathbf{I}^N - g_N\mu_n \mathbf{B}\cdot\mathbf{I}^N$$

and subsequently the error function

$$\sum_i (\nu^i_{obs} - \nu^i_{calc})^2 \tag{2}$$

was minimized by varying the elements of $\mathbf{P}^N$ and $\mathbf{A}^N$. In (2) the summation runs over the three assigned transitions at all orientations of the magnetic field in the three measured planes. After mimimization, the frequencies of the transitions in the other m_S-manifold could be calculated and compared with the experimental data. In this way, the frequencies of the two nitrogen atoms could be separated. In a second run the transition frequencies of both m_S-manifolds were included in the fit. The resulting principal values and the axes of the nitrogen tensors are listed in Table I. The (in absolute value) largest quadrupole interaction is in the direction of the C-N bond (deviation of ~ 3°) for both nitrogen atoms, the smallest principal value is perpendicular to the molecular plane. The asymmetry parameter η ($=|(P_1-P_2)/P_3|$) is ~ 0.15 and is equal for both atoms whereas the magnitude of the tensor elements differs by ~ 7%. The magnitude of the HFI is about 50% of the NQI. The isotropic contribution is one third of the largest anistropic principal value. The latter differs by about 10% for the two atoms and is located in the molecular plane, almost perpendicular to the C-N bond (~95°). The other two principal axes have no special orientations.

VI.4 Simulation of experimental spectra

The ESEEM spectra were simulated with the program MAGRES with the equations derived by Mims(17,18) for the stimulated echo sequence, in a generalized way:

Figure 2. Frequencies of ^{14}N-ESEEM modulations assigned to CN groeps; The numbering refers to the six level energy diagram of one electron spin coupled to a ^{14}N nuclear spin in figure 3. The fitted curves are indicated by the solid lines.

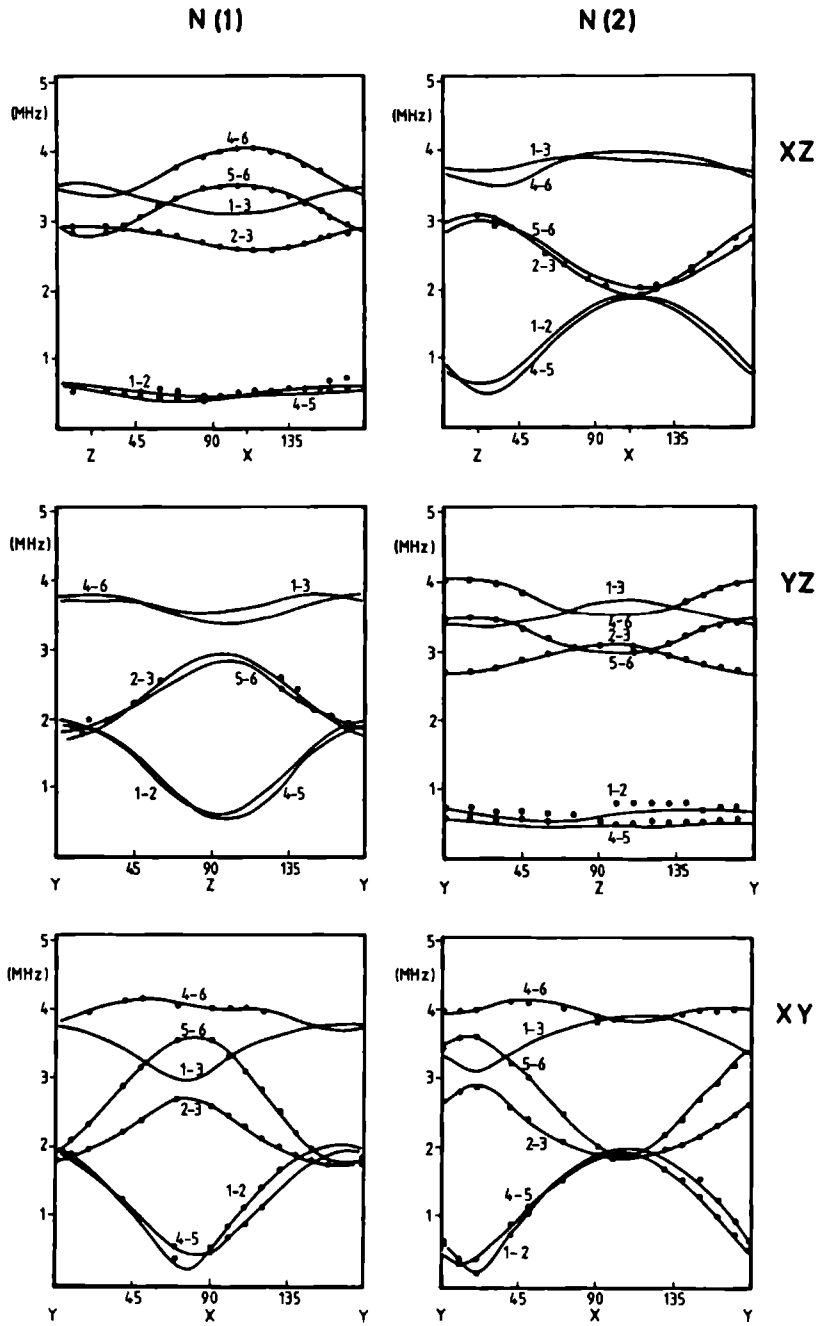
N (1)
N (2)
XZ
YZ
XY
(MHz)
4-6
5-6
1-3
2-3
1-2
4-5
Z
X
Y
45
90
135

$$P_{kn} = N\{\chi_{kn} + \sum_{i>j} 2\chi_{ij,kn}\cos(\omega_{ij}\tau)\} \quad (3)$$

where

$$\chi_{kn} = \sum_{i} |M_{ik}|^2 \, |M_{in}|^2$$

$$\chi_{ij,kn} = Re[M_{ik}^{*} M_{in} M_{jn}^{*} M_{jk}]$$

P_{kn} is the modulation intensity of NMR transition k-n and M_{ik} is the transition moment between states i and k of the spin system. The indices i,j,k,n run over all energy levels of the spin system. Inclusion of all four nitrogens in the spin Hamiltonian (1) would give rise to a dimensionality of 648 which is too large to be handled by the simulation program (it would take already 6.7 Mbyte to store the H-matrix). Therefore, only two inequivalent ^{14}N-nuclei were included. For τ the experimental value of 210 nsec was used.

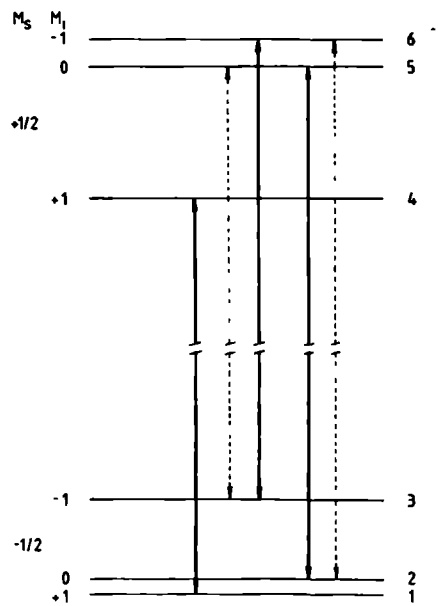

Figure 3. Energy level diagram for S=½ and ^{14}N nuclear spin I=1 with B_0 at an arbitrary orientation. The forbidden transitions are indicated with dotted lines.

The simulated spectra are presented in Fig. 1b. A comparison with the corresponding experimental spectra shows an excellent agreement in peak intensities and positions except for the splittings in transition 5-6 in the YZ-plane and especially in the transitions 1-2, 4-5, 5-6 in the XY plane. Also ESE-ENDOR studies on $Cu/Ni(mnt)_2$ oriented near the X-axis (an orientation were the ESEEM splittings were not resolved) showed splittings of 5 kHz (30)! Similar splittings were observed in ESEEM spectra of Cu bis(N,N di-n-butyldithiocarbamate), $Cu(but_2dtc)_2$ (22), and angular dependent line broadening was observed in CW-ENDOR spectra of Cu bis(dialkyldithiocarbamate), $Cu(R_2dtc)_2$, and bis(dialkyldiselenocarbamate) doped in the Zn and Ni hosts (26). Also in these two systems, the splitting/broadening was observed in those orientations where the lines have their maximum angular dependence. In order to investigate the possibility that these splittings are caused by second order interactions between the four nitrogen spins, simulated spectra were calculated without the copper spin but including all 4 nitrogen spins and their interactions according to Hamiltonian (1). (With the copper spin, the dimensionality of the problem is too large.) However, no evidence was found for splittings. Another possible cause would be a direct dipolar interaction between the cyanide N and a counter ion proton. Evaluation of this interaction at a distance of 2.5 0 yields a value of 1 kHz maximum, which is much too small to account for the observed splittings. Optical and EPR studies of $Cu/Ni(mnt)_2$ by Manoharan et al (31). suggested a change of crystal symmetry below 50 K giving rise to splittings in the EPR spectrum. In our studies no splitting in the EPR spectra could be observed. However, such a drastic effect would hardly explain the very small splittings in our ESEEM spectra which were temperature independent up to 70K. Still, these findings suggest the possibility of a break down of molecular inversion symmetry which would give rise to four inequivalent nitrogens. It is not clear, however, why similar effects were not observed in earlier ^1H and ^{13}C CW-ENDOR studies of the same compounds.

As was mentioned in the introduction, no good ^{14}N-CW-ENDOR spectra of this system could be obtained (8) as opposed to the system $Cu(dtc)_2$ where excellent line-intensities were observed (25,26). In order to check whether this is due to the different magnitude of the NQI and HFI, the nuclear spin transition probabilities of both complexes were calculated with the experimentally determined spin Hamiltonian parameters. Indeed the NMR transition moments of mnt were significantly lower than those of dtc (about a factor of three). Moreover, the number of "strong"-NMR transitions, i.e. with transition moments larger than 0.1×10^{-8}, was systematically lower in mnt (avarage of 3) than in dtc (average of 5). It is not sure, however, that this is the only reason for the weak ^{14}N-CW-ENDOR spectra of mnt, since dtc ENDOR transitions which were calculated to be "weak" could still be detected in many cases.

VI.5 Discussion

The g-tensor and the copper-HFI tensor agree with previous literature data (1,8). The nitrogen HFI and NQI tensors were not determined previously because the CW-ENDOR signals were too weak for a full rotational study (8). The nitrogen interactions were measured with ESEEM or CW-ENDOR in a series of $Cu(R_2dtc)_2$ (II) molecules in two different host crystals (26).

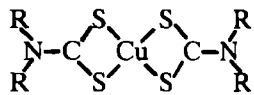

II

A comparison with the nitrogen tensors in the present system shows large differences:

1. In the present system the largest hyperfine and quadupole components are located in the molecular plane (parallel and perpendicular to the C-N bond respectively), whereas in the dithiocarbamate molecules they are perpendicular to the molecular plane.

2. In the $Cu(mnt)_2^{2-}$ molecule, the tensors are less axial, with asymmetry parameter 0.15 for the NQI and 0.21 and 0.31 for the HFI.

3. The NQI is ~ 30% larger than in the dtc-system

4. The isotropic HFI is a factor of three smaller whereas the anisotropic part of the HFI tensor is almost a factor of two larger than in $Cu(R_2dtc)_2$. This is very remarkable because the copper-nitrogen distance is much larger in the $Cu(mnt)_2^{2-}$ molecule, where nitrogen is located in the fourth coordination sphere whereas it is in the third one in $Cu(R_2dtc)_2$.

These differences suggest that the spin-density and electron-density distributions in the C-N and the $C-N(-C)_2^{2-}$ fragments in $Cu(mnt)_2^{2-}$ and $Cu(dtc)_2$ respectively, are very different. Several papers have been published with molecular orbital (MO) calculations on these molecules which results were, in turn, used for the computation of the spin Hamiltonian parameters. For both molecules, the calculations resulted in good fits of the g-tensor and the copper and sulfur HFI tensors. For $Cu(dtc)_2$, also ^1H, ^{13}C, and ^{14}N HFI tensors were calculated and compared with ENDOR and ESEEM experiments (22,32,33). For $Cu(mnt)_2^{2-}$ the ^{13}C-tensors were calculated in order to compare them with

ENDOR data. For this system, the ^{14}N interactions were not calculated and, therefore, in this paper we concentrate on the calculation of these interactions in order to compare them with the experimental tensors and for the comparison of the electronic structure around the nitrogen nuclei in $Cu(R_2dtc)_2$ and $Cu(mnt)_2^{2-}$. For the MO calculations, an extended Hückel method was used with the same empirical parameters as before (8,32). For the structure of the molecule, the structure of the host, nickel, crystal was used with two alterations:

1. The ligands were shifted over 0.06 $\AA$ along the x-axis which results in a copper-sulphur distance in between the metal-sulphur distances of the guest and the host molecules.

2. The computation of the nitrogen-interactions turned out to be very sensitive for the C-N bond-length and bond-direction. In the host crystal the bonds-lengths are different (1.130 and 1.147 $\AA$) and both bonds point at one side of the molecular plane (29). In the pure copper crystal the bond-lengths are equal (1.144 and 1.143 $\AA$) and one bond points above, the other below the plane (3). Therefore, the distances were adjusted to the C-N distances in the copper crystal whereas the directions were kept.

The picture that emerges from the calculations is that the unpaired electron is for about 50% centered in the d_{xy} orbital of the copper atom. The remaining 50% is delocalized to the four sulphur atoms. The spin-density on the remain-

TABLE 2

LCAO coefficients of nitrogen orbitals in the molecular orbital of the unpaired electron.

		$Cu(et_2dtc)_2$	$Cu(mnt)_2^{2-}$
N(1)	3s	-0.0001	0.0091
	$3p_x$	-0.0012	-0.0436
	$3p_y$	-0.0089	-0.0898
	$3p_z$	0.0016	0.0173
N(2)	3s		-0.0090
	$3p_x$		0.0370
	$3p_y$		-0.0871
	$3p_z$		-0.0144

ing ligand atoms is very small. In Table II we have listed the coefficients of the nitrogen orbitals together with coefficients in the $Cu(et_2dtc)_2$ molecule (32). At first sight it seems to be surprising that the spin density on nitrogen in the present system is larger, although the nitrogen atom is at a larger distance from the copper atom. However, in $Cu(R_2dtc)_2$ the nitrogen atom is located in a nodal plane of the B_{1g} MO (in the approximation of D_{2h} symmetry) and only the $2p_y$ orbital can have a spin density. But, the overlap with the sulphur orbitals is small and, hence, the mixing is small. In $Cu(mnt)_2^{2-}$ $2p_x$ and $2p_y$ of nitrogen can mix into the unpaired electron MO (also B_{1g} *in* D_{2h} symmetry) and the overlap with the sulphur orbitals is much more favourable.

The g-tensor, HFI- and NQI-tensors were calculated according to formulae which were published before (34). They are listed in Table I. The g-tensor and the copper HFI-tensor agree very well with the experimental results, proving that the calculated MO-energies and coefficients are reliable. For the calculation of the copper HFI, only one-center integrals (32) were included in both, first and second order contributions. This approximation is not allowed for the nitrogen HFI because it is to be expected that the multi-center integrals yield a sizeble contribution due to the fact that almost all of the spin density is located on copper and sulphur. The calculated second order contribution is small and, hence, multicenter integrals are calculated only in the first order contribution. This latter one is brought about by the electron spin nuclear spin dipole-dipole interaction (e.g. with nucleus N) and can be expressed (32) as

$$A_{ij}^N = \left(\frac{\mu_o}{4\pi}\right) g_e g_N \mu_b \mu_n \langle \psi_o | \frac{F_{ij}^N}{r_N^3} | \psi_o \rangle \qquad (4)$$

where μ_o is the permeability of free space, μ_b is the Bohr magneton, μ_n is the nuclear magneton, g_e the free-electron g-value and g_N the gyromagnetic ratio of nucleus N; i,j are x,y,z , F_{ij}^N is a component of a symmetrical traceless tensor operator related to the dipolar interaction and r_N is the electron-nucleus radius vector. If ψ_o, the MO of the unpaired electron, is expanded as a linear combination of atomic orbitals, ϕ_i^A, centered on nuclei A, then eq. (4) can be rewritten:

$$A_{ij}^N = \left(\frac{\mu_o}{4\pi}\right) g_e g_N \mu_b \mu_n \times \{ \sum_{i \in N} \sum_{j \in N} \langle C_i^N \phi_i^N | \frac{F_{ij}^N}{r_N^3} | C_j^N \phi_j^N \rangle$$

$$+ \sum_{A \neq N} \sum_{i \in A} \sum_{j \in A} \langle C_i^A \phi_i^A | \frac{F_{ij}^N}{r_N^3} | C_j^A \phi_j^A \rangle$$

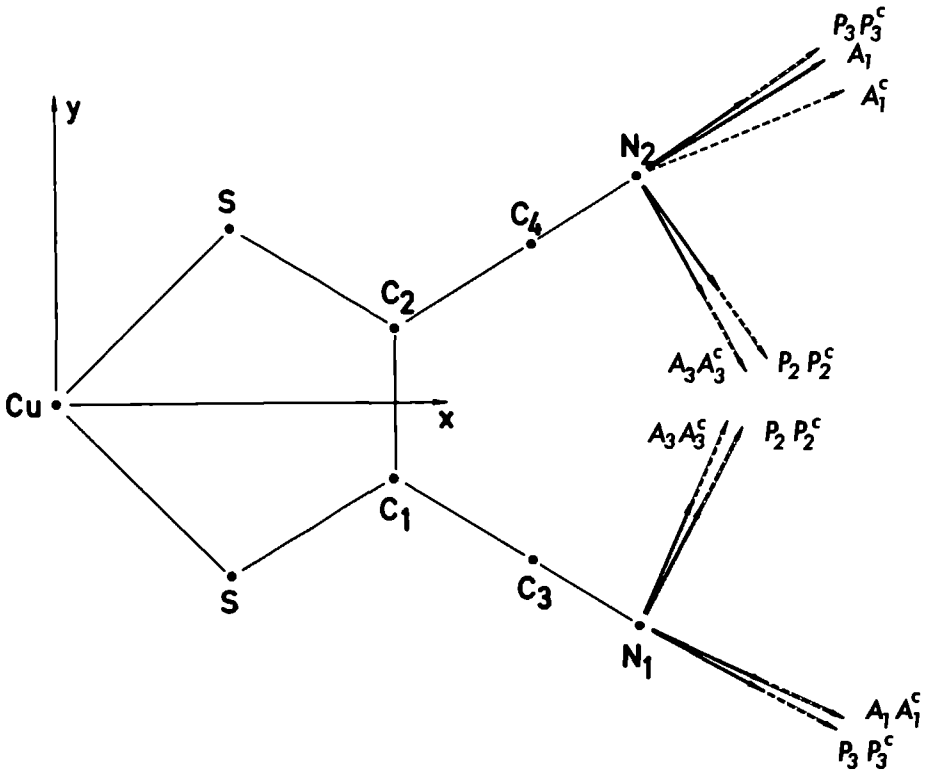

Figure 4. Orientation of the experimental (A, P) and the calculated (A^c, P^c) ^{14}N-tensors.

$$+ \sum_{A \neq N} \sum_{i \in A} \sum_{j \in N} \langle C_i^A \phi_i^A | \frac{F_{ij}^N}{r_N^3} | C_j^N \phi_j^N \rangle$$

$$+ \sum_{A \neq N} \sum_{B \neq N} \sum_{i \in A} \sum_{j \in B} \langle C_i^A \phi_i^A | \frac{F_{ij}^N}{r_N^3} | C_j^B \phi_j^B \rangle \}$$

$$= (A_{ij}^N)_1 + (A_{ij}^N)_{2,1} + (A_{ij}^N)_{2,2} + (A_{ij}^N)_3 \qquad (5)$$

where $(A_{ij}^N)_1$ and $(A_{ij}^N)_3$ are the one and three-center contributions respectively. $(A_{ij}^N)_{2,1}$ and $(A_{ij}^N)_{2,2}$ are two-centre contributions, $(A_{ij}^N)_{2,2}$ having one atomic or-

bital centered on nucleus N and $(A_{ij}^{N})_{2,1}$ having both orbitals centered on the same nucleus, not being N.

The multi center integrals were calculated form the MO coefficients by expanding each Slater type basis set orbital into five Gaussian type orbitals. Subsequently the integrals were calculated with the programme PROPERTY (32). In figure 4 the orientations of the calculated and the experimental ^{14}N-tensors are depicted. The numerical results of the calculations are listed in Table III together with the experimental values and with the corresponding data of $Cu(et_2dtc)_2$ (33). As might be expected on the basis of the LCAO coefficients in Table II, the calculated anisotropic and isotropic HFI is larger than in the calculated result for $Cu(et_2dtc)_2$. This is especially true if it is compared with

TABLE 3

Calculated one, two, and three center contributions to HFI tensors of ^{14}N in $Cu(mnt)_2^{2+}$ and $Cu(et_2dtc)_2$ and the experimentally determined tensors.

		1-center	2+3 center	1+2+3 center		experimental	
DTC-EH[1]							
	A_x	-0.01	0.05	0.04		0.06	
	A_y	0.02	-0.01	0.01		0.06	
	A_z	-0.01	-0.04	-0.05		-0.12	
	A_{iso}	0.0	0.0	0.0		-0.375	
DTC-UHFS[2]							
	A_x	0.08	0.05	0.13		0.06	
	A_y	0.16	-0.01	0.15		0.06	
	A_z	-0.24	-0.04	-0.28		-0.12	
	A_{iso}	-0.56	0.0	-0.56		-0.375	
MNT							
N(1)	A_1	-0.157	0.052	-0.105	(24,x)	-0.106	(34,x)
	A_2	-0.159	-0.003	-0.161	(11,z)	-0.162	(25,z)
	A_3	0.316	-0.049	0.269	(26,y)	0.268	(24,y)
	A_{iso}	0.042	0.017	0.059		0.102	
N(2)	A_1	-0.140	0.049	-0.091	(21,x)	-0.083	(41,x)
	A_2	-0.142	-0.004	-0.145	(9,z)	-0.157	(27,z)
	A_3	0.282	-0.045	0.239	(157,y)	0.240	(151,y)
	A_{iso}	0.041	0.017	0.058		0.077	

1) 1-center interaction calculated from Extended Huckel coefficients

2) 1-center interaction calculated from spin densities obtained with Unrestricted Hartree Fock Slater calculation[35].

the extended Hückel result of the latter molecule. The unrestricted Hartree Fock Slater method yielded a much larger HFI due to the inclusion of spin polarization effects. This effect is not expected to be significant for the nitrogen atoms in the present system because there is no nodal plane near these atoms. The multi-center integrals are not dominating but they are significant: ~ 20% of the largest 1-center principal value. The effect of the 2- and 3-center contribution is a reduction of (the absolute value of) A_1 and A_3, causing the calculated tensors to be non-axial, which is in agreement with the experiment. The total result for the anisotropic parts is equal to the experimental tensors, both in magnitude and direction, which result might be fortuitous on the basis of the very crude MO-method which is used. The calculated isotropic HFI is ~ 50% of the experimental value.

The calculated quadrupole tensors are listed in Table I. Taking into account the approximations in this calculation (34) (only one-center electric field gradient contributions, no lattice contribution) the result is satisfactory: the direction fits the experiment, the principal values are ~ 50% too large.

VI.6 Conclusions

1) The hyperfine and the quadrupole interaction could be measured very accurately, notwithstanding the fact that the spectra are very complicated due to the presence of two non-equivalent nitrogen atoms and the fact that the interactions are small (i.e. not larger than 2MHz).

2) The simulation of the ESEEM spectra is remarkebly good, considering the presence of two nitrogen spins and the suppression effect.

3) The observed splittings of the lines in certain directions of the magnetic field is not understood.

4) The MO calculation gives insight into the electronic structure of the molecule. The agreement between the calculated and the experimental tensors is very satisfactory, especially considering the approximate nature of the MO method.

Acknowledgement

The authors thank Professor E. de Boer for critically reading the manuscript and stimulating discussions.

References

1. A.H. Maki, N. Edelstein, A. Davison, and R.H. Holm, J. Am. Chem. Soc. *86*, 4580 (1964)
2. K.W. Plumlee, B.M. Hoffman, M.T. Ratjack, and C.R. Kannenwurf, Solid State Commun. *15*, 1651 (1974)
3. K.W. Plumlee, B.M. Hoffman, J.A. Ibers, and Z.G. Soos, J. Chem. Phys. *63*, 1926 (1975)
4. L.K. White and R.L. Belford, J. Am. Chem. Soc., *98*, 4428 (1976)
5. R. Kirmse, J. Stach, W. Dietzsch, and E. Hoyer, Inorg. Chim. Acta, *26*, L53 (1978)
6. M. Inone, K. Hiroyoshi, and D.J. Nakamusa, J. Magn. Reson. *33*, 409 (1979)
7. D. Snaathorst, H.M. Doesburg, J.A.A.J. Perenboom, and C.P. Keijzers Inorg. Chem. *20*, 2526 (1981)
8. R. Kirmse, J. Stach, U. Abram, W. Dietzsch, R. Böttcher, M.C.M Gribnau, and C.P. Keijzers, Inorg. Chem. *23*, 3333 (1984)
9. J. Stach, R. Kirmse, J. Sieler, U. Abram, W. Dietzsch, R. Böttcher, L.K. Hansen, H. Vergoossen, M.C.M. Gribnau, and C.P. Keijzers, Inorg. Chem. *25*, 1369 (1986)
10. L.V. Interrante, K.W. Browall, H.R. Hart Jr., I.S. Jacobs, B.D. Watkins, and S.H. Wee, J. Chem. Soc. *97*, 889, (1975)
11. R.D. Schmidt, R.M. Wing, and A.H. Maki, J. Am. Chem. Soc. *91*, 4391 (1969)
12. R.M. Wing and R.L. Schlupp, Inorg. Chem. *9*, 471 (1970)
13. P.T. Manoharan, J.H. Noordik, E. de Boer, and C.P. Keijzers, J. Chem. Phys. *74*, 1980 (1981)
14. J.G.M. van Rens, M.P.A. Viegers, and E. de Boer, Chem. Phys. Lett. *28*, 104 (1974)
15. R.L. Schlupp and A.H. Maki, Inorg. Chem. *13*, 44 (1974)
16. R. Kirmse, W. Dietzsch, J. Stach, L. Golic, R. Böttcher, W. Brunner, M.C.M. Gribnau, and C.P. Keijzers, Mol. Phys. *57*, 1139 (1986)

17. W.B. Mims, Phys. Rev. *B5*, 2409 (1972)

18. W.B. Mims, Phys. Rev. *B5*, 3543 (1972)

19. A.V. Astashkin, S.A. Dikanov, and Yu. D. Tsvetkov, Chem. Phys. Lett *122*, 259 (1985)

20. A. de Groot, R. Evenlo, and A.J. Hoff, J. Magn. Reson. *66*, 331 (1986)

21. E.J. Reijerse and C.P. Keijzers, J. Magn. Reson. accepted

22. E.J. Reijerse, M.L.H. Paulissen, and C.P. Keijzers, J. Magn. Reson. *60*, 66 (1984)

23. E.J. Reijerse, N.A.J.M. van Aerle, C.P. Keijzers, R. Böttcher, R. Kirmse, and J. Stach, J. Magn. Reson. *67*, 114 (1986)

24. R. Kirmse, U. Abram, and R. Böttcher, Chem. Phys. Lett. *88*, 98 (1982)

25. R. Kirmse, U. Abram, and R. Böttcher, Chem. Phys. Lett. *90*, 9 (1982)

26. R. Böttcher, R. Kirmse, J. Stach, E.J. Reijerse, and C.P. Keijzers, Chem. Phys. accepted.

27. L.K. White and R.L. Belford, J. Am. Chem. Soc. *98* 4428 (1976)

28. A. Davidson and R.H. Holm, Inorg. Synth. *10*, 8 (1971)

29. A. Kobayashi and Y. Sasaki, Bull. Chem. Soc. Jpn. *50*, 2650 (1977)

30. E.J. Reijerse and A.A.K. Klaassen, Rev. Sci. Instrum. in press.

31. P.T. Manoharan and G.V.R. Chandramouli, personal communication.

32. C.P. Keijzers and D. Snaathorst, Chem. Phys. Lett. *69*, 348 (1980)

33. D. Snaathorst, C.P. Keijzers, A.A.K. Klaassen, E. de Boer, V.P. Chacko, and R. Gomperts, Mol. Phys. *40*, 585 (1980)

34. C.P. Keijzers and E. de Boer, Mol. Phys. *29*, 1007 (1975)

35. P.J.M. Geurts, P.C.P. Bouten, and A. van der Avoird, J. Chem. Phys. *73*, 1306 (1980)

CHAPTER VII[†]

Model calculations of frequency domain ESEEM spectra of disordered systems

E.J. REIJERSE AND C.P. KEIJZERS

Department of Molecular Spectroscopy,
Research Institute of Materials, University of Nijmegen
Toernooiveld, 6525 ED Nijmegen, The Netherlands.

Model calculations were carried out for Electron Spin Echo Envelope Modulation (ESEEM), ENDOR and pulsed ENDOR spectra of spin systems of one electron coupled with a I=1/2, I=1 or a I=3/2 nucleus. On the basis of these simulations predictions are made for which cases resolved powder patterns can be expected. In the I=1/2 case it is demonstrated that in the ESEEM simulations a degradation of the powder lineshape occurs as compared to the ENDOR simulations. Nevertheless, the shape and the symmetry of the bands may give information about the relative sign of the isotropic and the anisotropic hyperfine interaction and may yield an estimate for the magnitude of the hyperfine interaction. In the I=1 case, the pure quadrupole frequencies can be observed when the nuclear Zeeman interaction is approximately compensated by the isotropic hyperfine interaction in one m_s-manifold. This limitation is much more strict if I=3/2. For this nuclear spin the spectra are extremely complicated and virtually no information can be obtained if this "compensation restriction" is not fulfilled.

[†] Appearing in "The Journal of Magnetic Resonance"

VII.1 Introduction

The great power of Electron Spin Echo Envelope Modulation (ESEEM) spectroscopy has been demonstrated in several studies of weakly coupled nuclei with a small magnetic moment in single crystals (1-4) and powders (5,6). In these cases one has to deal with low-frequency nuclear spin-transitions which are not easily accessible with the conventional CW-ENDOR techniques although spectacular improvements have been accomplished in this field (7-10). ESEEM has important advantages over CW-ENDOR:

a. The modulation effect does not depend on a balance of relaxation times.
b. Very low frequency modulations can be observed.
c. The signal to noise ratio does not depend on the frequency.
d. The modulation intensity can be calculated directly from the spin-hamiltonian because it is not influenced by relaxation effects (11).
e. With 2D techniques it is possible to obtain information about the assignment of spectral lines in case of single crystals (3,12).

On the other hand, the modulation effect is strongly dependent on the existence of anisotropic interactions which must not differ more than an order of magnitude from the nuclear Zeeman interaction (NZI). Therefore, the modulation effect will be weaker than the ENDOR effect in case of predominantly isotropic interactions as, for instance, for weakly coupled protons.

The application of ESEEM spectroscopy to disordered systems still suffers from some difficulties:

a. The anisotropic broadening results in destructive interference which makes the modulations disappear very fast from the echo-envelope. Therefore, the instrumental dead time is a serious limiting factor.
b. The analysis of frequency domain spectra is not straightforward due to the extreme angular dependence of the modulation intensity.

One way of analyzing the ESEEM spectra is to fit the time domain to a model function based on the spin hamiltonian (13-15). Impressive results have been accomplished this way for systems with an isotropic g tensor (6). However, in case of quadrupole nuclei, this procedure is limited to systems where a perturbation treatment of the nuclear quadrupole interaction (NQI) is allowed. Moreover, the hyperfine interaction (HFI) is always approximated as a (pseudo)-dipolar (hence axial) interaction. These approximations are inevitable if a complete diagonalisation of the spin hamiltonian matrix would take too much computer time in a fit procedure, as for instance in case there are interactions with several nuclei. Therefore, a reliable method of visual analysis could be important in deciding whether certain approximations are justified and in order to infer good starting values for a fit procedure. Moreover, it may render a computer analysis superfluous.

Obviously, the spectral data is better accessible for visual analysis in the frequency domain than in the original time domain and recent model calculations for spin systems S=1/2, I=1/2 (16,17) and S=1, I=1/2 (17) show that use-

ful information can indeed be obtained from ESEEM spectra in the frequency domain. Unlike ENDOR-powder spectra of systems with isotropic g, where the lineshape is determined by the statistical weight of orientations, the FT-ESEEM spectra show little structure due to the angular dependence of the modulation intensity which is at a minimum at the edges of the powder pattern. De Groot et al. (17) investigated under which limiting values of the hyperfine interaction, the isotropic hyperfine value can be determined reliably.

In this communication these studies are extended to the question which information concerning the symmetry and the magnitude of the anisotropic part of the HFI may be extracted from the powder lineshape itself. Also simulations are presented of the system S=1/2, I=1 and S=1/2, I=3/2 with HFI and NQI of arbitrary symmetry and orientation.

VII.2 Calculation Procedure

The computer program MAGRES calculates (EPR and NMR) transition frequencies and probabilities for any spin-system (for applications of the program see for instance (18,19)) by diagonalisation of the spin hamiltonian matrix. Also the calculation of powder spectra is possible, although the necessary computer time increases rapidly with increasing dimensionality of the spin system. To this program a series of subroutines was added to calculate the ESEEM and ENDOR spectra. They were used together with a minimazation program, for the derivation of HFI and NQI tensors of ^{14}N from single crystal experiments (2) and for a comparison of ESEEM, CW-ENDOR and pulsed ENDOR of the same system (5). The model calculations in this paper are restricted to isotropic electron and nuclear Zeeman interactions (although the program allows any g and σ tensors) and to the interaction with only one nucleus (the program allows any number of nuclei but the computer time increases drastically). The resulting spin hamiltonian, with the magnetic field, B_0, along Z is, therefore:

$$H = g\mu_B B_0 S_z - g_N \mu_N B_0 I_z + \mathbf{S}\cdot\mathbf{A}\cdot\mathbf{I} + \mathbf{I}\cdot\mathbf{P}\cdot\mathbf{I} \qquad [1]$$

where **A** consists of the isotropic contribution "a_{iso}" and the traceless tensor **T**. The NQI tensor, **P**, is traceless by definition. For the calculation of the powder spectrum, the direction of B_0 is varied over half a unit sphere. The number of directions depends on the system but is typically 2000. After the exact calculation of the energies and eigenfunctions for a direction of B_0, the three-pulse modulations were calculated with the relations derived by W.B. Mims (11) in a generalized way (5):

$$P_{kn} = N\{\chi_{kn} + \sum_{i>j} 2\chi_{ij,kn}\cos(\omega_{ij}\tau)\} \quad [2]$$

where

$$\chi_{kn} = \sum_{i} |M_{ik}|^2 \, |M_{in}|^2$$

$$\chi_{ij,kn} = Re[M_{ik}^{*} M_{in} M_{jn}^{*} M_{jk}]$$

P_{kn} is the modulation intensity of NMR transition k-n and M_{ik} is the transition moment between states i and k of the spin system. The indices i,j,k,n run over all energy levels of the spin system. The 3-pulse suppression effect is not taken into account in order to obtain a picture as general as possible. The simulated spectra are comparable with 3-pulse modulation experiments which would be integrated over time τ i.e. the $\cos(\omega_{ij}\tau)$ terms disappear from [2]. In all simulations the NZI frequency, ν_n, was taken as unity (1 MHz). The simulations can be applied to other nuclei by scaling all interactions (HFI and NQI) in units of ν_n.

In the present spin systems the difference in ENDOR transition probability of the low and high frequency components is about an order of magnitude as a consequence of the hyperfine (de)enhancement. This implies that the low frequency component of the calculated ENDOR spectra would be reduced beyond visibility. In order to facilitate comparison of the lineshapes in ENDOR and ESEEM spectra, this hyperfine (de)enhancement effect was excluded by omitting the term $\mu_b \mathbf{B}_1 \cdot \mathbf{g} \cdot \mathbf{S}$ from the perturbation hamiltonian. Thus, the ENDOR spectra were calculated as the NMR transition moments $g_n \mu_n <\psi_i | \mathbf{B}_1 \cdot \mathbf{I} | \psi_j>$. The concequence of this procedure is that the calculated intensities cannot be compared with experimental spectra. However, since all relaxation mechanisms that are necessary to observe ENDOR are excluded as well, comparison of the calculated ENDOR intensities with experimental ones would not be possible anyway. Nevertheless, these spectra still serve our purpose, i.e. comparison of line-shapes rather than line-intensities.

For all spectra, the calculated lines were convoluted with a Gaussian line of 10 kHz half-width.

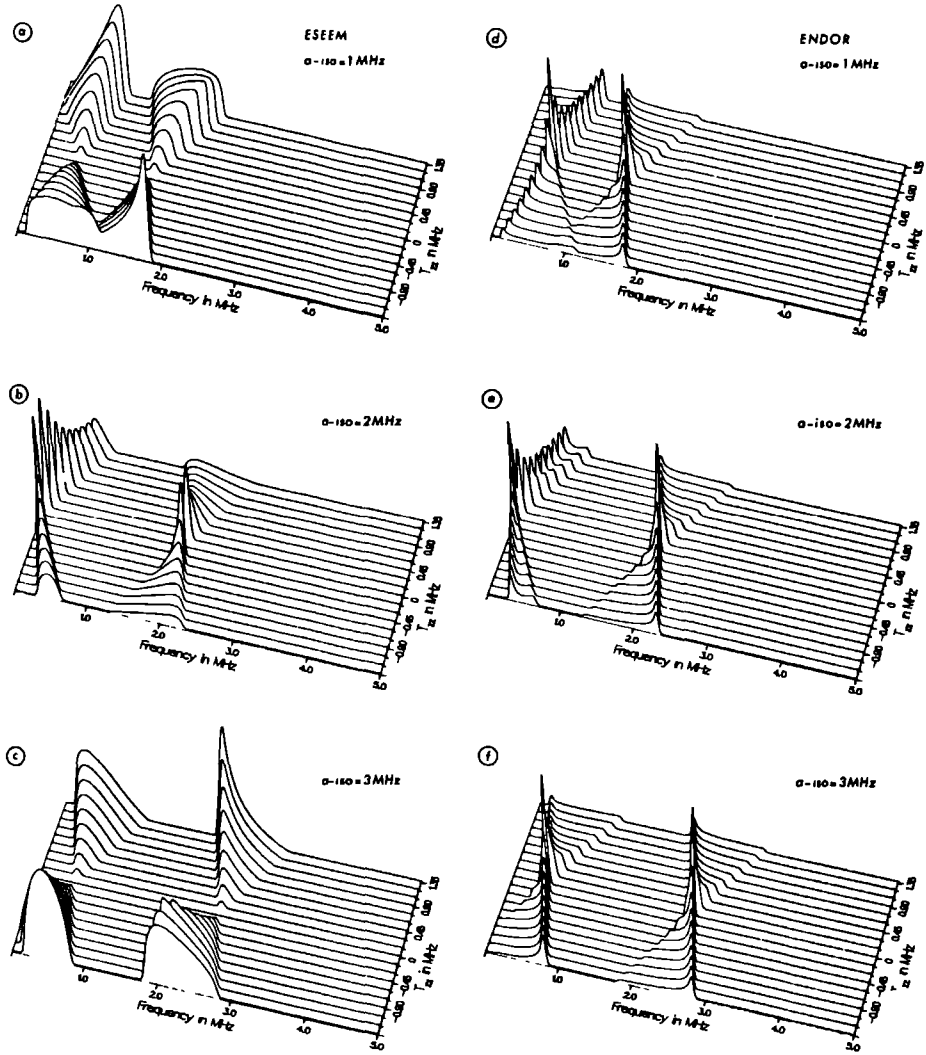

Figure 1. ESEEM (a-c) and ENDOR (d-f) simulations for S=1/2 and I=1/2 spin systems. Nuclear zeeman frequency ν_n = 1 MHz; isotropic hyperfine interaction: a_{iso} = 1 MHz (a,d); 2 MHz (b,e) and 3 MHz (c,f) respectively. The (axial) anisotropic hyperfine contribution is varied.

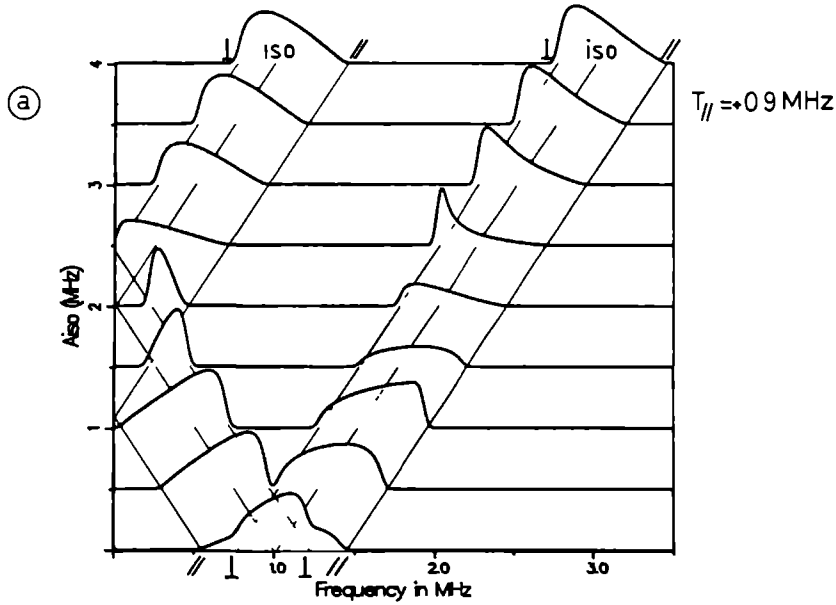
a
ISO
ISO
$T_{//}$ =+0.9 MHz
Aiso (MHz)
Frequency in MHz

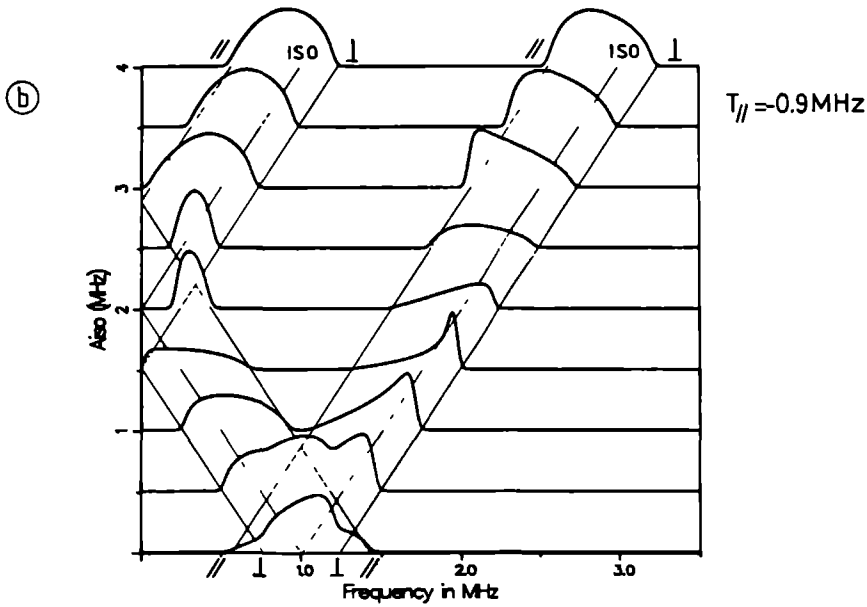
b
ISO
ISO
$T_{//}$ =-0.9 MHz
Aiso (MHz)
Frequency in MHz

VII.3 Calculated Spectra

The simplest case: S=1/2, I=1/2

In figure 1 ENDOR and "suppression free" (see above) three-pulse ESEEM simulations are presented for an axially symmetric HFI tensor with a_{iso} = 1,2 and 3 MHz and $T_{//}$ varying from -1.35 to +1.35 MHz. The ENDOR spectra reflect the statistical weight of orientations: the maximum intensity is obtained for $\nu_{\perp}^{\pm} = |\nu_n \pm \frac{1}{2}A_{\perp}|$ (in first order). The ESEEM spectra have a completely different intensity pattern. This is caused by the strong angular dependence of the modulation depth: it is minimal at canonical orientations whereas the modulation intensity is strong for orientations close to the magic angle where the secular part of the anisotropic HFI is zero and, hence, the mixing of the spin functions by the non-secular term is maximal (16). Therefore, in first order the maximum intensities are expected for the frequencies $\nu = |\nu_n \pm \frac{1}{2}a_{iso}|$. It is worth noting that in the case $\nu_n \pm \frac{1}{2}a_{iso}| = 0$ i.e. $a_{iso}=2$ MHz, the ESEEM powder patterns are comparible to the ENDOR patterns with a maximum intensity near $\nu_{\perp}^{\pm}$. In the other two cases the position of the maximum intensity depends on the sign of $T_{//}$. This is clarified in figure 2 where for a constant anisotropy ($T_{//}=+-0.90MHz$) the a_{iso}-dependence is depicted. For both signs of $T_{//}$ the a_{iso}-dependence starts at $a_{iso}=0$ with a structureless bump at ν_n. The lineshapes of both frequency components are asymmetric for most values of a_{iso}. The maximum intensity in the low frequency component varies between the isotropic position and the position of $\nu_{\perp}^{-}$, hence between the isotropic position and the position of the maximum that is observed in ENDOR. This is not true, however, for the case $T_{//}<0$, $a_{iso} \geq 2\nu_n$. In that region, the low frequency line is almost symmetric and the maximum intensity is between the isotropic position and $\nu_{//}^{-} = |\nu_n - \frac{1}{2}A_{//}|$! The position of the maximum intensity in the high frequency band is either at the perpendicular or at the parallel frequency, depending on the sign of $T_{//}$ and on the sign of $(a_{iso}-2\nu_n)$. For values of a_{iso} close to $2\nu_n$, the low frequency band is symmetric, with the maximum intensity between the parallel and the perpendicular position, and the position of the maximum in the high frequency band can change drastically with small changes in a_{iso}. For large values of a_{iso} (as compared to $|T_{//}|$) both bands become symmetric and centered at the isotropic positions (not shown). With respect to the analysis of experimental spectra, the following conclusions can be drawn:

Figure 2 ESEEM simulations showing the powder lineshape as a function of the isotropic hyperfine interaction for a fixed (axial) anisotropic hyperfine contribution (a) T_{zz} = +0 9 MHz, (b) T_{zz} = -0 9 MHz To facilitate comparison of the lineshapes the simulations were normalized to the same maximum intensity. The dashed lines indicated with "$\perp$" and "//" reflect the linepositions of single crystal spectra i e $|\nu_n \pm \frac{1}{2}A_{//}|$ and $|\nu_n \pm \frac{1}{2}A_{\perp}|$ respectively

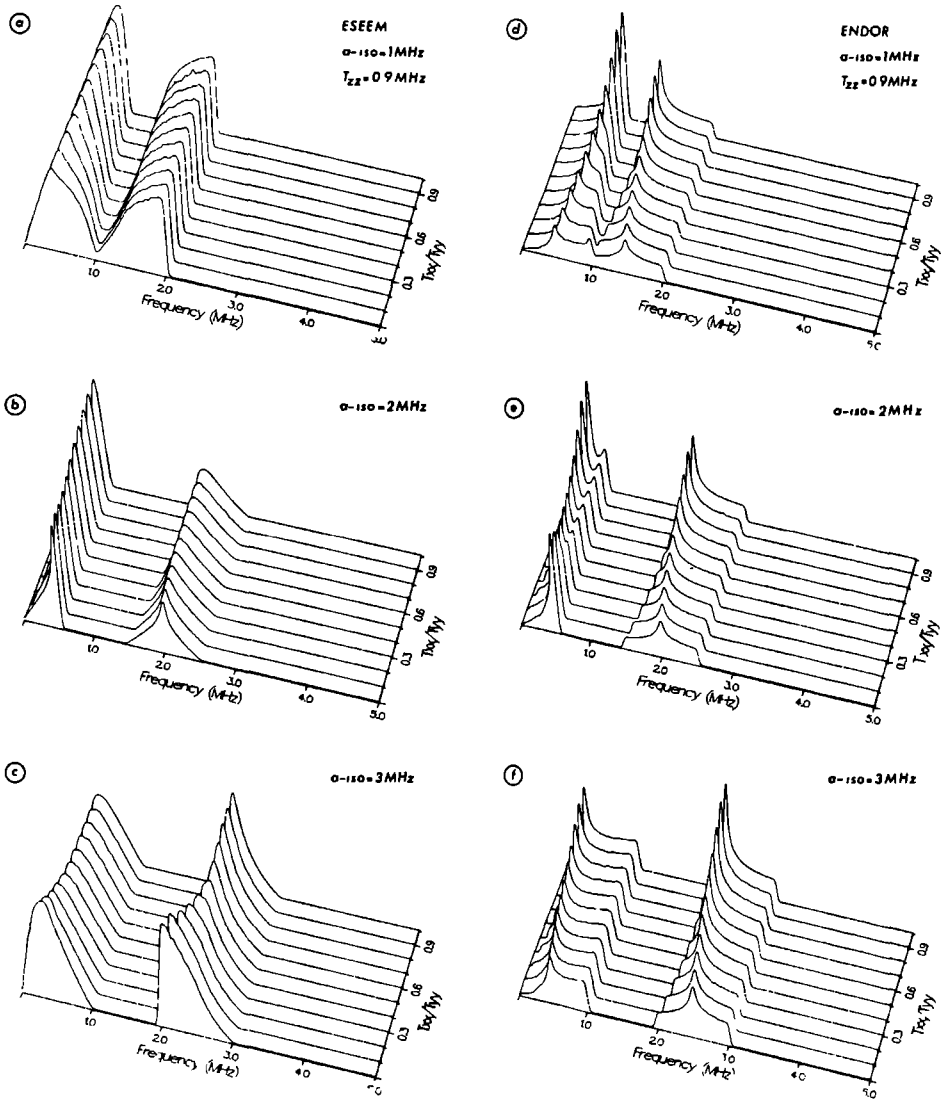

Figure 3. ESEEM (a-c) and ENDOR (d-f) simulations for S=1/2 and I=1/2 spin systems with the same isotropic parameters as in figure 1. For a fixed T_{zz}-value the asymmetry of the hyperfine interaction (T_{xx}/T_{yy}) is varied.

a. If the observed lines are symmetric, then $|T_{//}| << |\nu_n \pm \frac{1}{2}a_{iso}|$ and the spectrum is similar to an isotropic, first order ENDOR spectrum.
b. If only the high-frequency band can be observed, no conclusion can be drawn about the relative sign of a_{iso} and $T_{//}$
c. From the position of the high frequency band, $|a_{iso}|$ can be roughly determined (figure 2).
d. Even if the high and the low frequency band can be measured, the determination of the relative sign of a_{iso} and $T_{//}$ will be very difficult in the regime of $|a_{iso}| > 2\nu_n$, although a large asymmetry in the low symmetry band would indicate equal signs for a_{iso} and $T_{//}$.
e. In the regime $|a_{iso}| < 2\nu_n$, the relative signs of a_{iso} and $T_{//}$ can be determined readily provided that both frequency bands can be observed.
f. In most cases the ESEEM powder lineshapes are not sensitive to deviations of the axiality of the hyperfine tensor. This must be concluded from the simulations in figure 3 where the T-tensor is varied from axial ($T_{xx} = T_{yy} = -\frac{1}{2}T_{zz}$) to completely non-axial ($T_{xx} = 0$, $T_{yy} = -T_{zz}$), for a T_{zz} value of 0.9 MHz (the same value as in figure 2). Only in the very rare case $a_{iso} = 2\nu_n$ the powder lineshapes reflect the statistical weight of orientations as in ENDOR.

It seems, therefore, that although generally the exact values of $T_{//}$ and $T_{\perp}$ cannot be determined from the Fourier transformed ESEEM spectra as was concluded by de Groot et al. (17), in some cases (d,e) the shape and symmetry of the observed bands may give information about the relative sign of a_{iso} and $T_{//}$ and possibly yield an estimate of $T_{//}$ and $T_{\perp}$.

The case S=1/2, I=1

In the case I=1 with a NQI of the same order of magnitude as the NZI, the ESEEM and ENDOR spectra are completely broadened unless the NZI is (partly) compensated for in one m_S-manifold by the isotropic HFI (20). In this case the pure quadrupole frequencies are obtained. This is illustrated in figure 4a, where "suppression free" three-pulse ESEEM powder spectra are simulated using the simulation equations [2] with the following spin hamiltonian:

$$H = g\mu_B B_0 S_z - g_N \mu_N B_0 I_z + \mathbf{S}\cdot\mathbf{A}\cdot\mathbf{I} + K[3I_z^2 - I^2 + \eta(I_x^2 - I_y^2)] \qquad [3]$$

where quadrupole parameters K and η have their usual meaning. Quadrupole parameters in the order of K=0.4 MHz and η=0.5 are encountered frequently in ^{14}N-coordinated paramagnetic species in biological systems (21,22). Figure 4a shows that at the "compensation point" $|\nu_n \pm \frac{1}{2}a_{iso}| = 0$, sharp peaks emerge (from the manifold $m_S = +\frac{1}{2}$ for $a_{iso} > 0$) at the quadrupole frequencies (hamiltonian [3] without HFI and NZI):

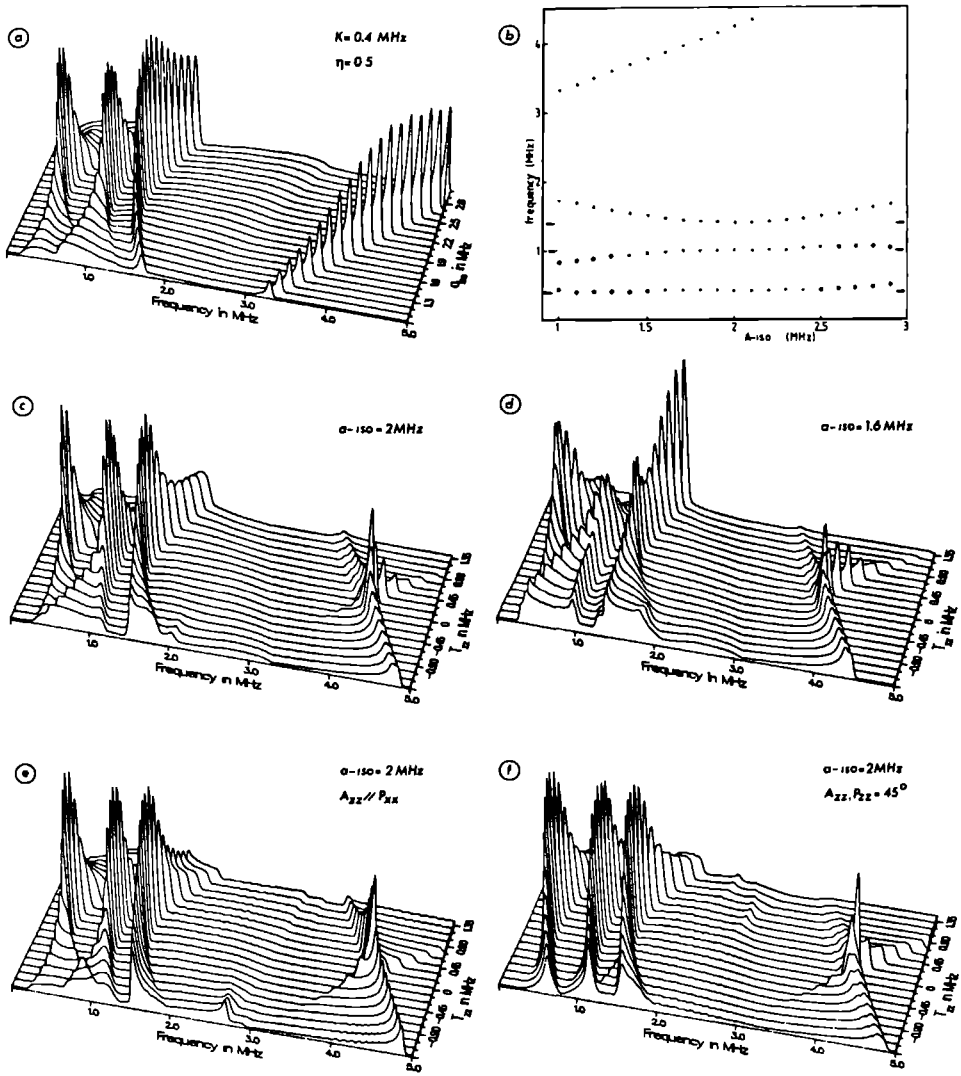

Figure 4. ESEEM simulations of S=1/2 and I=1 spin system with ν_n = 1 MHz; K = 0.4 MHz and η = 0.5. (a) The isotropic hyperfine interaction is varied. The anisotropic interaction is zero. (b) Graph of peak positions according to simulations in (a). The arrows indicate the quadrupole frequencies, eq. [4]. (c,d) Anisotropic hyperfine contribution is varied and a_{iso} is fixed at 2 MHz (c) or 1.6 MHz (d). (e) Same simulations as in (c) but with A_{zz} alligned along the x-axis of the quadrupole tensor. (f) same ESEEM simulations as in (e) but with A_{zz} making an angle of 45° in the XZ-plane of the quadrupole tensor.

$$\nu_+ = K(3+\eta), \quad \nu_- = K(3-\eta), \quad \nu_0 = 2K\eta. \qquad [4]$$

The graph of the peakpositions in figure 4b indicates that in order to obtain the quadrupole frequencies within 10% accuracy, $|\nu_n - \frac{1}{2}a_{iso}|$ should not exeed 25% of ν_n. The high frequency component from the manifold $m_S = -\frac{1}{2}$ can be used as a check for the correctness of the approximation since it reflects the frequency $2\nu_m$ where

$$\nu_m = [\nu_{eff}^2 + K^2(3+\eta^2)]^{1/2} \approx \nu_{eff} \textit{ in this case} \qquad [5]$$

$$\nu_{eff} = |\nu_n + \tfrac{1}{2}a_{iso}|$$

Figures 4c-f show the effect of the introduction of an anisotropic HFI of axial symmetry at arbitrary orientations. According to the simulations 4c-d the high-frequency component has its highest intensity near $2|\nu_n + \frac{1}{2}a_{iso} + \frac{1}{2}T_\perp|$. In combination with anisotropic hyperfine interactions of arbitrary orientation, intense low frequency components may arise which yield unreliable quadrupole values. Therefore, it appears that the high-frequency component plays an important role in deciding whether the "compensation- approximation" is valid: In the ideal case one expects three low-frequency components with a sum relation ($\nu_- + \nu_0 = \nu_+$) and a high frequency component at $2\nu_m$.

The case S=1/2, I=3/2

In figure 5 simulations are shown for the case of a I=3/2 nucleus (ν_n = 1*MHz*, K=0.4 MHz and η=0.5). It seems that this case needs a very tight "compensation restriction" in order to produce detectable ESEEM signals at the quadrupole frequency. A sharp peak is observed at this frequency $\nu_q = 6K(1+\eta^2/3)^{1/2} = 2.50$ MHz only when $\nu_n - \frac{1}{2}a_{iso}$ is less then 10% of ν_n in the rare case that T_{zz} is zero. In the cases that T_{zz} is nonzero, the intensity reduces rapidly for increasing values of T_{zz}, especially in the case $\frac{1}{2}a_{iso} = \nu_n$ (fig. 5c). For other values of a_{iso} (fig. 5 b,d) the intensity for $T_{zz}=0$ is lower and it almost doesn't increase for finite values of T_{zz}. Only for $\frac{1}{2}(a_{iso} + T_{zz}) \approx \nu_n$ an intense peak emerges at very low frequency. The resulting spectra for finite values of T_{zz} are quite complicated and it must be considered to be extremely

Figure 5 (next page). ESEEM simulations for S=1/2 and I=3/2 systems with ν_n = 1 MHz, K=0 4 MHz and η = 0 5. (a) Zero anisotropic hyperfine interaction, varying isotropic hyperfine interaction In (b-d) the (axial) anisotropic hyperfine interaction is varied and the isotropic interaction is fixed (b) a_{iso} = +1 6 MHz, (c) a_{iso} = +2 0 MHz, (d) a_{iso} = +2 4 MHz The intensities in b-d are scaled to the same maximum value Their relative intensities can be judged by comparison of the T_{zz} = 0 spectra with the corresponding spectra in (a)

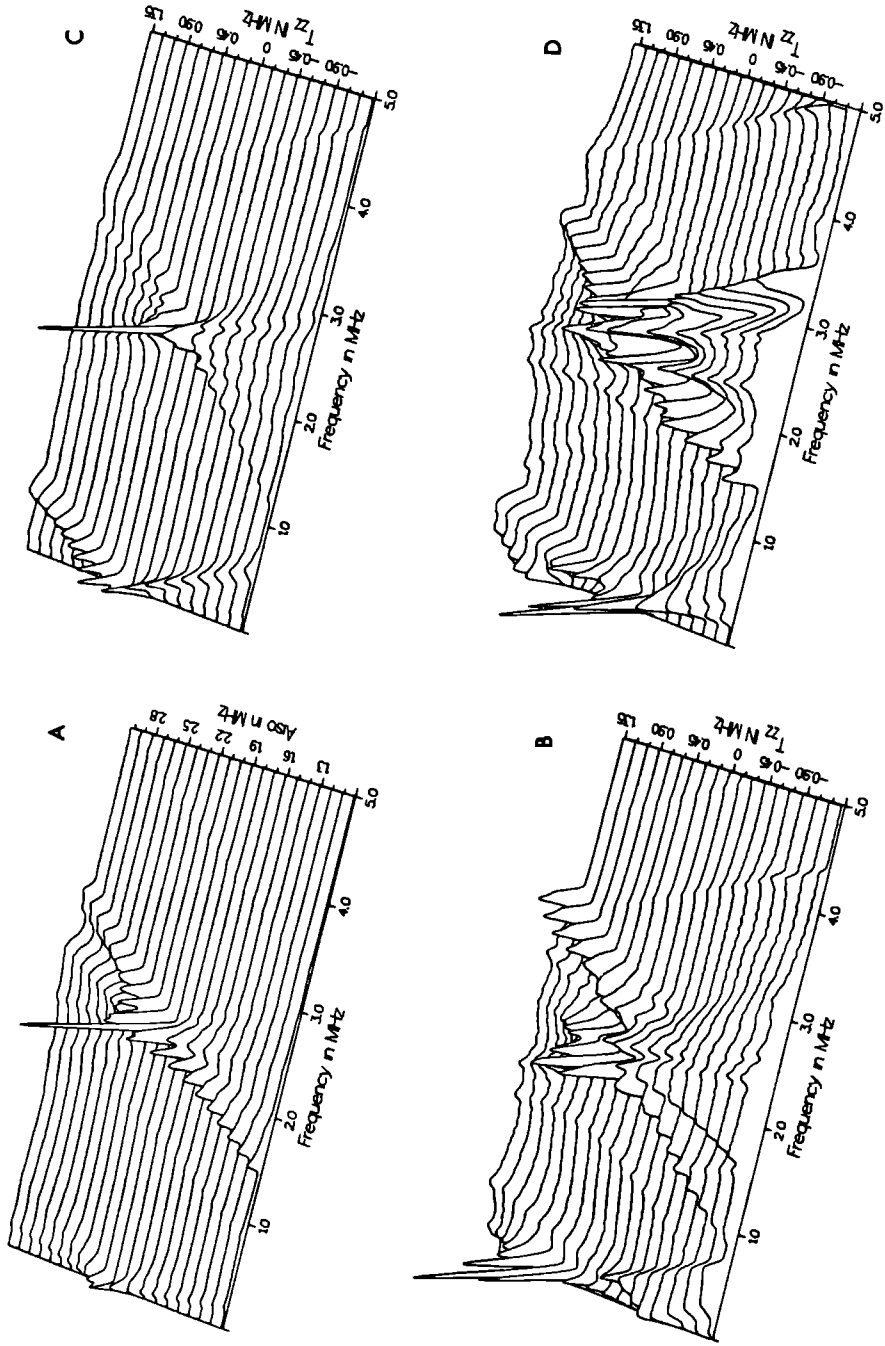
A
Abs n MHz
1.2
1.5
1.9
2.2
2.5
2.8
Frequency n MHz
1.0
2.0
3.0
4.0
5.0
B
Tzz N MHz
-1.35
-0.90
-0.45
0
0.45
0.90
1.35
Frequency n MHz
1.0
2.0
3.0
4.0
5.0
C
Tzz N MHz
-1.35
-0.90
-0.45
0
0.45
0.90
1.35
Frequency n MHz
1.0
2.0
3.0
4.0
5.0
D
Tzz N MHz
-1.35
-0.90
-0.45
0
0.45
0.90
1.35
Frequency n MHz
1.0
2.0
3.0
4.0
5.0

difficult to extract direct information from them about the magnitude of hyperfine and quadrupole interaction. Therefore, we may safely conclude that for nuclei like Na, K and Al it is virtually impossible to detect pure quadrupole frequencies with ESEEM or ENDOR in a disordered system.

VII.4 Conclusions

a. Despite the degradation of the powder lineshapes in ESEEM, as compared to ENDOR for a I=1/2 system it is worthwhile to continue the efforts to obtain reliable FT-ESEEM spectra by improving the experimental and the data-analysis techniques, since ESEEM lineshapes still contain useful information in case of axial hyperfine interaction.

b. In the case of I=1 nuclei there is a fair chance to obtain resolved powder ESEEM spectra since the "compensation restriction" is rather mild (as opposed to higher nuclear spin states) i.e. $|\nu_n \pm \frac{1}{2}a| < 25\% \times \nu_n$. The high frequency component gives the necessary information about the validity of this restriction.

c. For I=3/2 the spectra are extremely complicated and virtually no information can be obtained, unless the compensation restriction is fulfilled: $|\nu_n \pm \frac{1}{2}a| < 10\% \times \nu_n$.

Acknowledgement

We thank Professor Dr. E. de Boer for his incisive critical comments and his continuous interest in our work.

References

1. J. Isoya, M.K. Bowman, J.R. Norris, and J.A. Weil, J. Chem. Phys. *78*, 1735 (1983).
2. E.J. Reijerse, M.L.H. Paulissen, and C.P. Keijzers, J. Magn. Reson. *60*, 66 (1984).
3. H. Barkhuijsen, R. de Beer, A.F. Deutz, D. van Ormondt, and G. Völkel, Solid State Commun. *49*, 679 (1984).
4. D.J. Single, W.A.J.A. van de Poel, J. Schmidt, J.H. van der Waals, and R. de Beer, J. Chem. Phys. *81*, 5453 (1984).

E.J. Reijerse, N.A.J.M. van Aerle, C.P. Keijzers, R. Böttcher, R. Kirmse and J. Stach, J. Magn. Reson. *67*, 114 (1986)

6. L. Kevan in "Time Domain Electron Paramagnetic Resonance" (Eds, L. Kevan and R.N. Schwartz, John Wiley, New York, 1979), Chap. 8.
7. R. Kirmse, U. Abram, and R. Böttcher, Chem. Phys. Lett. *90*, 9 (1982)
8. R. Kirmse, J. Stach, U. Abram, W. Dietzsch, R. Böttcher, M.C.M. Gribnau, and C.P. Keijzers, Inorg. Chem. *23*, 3333 (1985)
9. R. Böttcher, R. Kirmse, J. Stach, and C.P. Keijzers, Mol. Phys. *55*, 1431 (1985).
10. R. Böttcher, R. Kirmse, J. Stach, E.J. Reijerse, and C.P. Keijzers, Chem. Phys. accepted.
11. W.B. Mims, Phys. Rev. *B5*, 2409 (1972), Phys. Rev. *B6*, 3543 (1972);
12. R.P.J. Merks and R. de Beer, J. Magn. Reson. *37*, 305 (1980).
13. M. Romanelli, M. Narayana, and L. Kevan, J. Chem. Phys. *80*, 4044 (1984).
14. M. Hemig, M. Narayana, and L. Kevan, J. Chem. Phys. *83*, 1478 (1985).
15. M. Iwasaki and K. Toriyama, J. Chem. Phys. *82*, 5415 (1985).
16. A.V. Astashkin, S.A. Dikanov, and Yu. D. Tsvetkov, Chem. Phys. Lett. *122*, 259 (1985).
17. A. de Groot, R. Evenlo, and A.J. Hoff, J. Magn. Reson. *66*, 331 (1986)
18. D. Snaathorst and C.P. Keijzers, Mol. Phys. *51*, 509 (1984)
19. M.A. Hefni, N.M. McConnel, F.J. Rietmeijer, M.C.M. Gribnau, and C.P. Keijzers, Mol. Phys. in press.
20. W.B. Mims and J. Peisach, J. Chem. Phys. *69*, 4921 (1978)
21. S.A. Dikanov, Yu. D. Tsvetkov, M.K. Bowman, and A.V. Astashkin, Chem. Phys. Lett. *90*, 149 (1982)
22. A.J. Hoff, A. de Groot, S.A. Dikanov, A.V. Astashkin and Yu. D. Tsvetkov, Chem. Phys. Lett. *118*, 41 (1985)

JOURNAL OF MAGNETIC RESONANCE 67, 114–124 (1986)

CHAPTER VIII

Comparison of ESEEM, ESE-ENDOR, and CW-ENDOR on ^{14}N in a Powder

E. J. REIJERSE, N. A. J. M. VAN AERLE, AND C. P. KEIJZERS

Department of Molecular Spectroscopy, Research Institute of Materials, Faculty of Science, University of Nijmegen, Toernooiveld 6525 ED Nijmegen, The Netherlands

R. BÖTTCHER

Department of Physics, Karl-Marx-University, Linnéstrasse 5, 7010 Leipzig, German Democratic Republic

AND

R. KIRMSE AND J. STACH

Department of Chemistry, Karl-Marx-University, Talstrasse 35, 7010 Leipzig, German Democratic Republic

Received October 8, 1985

Three different techniques were applied for the determination of the ^{14}N couplings in powdered 0.3% copper-doped nickel(II)bis(*N,N*-diethyl dithiocarbamate) electron spin-echo envelope modulation (ESEEM), electron spin-echo ENDOR, and continuous-wave ENDOR. Comparison of the experimental data obtained with these methods shows their complementary nature and suggests that ESEEM and one of the ENDOR techniques should be applied together to obtain maximum information. The various powder spectra were simulated using tensors which are known from single-crystal studies. Intensities and transition probabilities were computed by complete diagonalization of the spin-Hamiltonian matrix. The correspondence with the experimental spectra is quite promising.

INTRODUCTION

Recently several electron spin-echo envelope modulation (ESEEM) and CW-ENDOR studies showed the possibility of measuring, in single crystals, small interactions of nuclei with a low magnetic moment (*1–4*). The interpretation of the spectra of quadrupole nuclei (^{14}N, ^{27}Al, and ^{2}H) can be difficult especially when the hyperfine, quadrupole, and the nuclear Zeeman interactions are of the same order of magnitude. In these cases, only by complete diagonalization of the spin-Hamiltonian matrix is it possible to account for the intensities and the frequencies of the spectral lines (*4*).

In powders the interpretation of ESEEM and ENDOR spectra can be more complicated or even impossible, unless one succeeds in simulating the spectra, again by complete diagonalization of the spin-Hamiltonian matrix.

In this paper we compare the applicability of three different techniques, ESEEM, ESE-ENDOR, and CW-ENDOR, for studying powdered samples. As a test sample we use nickel(II)bis(*N,N*-diethyl-dithiocarbamate) doped with ^{63}Cu(II) [Cu/Ni(et_2dtc)$_2$]. This system has been studied extensively with single-crystal ESR, ENDOR, and ESEEM (*4–6*). The unpaired electron of copper is delocalized for about 50% to the sulfur ligand atoms (*7*). The nitrogen atoms are situated in the third coordination sphere. Their quadrupole and hyperfine interaction are of the same order of magnitude as the nuclear Zeeman interaction (*4*) which necessitates the complete diagonalization of the Hamiltonian matrix for the calculation of the transition frequencies and intensities.

We demonstrate how the powder spectra can be simulated in a satisfactory manner and how the different techniques yield complementary information. The time economics and the sensitivity of the techniques are also considered.

EXPERIMENTAL

All pulsed experiments were carried out at a temperature of 20 K with the ESE spectrometer described previously (*4*). The ESEEM spectra were recorded using the three-pulse method (*8*). 90° pulses of 50 ns were used in order to excite a limited region of the powder spectrum. The ESE-ENDOR spectra were measured with the same three-pulse sequence except that during the full fixed time between the second and third microwave pulses (90 μs), rf power was supplied. An A-300 ENI amplifier was used for the amplification of the rf pulses. In all ESE-ENDOR experiments the value of τ (time space between first and second microwave pulses) was 200 ns. The rf coil consisted of 15 loops turned around the strip of a strip-line resonator (*9*) in such a way that both the powdered material and the strip were situated inside the coil.

The CW-ENDOR investigations were made with a modified Varian E1700 spectrometer at T = 27.2 K using liquid neon. This "low-power" ENDOR apparatus employs a 20 W distributed amplifier which is loaded by a three-turn coil placed inside a H_{102} cavity. The measurements were done in the δf mode of operation (δf = 10 kHz) without low-frequency magnetic field modulation. In this mode the rf signal (frequency f) is square-wave frequency modulated at a 1 kHz rate and fed to the rf gate. The gate chops the frequency-modulated signal at a 2 kHz rate. In this manner alternate rf pulses which are shifted in frequency above and below the value f by δf are generated. The 1 kHz component of the ENDOR signal is proportional to the difference of the magnitude of the ENDOR enhancement at $f \pm \delta f$. Therefore, in the δf mode the first-derivative line shape of the ENDOR signal is observed. No gated preamplifier was used in contrast to the original Varian arrangement. The CW-ENDOR spectra were recorded in the frequency range 0.5–4.5 MHz.

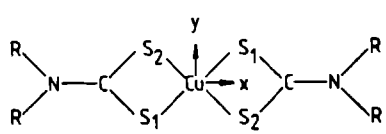

FIG. 1. Molecular structure of host complex Ni(et_2dtc)$_2$, with the principal axes of g and Cu hyperfine tensor. R = ethyl.

TABLE 1

Cu/Ni $(et_2dtc)_2$ Interaction Tensors Used in Powder Simulations (in Units of 10^{-4} cm^{-1})

Tensor: Reference:	g (5)	^{63}Cu A (5)	^{14}N A (10)	^{14}N P (10)
iso	—	−84.5	−0.38	—
xx	2.017	42.6	0.06	0.25
yy	2.020	41.4	0.06	0.25
zz	2.084	−84.0	−0.12	−0.5
xz	—	—	−0.015	−0.065

Powders of ^{63}Cu/Ni$(et_2dtc)_2$ were prepared by evaporation of a trichloromethane solution containing the Cu and Ni complexes in a mole ratio of 3:1000.

EXPERIMENTAL RESULTS

In Fig. 1 the structure of the host complex and the directions of the interaction tensors are shown. All tensors (Table 1) are known from single-crystal experiments (*4, 5, 10*). They are nearly axial and coinciding. This property simplifies the EPR

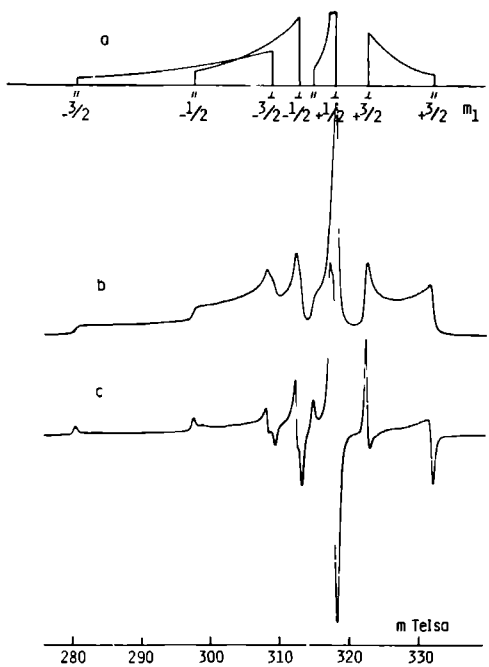

FIG. 2. EPR powder spectrum of ^{63}Cu/Ni$(et_2dtc)_2$. (a) Idealized absorption spectrum, assuming axiality for the coinciding g and Cu A tensors (b) Echo-induced EPR spectrum, measured with the two-pulse method (τ = 200 ns). (c) First-derivative absorption EPR spectrum Note that because of the different microwave frequencies used in the various experiments the magnetic field does not correspond to the fields in the other figures.

powder spectrum considerably (Fig. 2). For powder ESEEM/ENDOR measurements the Cu $m_I = \frac{3}{2}$ region is the most appropriate one to measure since there is no overlap with other Cu lines and the anisotropy is large enough to allow a limited selection of orientations to be excited.

Because of the near-axial and near-coinciding tensors one might expect that the ESEEM and ESE-ENDOR powder spectra measured at different fields will resemble single-crystal spectra measured at the same fields. As a reference, Fig. 3 shows some calculated single-crystal ENDOR spectra in this range of fields/orientations. The experimental powder ESE-ENDOR and FT-ESEEM spectra (Figs. 5a and 6a), however, show a distinct broadening of the signals and in some instances the lines even disappear completely. This can be due to (a) the slight nonaxiality of the tensors, (b) the use of a finite microwave pulsewidth, and (c) spectral diffusion. All these effects lead to a widening of the range of orientations which is excited by the microwave pulses. The broadening is most pronounced in the case of ESEEM; this is most probably caused by the instrumental dead-time which cuts off the initial part of the modulation pattern where the broad lines have their time domain.

The CW-ENDOR spectra (Figs. 7 and 8) show a similar broadening behavior of the signals and also a complete disappearance of the transitions in the field range in which they are found to be strongly angular dependent in the single-crystal rotation pattern (Fig. 3). Powder lineshapes are observed for the less angle-sensitive transition 4-6 over the whole field range (see Fig. 7 around 3.8 MHz). This indicates that even in a CW experiment a broad range of orientations is excited! Nevertheless, three of the six possible transitions can be observed over the complete range of fields/orientations. The two strongly angular-dependent ones, 4-5 and 5-6, are observable only for orientations near the parallel and the perpendicular site of the EPR powder pattern.

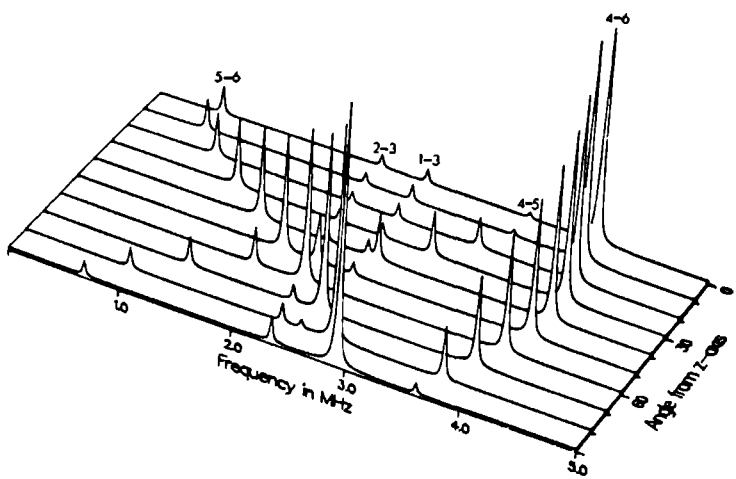

FIG 3 Single-crystal ENDOR simulations for $^{63}Cu/Ni(et_2dtc)_2$, calculated with tensors obtained from Ref (*10*) (see Table 1) Fields/orientations were chosen such that the microwave carrier frequency was positioned at the Cu $m_I = \frac{3}{2}$ EPR transition The peaks are labeled in accordance with the energy-level diagram in Fig 4.

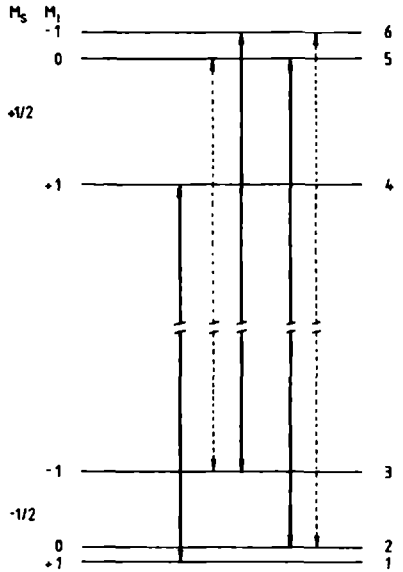

FIG. 4. Energy-level diagram for electron spin $S = \frac{1}{2}$ and ^{14}N nuclear spin $I = 1$ calculated for B oriented 20° from molecular z axis.

The sixth transition, however, (indicated as 1-2 in Fig. 6b) cannot be detected because of its very low frequency and its very small transition probability.

The sensitivity of the ESE-ENDOR technique appeared to be distinctively lower than that of the FT-ESEEM technique: The observed ENDOR effect was less than 5% whereas the ESEEM modulation depth was about 15%. In practice it took about 7 min for an ESEEM experiment to obtain a fairly good S/N ratio as compared to 30 min for an ESE-ENDOR experiment. This can be due to a poor impedance match of the rf coil leading to a reduced rf power at the sample. On the other hand this low rf-power limit may simplify the calculations (see below). The CW-ENDOR powder spectra were recorded within 4 minutes for each spectrum.

It should be noted that only 80 mm^3 of material or less has been used in all experiments.

CALCULATIONS

The powder spectra were simulated using a spin Hamiltonian with $S = \frac{1}{2}$, ^{63}Cu $I = \frac{3}{2}$, ^{14}N $I = 1$ and including the g tensor, the copper and nitrogen hyperfine and Zeeman interactions, and the nitrogen quadrupole interaction (Table 1). The Hamiltonian matrix was diagonalized and the transition frequencies and probabilities were calculated for about 2000 orientations of the magnetic field.

For the ENDOR simulations a semitheoretical procedure was followed: The NMR transition probabilities were weighed with the EPR transition probabilities in which the energy levels involved took part. Therefore, NMR transitions between levels which are not "hit" by EPR transitions will not contribute to the simulated spectra. Thus the ENDOR intensities P_{ij} are calculated as

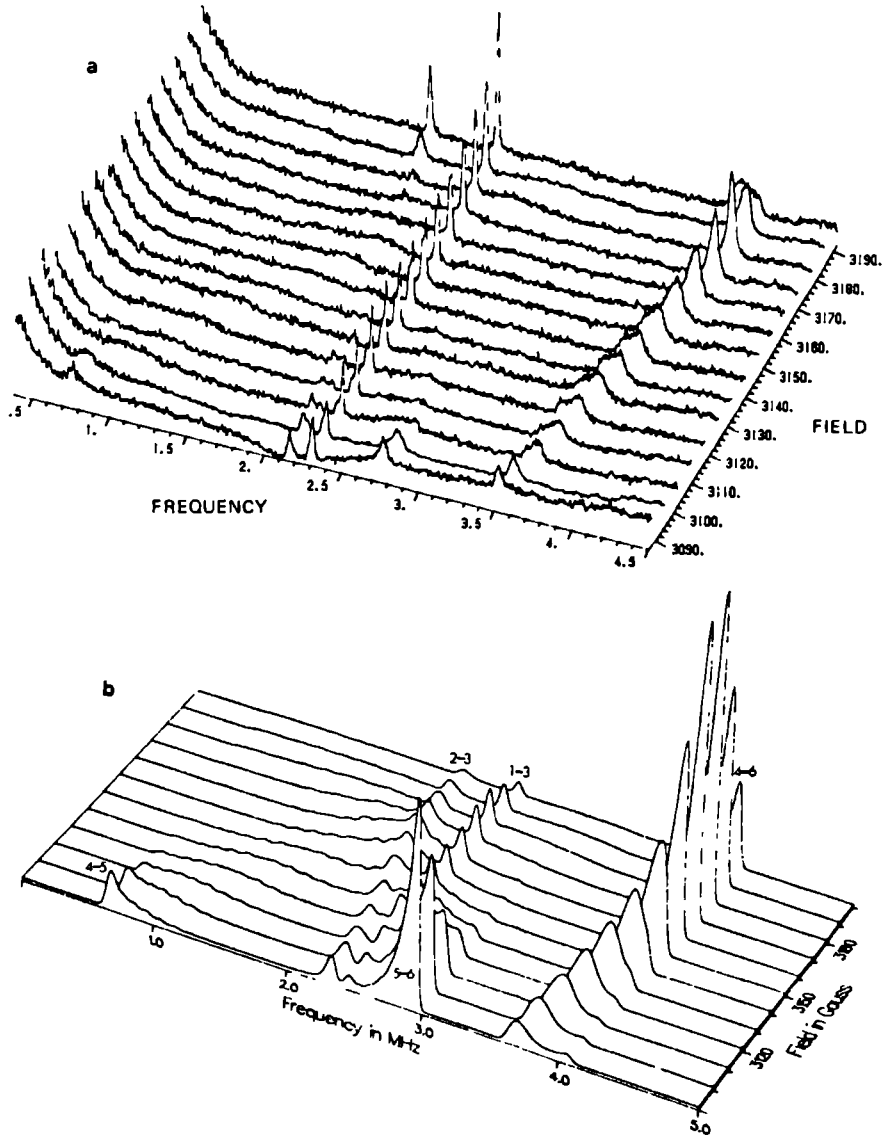

FIG. 5. (a) Experimental ESE-ENDOR powder spectra of $^{63}Cu/Ni(et_2dtc)_2$ measured at 20 K in the field range of the Cu $m_I = \frac{3}{2}$ transition with the three-pulse sequence (τ = 200 ns, T_{rf} = 90 μs). (b) Simulated ENDOR powder spectra in the same field range.

$$P_{ij} = M_{ij} \times \{\sum_k M_{ik} G(\omega_0 - \omega_{ik})\} \times \{\sum_l M_{jl} G(\omega_0 - \omega_{jl})\} \times B(i,j) \qquad [1]$$

where

$$B(i,j) = \frac{e^{-E_i/kT} - e^{-E_j/kT}}{\sum_k e^{-E_k/kT}}.$$

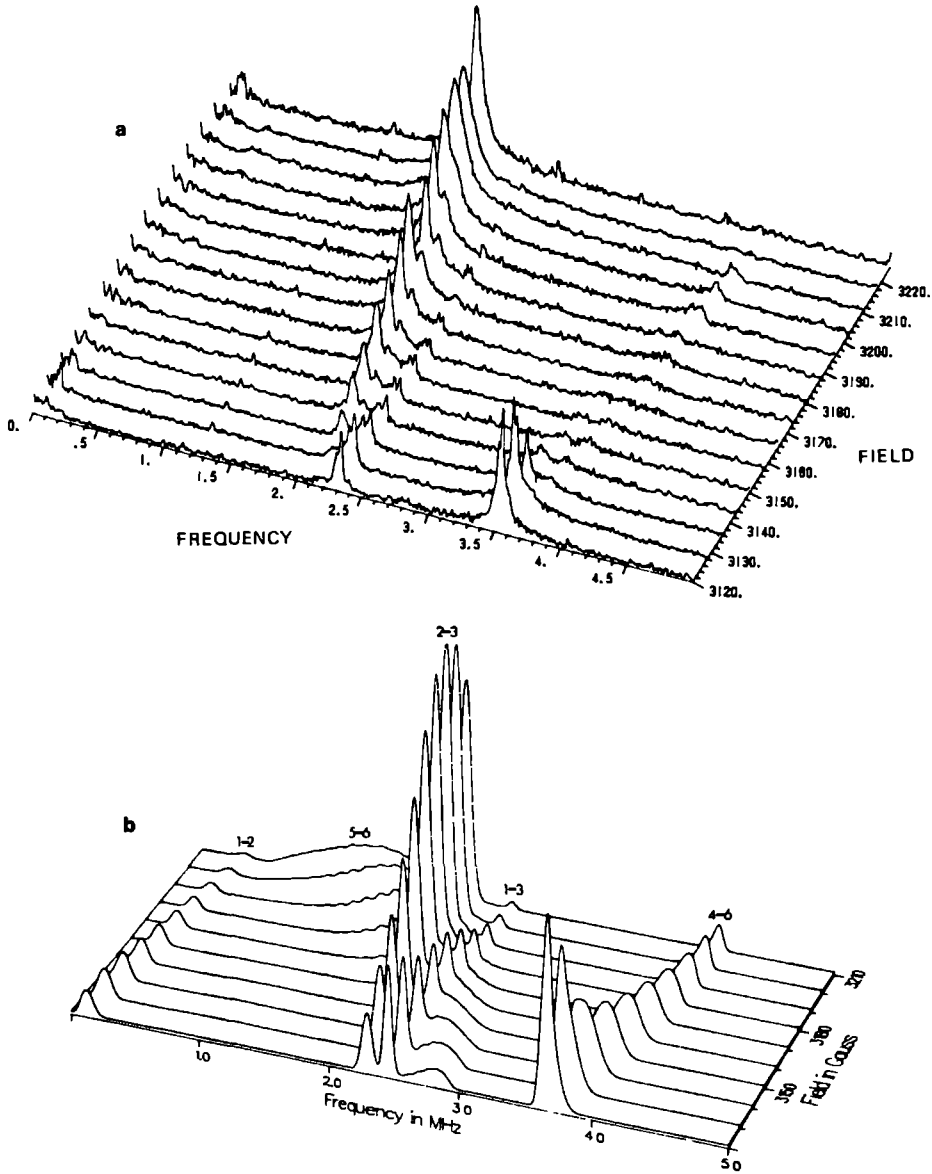

FIG. 6. (a) Experimental FT-ESEEM powder spectra of $^{63}Cu/Ni(et_2dtc)_2$ measured with the three-pulse method. Experimental data as indicated in Fig. 4. (b) Simulated FT-ESEEM powder spectra in the same field range.

M_{ij} are the transition moments between state i and j; i.e., the elements of the perturbation Hamiltonian matrix on the basis of the eigenvectors of the stationary Hamiltonian. $G(\omega_0 - \omega)$ is the excitation lineshape function around the carrier frequency of the microwave pulses (ω_0). $B(i, j)$ is the Boltzmann equilibrium correction factor. The summations over k and l run over all energy levels. The simulations thus obtained

FIG. 7. Experimental CW-ENDOR powder spectrum of $^{63}Cu/Ni(et_2dtc)_2$ measured at $T = 27.2$ K for $B \perp z$ (Cu $m_I = \frac{3}{2}$ EPR transition). $\nu = 9.58$ GHz, $B = 3442$ G. It is not likely that the line at 1.9 MHz originates from ^{14}N since it is only present at this field position and can hardly be attributed to the powder pattern of transition 5–6.

are theoretical representations of CW-ENDOR spectra, discarding only relaxation effects.

Since ESE-ENDOR spectra are also sensitive to the waiting time τ between the first and second pulse in the three-pulse ENDOR sequence, the above expression is less applicable to the simulation of these spectra. Yet it will yield a reliable qualitative picture of the ESE-ENDOR spectra because according to the relations of Liao and Hartmann (*11*), the ENDOR effect on the electron spin-echo for a system of one electron and one nuclear spin $I = 1$ and both the electron and the nucleus in strong-field approximation, is given by

$$F = 1 - \tfrac{1}{2}(1 + \tfrac{1}{3}(1 + 2\cos^2(\theta/2) + 2\sin^2(\theta/2)\cos[(\omega_{ij} - \omega_{kn})\tau])) \qquad [2]$$

where θ is the rf pulse angle and $i - k$ and $j - n$ are the allowed EPR transitions. It can be readily inferred from this expression that "blind spots" ($F = 0$) will occur at τ values equal to a multiple of $2\pi/(\omega_{ij} - \omega_{kn})$. Since in our experiments no ENDOR frequency was observed above 5 MHz, which is the frequency corresponding to our τ value of 200 ns, no blind spots are to be expected.

For low rf pulse power, expression [2] reduces to

$$F = \tfrac{1}{12}\theta^2(1 - \cos[(\omega_{ij} - \omega_{kn})\tau]). \qquad [3]$$

Therefore, in this regime the ENDOR effect will be linearly proportional to the rf pulse power just as we have observed in our experiments. However, these expressions do not yield the exact ESE-ENDOR intensities in our experiments since they were derived for the case of unmixed electron and nuclear spin levels in which all ENDOR transition probabilities are the same. In our system we have to account for differences in ENDOR transition probabilities caused by the mixing of the nuclear spin levels as well. Therefore, the CW-ENDOR simulations are also used for the ESE-ENDOR spectra. Because of this approximation and because the CW-ENDOR spectra also depend strongly on the cross-relaxation times, the simulations should be regarded as a qualitative picture for both CW- and ESE-ENDOR measurements.

In the case of ESEEM simulations the EPR transition probabilities were processed using the modulation relations derived by W. B. Mims (*8*) for the three-pulse sequence in a generalized manner:

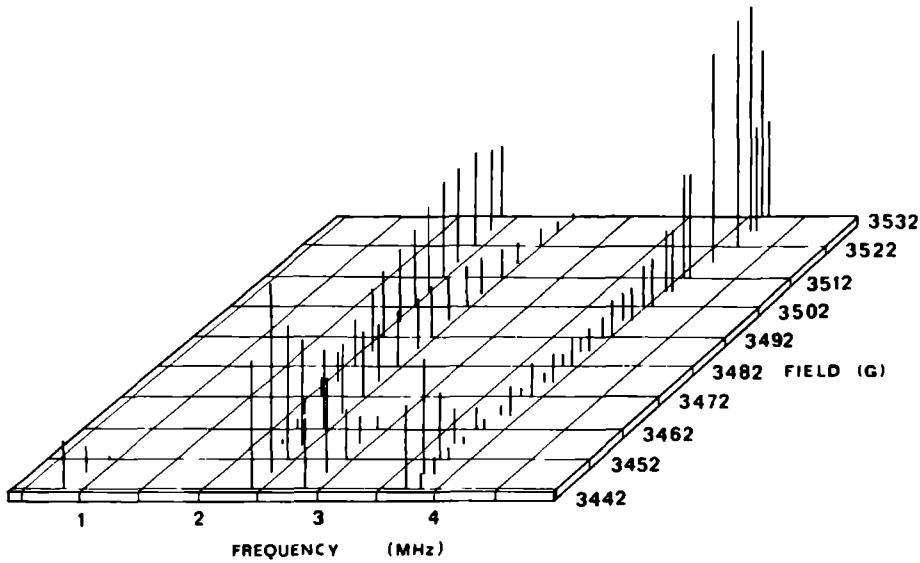

FIG. 8. Experimental CW-ENDOR powder spectra of $^{63}Cu/Ni(et_2dtc)_2$ (reproduced as stick spectra) measured at 27.2 K in the field range of the Cu $m_I = \frac{3}{2}$ EPR transition.

$$P_{kn} = N\{\chi_{kn} + \sum_{i>j} 2\chi_{ij,kn} \cos(\omega_{ij}\tau)\} \qquad [4]$$

where

$$\chi_{kn} = \sum_{i} |M_{ik}|^2 |M_{in}|^2$$

$$\chi_{ij,kn} = \mathrm{Re}[M_{ik}^* M_{in} M_{jn}^* M_{jk}].$$

P_{kn} is the modulation intensity at frequency ω_{kn}, N is a normalization constant, and M_{ij} are the elements of the transition matrix as in Eq. [1].

In principle all indices run over all energy levels involved in the EPR transitions. In the case where these relations were originally derived for, no mixing of electron-spin eigenstates by the nucleus studied (^{14}N in our case), the contributions to the ESEEM intensities automatically reduce to those derived by Mims. By using the relations in this manner, however, the program is able to deal with any number of electrons or any pseudo-electron-spin particle.

DISCUSSION

A comparison of the ESE-ENDOR spectra (Fig. 5a) with the ESEEM spectra (Fig. 6a) reveals that the field/orientation dependence of the intensities is reversed. In other words, spectral features missing in the former spectra are present in the latter and vice

versa. This illustrates the complementary nature of the two techniques: they access the spin Hamiltonian from a different "view angle."

A comparison of the two ENDOR techniques (Figs. 5a and 8) shows differences in field/intensity behavior, in particular of line 1-3. This illustrates that these techniques depend on different mechanisms: T_1 and cross-relaxation (CW-ENDOR) and destruction of phases (ESE-ENDOR). Both techniques depend in first order on the NMR transition probabilities and only these were included in the simulations. Because of the difference between these spectra it is impossible that the simulations are valid for both techniques simultaneously. In fact, it seems that they result in an average of the two experimental sets of spectra (see below).

The simulated powder ENDOR and ESEEM spectra are presented in Fig. 5b and 6b. A 120 MHz Lorentzian lineshape function around the carrier frequency appeared to be necessary to simulate the broadening beyond detection of the anisotropic lines 5-6 and 4-5 in all spectra. This excitation width is approximately equal to the bandwidth of the cavity which was used for the pulsed experiments (Q = 100) or 6 times the inverse pulsewidth (50 ns). This large excitation width resulted also in broad and sometimes powderlike lines in some of the spectra. This is completely in accordance with the experimental observations (cf. transitions 4-5 and 4-6 in Figs. 5–7). Considering the fact that these effects were present in the pulsed as well as in the CW-ENDOR spectra, we conclude that spectral diffusion is the main broadening mechanism in this case.

The ENDOR simulation shows a larger line broadening than the experimental spectra; yet the slightly anisotropic line 2-3 can be tracked over the whole field range in contrast to the sharp experimental line which disappears at intermediate field values. Furthermore, the intensity of the very anisotropic transition 5-6 is much too pronounced in the simulations. The FT-ESEEM simulation, however, shows a nice correspondence with the experimental spectra despite the suppression of the anisotropic peaks caused by the instrumental dead time.

CONCLUSIONS

Both ESEEM and ESE-ENDOR/CW-ENDOR are useful techniques and should be used together whenever possible because the spectral information from the two techniques is complementary. It has been demonstrated that the experimental spectra (in particular the ESEEM spectra) can be simulated satisfactorily with our software, despite the broadening effects. It is to be expected that in the future more complicated disordered systems can be analyzed following this procedure.

ACKNOWLEDGMENTS

The authors thank the following people at the University of Nijmegen: Mr. Jan van Os and Mr. Adrie Klaassen for their technical support and their continuous effort in improving the performance of the ESE spectrometer, Addy Thiers for developing graphical representation software and Professor E. de Boer for critically reading the manuscript and for useful suggestions. This work is financially supported by the Netherlands Foundation for Chemical Research (SON).

REFERENCES

1 H. BARKHUYSEN, R. DE BEER, E. L. DE WILD, AND D. VAN ORMONDT, *J Magn Reson* **50,** 299 (1982).
2 J. ISOYA, M. K. BOWMAN, J. R. NORRIS, AND J. A. WEIL, *J Chem. Phys* **78,** 1735 (1983).
3 D J. SINGLE, W A. J. A. VAN DER POEL, J. SCHMIDT, J. H. VAN DER WAALS, AND R. DE BEER, *J Chem Phys* **81,** 5453 (1984).
4 E. J. REIJERSE, M. L H. PAULISSEN, AND C. P. KEIJZERS, *J Magn. Reson* **60,** 66 (1984).
5 M. J. WEEKS AND J. P. FACKLER, *Inorg Chem* **7,** 2548 (1969).
6 D. SNAATHORST, C. P. KEIJZERS, A. A. K. KLAASSEN, E. DE BOER, V. P. CHAKO, AND R. GOMPERTS, *Mol Phys* **40,** 585 (1980).
7. C. P. KEIJZERS, H. J. M. DE VRIES, AND A. VAN DER AVOIRD, *Inorg Chem* **11,** 1338 (1972).
8 W. B. MIMS, *Phys Rev B* **5,** 2409 (1972); **6,** 3543 (1972).
9. J. L. DAVIS AND W. B. MIMS, *Rev Sci Instrum.* **49,** 1095 (1978).
10 R. KIRMSE, J. STACH, AND R. BÖTTCHER, private communication.
11 P. F. LIAO AND S. R. HARTMANN, *Phys. Rev B* **8,** 69 (1973).

CHAPTER IX[†]

Spin Lattice Relaxation of a Jahn-Teller System

E.J. REIJERSE, N.A.J.M. VAN AERLE, C.P. KEIJZERS, AND E. DE BOER.

Department of Molecular Spectroscopy,
Research Institute of Materials
University of Nijmegen, Toernooiveld, 6525 ED Nijmegen, The Netherlands

Spin-lattice relaxation (T1) measurements of two different complexes in a ^{63}Cu(II) doped crystal of Zn(II) hexakis pyridine N-oxide perchlorate ($Zn(PyO)_6(ClO_4)_2$), grown from a DMF solution are presented the Jahn-Teller active $Cu(II)(PyO)_6$-complex and the JT inactive $Cu(II)(PyO)_5DMF$-complex

The T1 of the Jahn-Teller active species is less than one order of magnitude shorter than that of the JT inactive species This contrasts with other studies where differences of several orders of magnitude are reported In the studied temperature range both relaxation processes can be described by a Raman-mechanism

[†] Journal of Molecular Structure, 142 (1986) 175-178

IX.1 Introduction

Several studies were reported about the role of the Jahn-Teller effect in spin-lattice relaxation (1-4). Most authors report relaxation times of JT molecules which are several orders of magnitude shorter than those observed for similar non-active molecules, suggesting that the JT effect is a very effective relaxation mechanism.

However, all these investigations seem to suffer from the lack of a proper reference material, i.e. a non-active analogue of the JT molecule situated in the same (host) lattice. Therefore, it is difficult to relate the relaxation data to the JT effect itself as an independant relaxation mechanism.

In this paper we present T1 data obtained from a single crystal of ^{63}Cu doped Zn-hexakis pyridine N-oxide perchlorate ($Cu{:}Zn(PyO)_6(ClO_4)_2$) grown from a DMF solution. From previous EPR studies (5) it is known that DMF creates two solvated species in the crystal: $[Cu(PyO)_5DMF]^{2+}$ and $[Cu(PyO)_4(DMF)_2]^{2+}$. These complexes are JT inactive. EPR spectra show that their geometry is almost identical to the low temperature structure of the JT active Cu hexakis complex. Therefore, they are an excellent reference to the JT complex in the relaxation studies.

IX.2 Experimental

Single crystals were grown by slow evaporation of a DMF-solution which contained both complexes in a ratio of 1:99 (Cu:Zn).

Three different puls-sequences were used all of which have in common that the electron-spin magnetization is saturated by one or more intense microwave pulses and subsequently the recovery of the magnetization is monitored by a standard two-pulse Hahn echo sequence.

IX.3 Results and Discussion

In order to obtain a maximum separation between the lines of the different species the crystal was oriented with the magnetic field along g// of one of the three static JT sites (the g and Cu-A tensors of all species coincide). In figure 1 field swept ESE spectra measured at different temperatures are presented. The large echo intensities at 15 K (marked with 'o') are due to the JT complex. The Copper quartet of the parallel site can be clearly recognized. The very intensity at higher field is due to a superposition of the perpendicular sites of all species. The intensities due to the solvated JT inactive species (marked with 'x' and '+') have field values very close to the corresponding lines of the JT active complex. Upon raising the temperature the intensities of

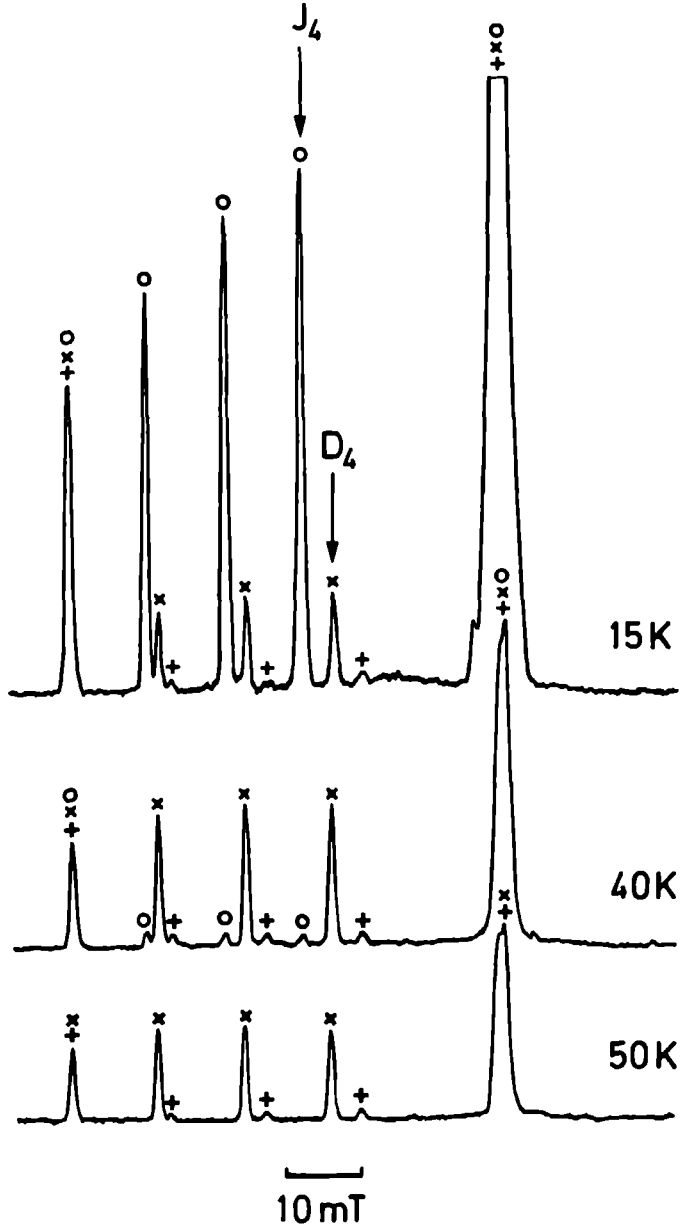

Fig. 1. Field swept ESE spectra as a function of temperature. (o) JT-active complex: $Cu(PyO)_6$, (x) $Cu(PyO)_5(DMF)$, (+) $Cu(PyO)_4(DMF)_2$. The relaxation measurements were made on the lines indicated by D4 and J4.

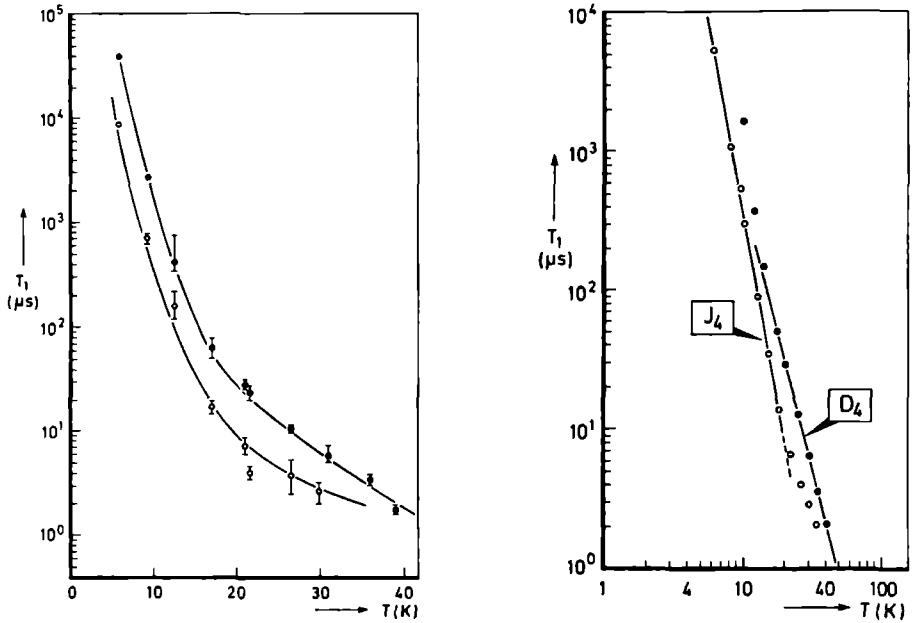

Fig. 2. Temperature dependance of T1, measured on the linepositions D4 (o) and J4 (o) in fig. 1. Error margins are indicated in the Lin-Log plot (left); the Log-Log plot shows J4. 1/T1 (:) $T^{5.2\pm0.5}$, D4: 1/T1 (.) $T^{3.9\pm0.5}$

the JT active species decrease as a result of the increasing exchange rate caused by the dynamic JT effect.

All relaxation measurements were made on the Cu m_I=-3/2 resonance of each species (D4 and J4). In figure 2 the average T1 's obtained with the three different methods are presented. The relaxation time of the JT active species is never more than one order of magnitude shorter than that of the JT inactive species. At higher temperatures the relaxation times even tend to become equal. Since the lattice effect on the difference of relaxation times can be virtually ruled out, we must conclude that the small difference in T1-relaxation is due to the Jahn-Teller effect.

The log-log plot in figure 2 shows the following relations between T1 and the temperature: $T_1^{-1}(:)T^{5.2\pm0.5}$ (6K < T < 20K) for the Jahn-Teller active species and $T_1^{-1}(:)T^{3.9\pm0.5}$ (15K < T < 40K) for the Jahn-Teller inactive species. These relations suggest a Raman-mechanism in the given temperature range. A similar behaviour was found for other Cu-complexes (6).

IX.4 Conclusion

In the studied temperature range the role of the Jahn-Teller effect in the spin-lattice relaxation seems to be substantial but not dominating. There is no clear evidence for a special Jahn-Teller supported relaxation mechanism since both species can be described by a conventional Raman-mechanism.

References

1. Townsend, M.G., and Weissman, S.I., J. Chem. Phys. *32*, 309 (1960).
2. Breen, D.P. Krupka, D.C., and Williams, F.I.B., Phys. Rev. *189*, 241 (1969).
3. Dang, L.S., Buisson, R. and Williams, F.I.B., J. Phys. (France) *35*, 49 (1974).
4. Lee, K.P., and Walsh, D., Phys. Stat. Sol. (b) *62*, 689 (1974).
5. Keijzers, C.P., McMullan, R.K., Wood, J.S., van Kalkeren, G., Srinivasan, R., and de Boer, E., Inorg. Chem., *21*, 4275 (1982).
6. Al'tshuler, S.A., Kirmse, R., and Solov'ev, B.V., Solid State Phys., *8*, 1907, (1975).

The Electron Spin Echo technique is applied to transition metal compounds in several experiments. As opposed to the traditional "Continuous Wave" ESR technique, in the E.S.E. experiment the sample is exposed to (a series of) short microwave pulses. After each pulse-train the sample responds with one or more microwave echoes. By measuring the echo-height as a function of a timeparameter from the pulse-sequence, information about the sample can be obtained which is hardly accessible with conventional C.W. ESR. The aim of the work described in this thesis is as follows:

- To build an E.S.E. spectrometer to the highest technological standards possible.

- To develope the control- and dataprocessing software for this instrument.

- To investigate what new information can be obtained with ESE spectroscopy about the structure of transition metal compounds.

- To develope simulation algorithms for the calculation of spectra obtained with several E.S.E. techniques especially when they are applied to powders.

Three types of experiments were employed, namely T_1-relaxation measurements, the determination of hyperfine and quadrupole interactions through the nuclear modulation effect (Electron Spin Echo Envelope Modulation Spectroscopy) and through the detection of ESE-ENDOR.

In Chapter I the principle of ESE spectroscopy and these three types of experiments are explained.

In Chapter II the instrumental aspects (both hard- and software) are treated.

Chapter III deals with the development of a microwave resonator which enables single crystal studies with the ESE-ENDOR technique at temperatures between 4K and 300K. In this resonator the crystal can be rotated over two axes which is not possible in other types of ENDOR resonators.

In Chapter IV the algorithms are described that were used for the simulation of the different types of ESE experiments. Special attention is payed to numerical aspects of the calculation of powder spectra for spin systems with a high multiplicity.

In Chapter V the nuclear modulation effect is applied for the determination of the hyperfine- and quadrupole tensor of ^{14}N in Cu(II)/Ni(II) bis(N,N-di-n-butyl dithiocarbamate). The ^{14}N quadrupole tensor can be explained

theoretically with Extended Hückel Molecular Orbital calculations. For the interpretation of the ^{14}N hyperfine tensor, however, an "unrestricted" M.O. calculation turned out to be necessary indicating a spinpolarisation effect. Moreover, the multicenter terms gave a significant contribution to the total hyperfine interaction. From this it is concluded that one should be cautious with the interpretation of small hyperfine interactions of nuclei in high coordination spheres in terms of spin densities.

In Chapter VI a similar study applied to Cu(II)/Ni(II) bis (cis-1,2-dicyanoethene-dithiolate) is presented. As opposed to the dithiocarbamate compound which contains only one set of two equivalent ^{14}N-atoms, this compound contains two non-equivalent sets of ^{14}N-atoms which increases the complexity of the spectra considerably.

In Chapter VII ESEEM model calculations are presented for I=1/2, I=1 and I=3/2 nuclei coupled to an electron S=1/2 in disordered systems. On the basis of simulations of the frequency domain, the boundary conditions of frequently used approximations in the interpretation of FT-ESEEM powder spectra, are determined. It turns out that for quadrupole nuclei with a quadrupole interaction of the same order of magnitude as the Nuclear Zeeman interaction, only for specific values of the hyperfine tensor FT-ESEEM spectra with some resolution can be expected.

In Chapter VIII three methods for determining hyperfine interactions are compared: ESEEM, ESE-ENDOR and CW-ENDOR. The methods are applied to 1% doped Cu(II)/Ni(II) bis (N,N-diethyl dithiocarbamate) in powdered form. It turns out that ESEEM and the ENDOR techniques yield complementary spectral information. The different powder spectra are simulated by the algorithms discussed in Chapter IV using the interaction tensors that were determined in Chapter V. The correspondence of the simulated and the experimental spectra is quite satisfying.

In Chapter IX T_1-relaxation measurements on two molecular species in a single crystal of 1% doped Cu(II)/Zn(II) hexakis (pyridine N-oxide) perchlorate grown from a DMF solution are presented. The two species are the Jahn Teller active Cu(II)$(PyO)_6$-complex and the Jahn-Teller inactive Cu(II)$(PyO)_5DMF$ complex. T_1 of the JT active species is less than one order of magnitude shorter than that of the JT-inactive species. This result contradicts with other studies where differences of several orders of magnitude are reported. These studies, however, deal with species in different crystals whereas our study was confined to two species in one crytal!

De Electron Spin Echo techniek is in een aantal verschillende experimenten toegepast op overgangsmetaal verbindingen. Met de E.S.E. techniek wordt, in tegenstelling tot de meer traditionele "Continuous Wave" ESR techniek, het monster blootgesteld aan (een serie van) korte microgolf pulsen. Na iedere serie pulsen zendt het monster een gedeelte van de toegevoerde microgolfenergie weer uit in de vorm van een of meer microgolf echo's. Door de echohoogte te meten als functie van een tijdsparameter uit de puls-sequentie kunnen gegevens over het monster gemeten worden die niet of moeilijk toegankelijk zijn m.b.v. CW ESR. Doel van het werk dat beschreven wordt in dit proefschrift is

- Het bouwen en optimaliseren van een E.S.E. spectrometer op een zo hoog mogelijk technisch niveau

- Het ontwikkelen van meet- en dataverwerkings software voor deze E.S.E. opstelling,

- Te onderzoeken in hoeverre nieuwe informatie verkregen kan worden m.b.v. E.S.E. spectrometrie over de struktuur van overgangsmetaal verbindingen en de locaties van kationen in zeolieten,

- Het berekenen en simuleren van spectra gemeten met verschillende E.S.E. technieken in het bijzonder wanneer deze technieken worden toegepast op poeder materialen.

Drie typen experimenten werden gebruikt, namelijk T_1 relaxatie metingen, de meting van hyperfijn en quadrupool interacties via het kernmodulatie effect (Electron Spin Echo Envelope Modulatie) en via de detectie van ESE-ENDOR.

In Hoofdstuk I wordt het principe van E.S.E. en van deze drie typen experimenten besproken.

In Hoofdstuk II worden de instrumentele aspecten (zowel hard- als software) behandeld.

In Hoofdstuk III wordt het ontwerp van een dubbelresonantie resonator besproken die het mogelijk maakt een-kristal studies te verrichten m.b.v. de ESE-ENDOR techniek bij temperaturen tussen 4 en 300 K. Met deze resonator is het mogelijk het kristal om twee assen te draaien hetgeen niet mogelijk is met andere typen ENDOR resonatoren.

In hoofdstuk IV worden de algorithmen beschreven die gebruikt worden voor het simuleren van de verschillende typen E.S.E. experimenten. Er wordt ingegaan op de numerieke aspecten van het berekenen van poederspectra van

spinsystemen met hoge multipliciteit.

In hoofstuk V wordt het kernmodulatie effect toegepast voor het bepalen van de hyperfijn- en quadrupooltensor van ^{14}N in Cu(II)/Ni(II)bis(N,N-di-n-butyl-dithiocarbamaat). De ^{14}N-quadrupool tensor kan theoretisch verklaard worden met Extended Hückel M.O. berekeningen. Voor de interpretatie van de ^{14}N-hyperfijn tensor bleek echter een "unrestricted" M.O. berekening nodig, duidend op een spin-polarisatie effect. Bovendien gaven de meer-centrum termen een belangrijke bijdrage aan de totale hyperfijn interactie. Hieruit wordt geconcludeerd dat bij het interpreteren van kleine hyperfijninteracties van kernen in hoge coordinatie schillen in termen van spindichtheden, voorzichtigheid betracht dient te worden.

In hoofdstuk VI wordt een soortgelijke studie aan Cu(II)/Ni(II) bis(cis-1,2-dicyanoetheen-dithiolaat) beschreven. In tegenstelling tot de dithiocarbamaat verbinding die slechts een set van twee equivalente ^{14}N kernen bevat, is hier sprake van twee niet-equivalente sets ^{14}N atomen hetgeen de interpretatie van de spectra aanzienlijk moeilijker maakt.

In hoofdstuk VII worden ESEEM model berekeningen besproken voor I=1/2, I=1 en I=3/2 kernen gekoppeld aan een electron S=1/2 in wanordelijke systemen. Op basis van simulaties van het frequentiedomein worden de randvoorwaarden bepaald van veel gebruikte benaderingen bij de interpretatie van ESEEM poeder spectra. Het blijkt dat voor quadrupool kernen met een quadrupool interactie van dezelfde grootte-orde als de Kern Zeeman-interactie alleen voor zeer bepaalde waarden van de hyperfijn tensor ESEEM-spectra met enige resolutie verwacht kunnen worden.

In hoofdstuk VIII worden drie methoden vergeleken ter bepaling van de ^{14}N-interacties in gepoederd Cu(II)/Ni(II) bis(N,N-diethyl dithiocarbamaat), namelijk ESEEM, ESE-ENDOR en CW-ENDOR. Het blijkt dat ESEEM en de ENDOR technieken complementaire spectrale informatie leveren. De verschillende poederspectra worden gesimuleerd m.b.v. de algorithmen besproken in hoofdstuk IV, gebruik makend van de tensoren bepaald in hoofdstuk V. De overeenkomst van de gesimuleerde met de experimentele spectra is zeer bevredigend.

In Hoofdstuk IX worden T_1-relaxatie metingen gepresenteerd aan twee moleculaire species in een een-kristal van Cu(II) gedoopt Zn(II) hexakis (pyridine N-oxide) perchloraat gegroeid uit een DMF oplossing: het Jahn-Teller actieve Cu(II)$(PyO)_6$-complex en het JT-inactieve Cu(II)$(PyO)_5DMF$-complex. De T_1 van het JT actieve species is minder dan een grootte-orde korter dan die van het JT inactieve species. Dit is in tegenspraak met andere studies waar verschillen van enkele grootte-orden zijn vermeld. Deze studies hebben echter betrekking op species in verschillende kristallen terwijl in het huidige onderzoek beide species in één kristal aanwezig zijn.

LEVENSLOOP

Ik werd geboren op 1 juni 1956 in Toronto, Canada. Na het voltooien van het Atheneum B aan het Pius X college te Almelo in 1975, begon ik in dat jaar met mijn chemie studie aan de Katholieke Universiteit te Nijmegen. Het kandidaats examen (S2) legde ik cum laude af op 25 september 1978. De doctoraal studie omvatte als hoofdrichting Biofysische Chemie en als bijvakken Informatica en Molecuulspectroscopie. Op 24 mei 1982 werd het doctoraal examen cum laude behaald. Sinds 31 mei 1982 ben ik in dienst van de Katholieke Universiteit Nijmegen als wetenschappelijk medewerker verbonden aan de afdeling Molecuulspectroscopie o.l.v. Prof. E. de Boer. Gedurende deze tijd ben ik tevens betrokken geweest bij het onderwijs in de Fysische Chemie.

STELLINGEN

I De door de Groot et. al. gehanteerde condities waarbij het Electron Spin Echo Envellope Modulatie Spectrum nog geinterpreteerd mag worden in termen van "vrije quadrupole frequenties" zijn niet correct aangegeven in de text. Bovendien blijkt uit modelberekeningen dat deze marges te ruim genomen zijn.

A. de Groot. A.J Hoff, R. de Beer & H. Scheer, Chem. Phys. Lett. **113,** *286 (1985)*

Dit Proefschrift

II Het feit dat het sterk vereenvoudigde model ter beschrijving van het ESEEM effect, gepresenteerd door L. Kevan, door deze auteur met schijnbaar succes wordt toegepast op de meest uiteenlopende systemen, is nog geen bewijs dat deze beschrijving correct is voor al deze toepassingen.

T. Ichikawa, and L. Kevan, J. Am. Chem Soc. **102,** *2650 (1980)*

M. Narayana, and L. Kevan, J Chem. Phys. **75,** *3269 (1981).*

J Michalik, M. Narayana, and L Kevan, J. Phys. Chem **88,** *5236 (1984)*

III De verbreding van de ^{1}H-NMR lijnen van aromatische dianionen is niet, zoals Rabinovitz en medewerkers beweren, het gevolg van een thermisch toegankelijke aangeslagen triplet toestand, maar het resultaat van een relatief hoge concentratie mono-anionen.

A. Minsky, A Y. Meyer, R. Poupko, and M. Rabinovitz, J. Am Chem. Soc. **105,** *2165 (1983)*

M. Rabinovitz, and Y. Cohen, P.A.C S , Division of Petroleum Chemistry, **31,** *777 (1986).*

IV De door Behrens en medewerkers gepresenteerde analyse van de ^{27}Al-NMR lijnvorm van zeolieten ter bepaling van de quadrupole frequentie is niet correct, aangezien de asymmetrie-parameter in dit geval niet verwaarloosd mag worden, en bovendien de lijnbreedte op halve hoogte niet gebruikt kan worden voor de beschrijving van de betreffende poeder lijnvorm.

D. Freude and H.J. Behrens, Crystal Research and Technology, **16,** *K36 (1981)*

V Een gebruikers vriendelijk userinterface behoort vriendelijk te zijn voor zowel beginnende als gevorderde gebruikers.
Chemisch Magazine, november 1985

VI Uit het feit dat VIDITEL in vrijwel geen enkel land is aangeslagen blijkt dat de informatisering van de samenleving niet zo onstuitbaar zal verlopen als algemeen wordt aangenomen.

VII De voortgang van de natuurwetenschappen en van de techniek laten zich helaas goed beschrijven aan de hand van diverse militaire toepassingen van nieuwe vindingen.

VIII Het effect van ontspannings- en meditatie technieken in de wetenschaps beoefening is nog onvoldoende onderzocht en verdient nadere aandacht.
Currect Contence 22/29 juli 1985

IX Ayn Rands "objectivisme" gepresenteerd in haar boek "The Fountainhead" is in feite weining meer dan "The American Dream" in filosofische verpakking.

X De Nederlandse Spoorwegen zouden voldoen aan een grote behoefte wanneer de ochtendtreinen voorzien waren van couchette rijtuigen.

E.J. Reijerse, 6 november 1986